UNIVERSITÉ DE SHERBROOKE
Faculté de génie
Département de génie mécanique

RÉDUCTION DES CONTRAINTES SECONDAIRES EN TENSION DANS LES PALES EN CÉRAMIQUE DE ROTORS DE TURBINE EN CONFIGURATION RENVERSÉE

Reducing Secondary Tensile Stresses in the Ceramic Blades of the Inside-Out Turbine Rotor Configuration

Thèse de doctorat
Spécialité : génie mécanique

Patrick Dubois

Sherbrooke (Québec) Canada		Octobre 2021

JURY MEMBERS

Mathieu Picard

Supervisor

Vladimir Brailovski

Co-supervisor

Jean-Sébastien Plante

Examiner

François Charron

Examiner

Michael Vick

Examiner

RÉSUMÉ

Depuis quelque temps, un groupe de chercheurs du Groupe d'innovation Createk de l'Université de Sherbrooke travaille sur une nouvelle configuration de rotor de turbine qui utilise un carénage rotatif structurel pour tenir des pales en céramique sous compression, sous l’action du champ centrifuge. Cette configuration de rotor, baptisée *Inside-Out Ceramic Turbine* (ICT) vise à augmenter la température d'entrée de la turbine (TIT) pour les petites turbines, pour lesquelles le refroidissement et les techniques de fabrication complexes sont d'un coût prohibitif.

Plusieurs prototypes et itérations du rotor ICT ont été testés au cours des dernières années, augmentant le temps de fonctionnement et la température d’opération atteignables. Au fur et à mesure que la confiance de l'équipe dans le rotor ICT s'améliore, les problèmes auxquels il est confronté deviennent importants à identifier et à résoudre. Cette thèse vise à étudier et à améliorer la fiabilité des pales en céramique dans des conditions normales de fonctionnement. Ceci est essentiel à l'adoption de la technologie ICT dans un grand nombre de moteurs.

La thèse est découpée en trois parties : (1) isoler la cause la plus probable de défaillance des pales grâce à l'observation des résultats expérimentaux et numériques passés, (2) quantifier l'influence relative des principaux paramètres de conception sur la fiabilité des pales à l’aide d’un modèle numérique, et (3) tester des solutions potentielles qui ciblent les variables de conception les plus critiques, pour obtenir une meilleure fiabilité des pales ICT.

Les pales étant en céramique technique monolithique, actuellement en nitrure de silicium, elles supportent mal les contraintes en tension. Le niveau de contrainte le plus élevé dans les pales s’avère être à l'interface avec les composants métalliques de support, car les pales sont maintenues en place par friction sous une force normale importante, et des contraintes élevées en tension se manifestent à l'interface. Cela demande de réduire d'abord le nombre d'interfaces au minimum, c'est-à-dire uniquement au niveau du bout de pale en appui contre le carénage structurel tournant. Deuxièmement, à cette interface subsistante, les efforts pour réduire le coefficient de frottement, ainsi que pour réduire la différence de dilatation thermique et de déformation tangentielle entre la pale et le carénage, sont essentiels pour obtenir de faibles contraintes en tension à l'extrémité de la pale. La validation expérimentale des revêtements a été menée avec succès : le revêtement de barrière thermique (TBC) appliqué entre l'extrémité de la pale et le carénage pourrait augmenter la température de l'extrémité de la pale et diminuer la température du carénage, conduisant ainsi à une meilleure correspondance de la dilatation thermique ; le nitrure de bore hexagonal (hBN) est un lubrifiant solide à haute température qui réduit considérablement le coefficient de frottement, même sous une charge extrême, et pourrait conduire à au moins doubler la tolérance à la différence de déformation.

Ainsi, un double revêtement de TBC et de hBN devrait réduire la charge en bout de pale. Les niveaux de contrainte réels dépendent de la géométrie de la pale et de la conception globale de la turbine, mais un outil numérique simple a été développé qui permet au concepteur de déterminer quel niveau de réduction de frottement et d'ajustement de dilatation thermique est nécessaire pour obtenir une fiabilité adéquate dans la pale.

Mots-clés : Céramique, Turbomachine, Turbine, Contraintes thermiques, Nitrure de bore, TBC, Nitrure de silicium, Friction.

ABSTRACT

For some time now, a group of researchers in the Createk Innovation Group at Université de Sherbrooke have been working on a novel turbine rotor configuration which uses a structural, rotating shroud to compress ceramic blades under centrifugal load. This rotor configuration, dubbed Inside-Out Ceramic Turbine (ICT) aims at increasing turbine inlet temperature (TIT) for small turbines, for which intricate cooling and complex manufacturing techniques are prohibitively costly.

Several prototypes and iterations of the ICT rotor have run over the last years, achieving consistently better run times and firing temperatures. As the team's confidence in the ICT rotor improves, the issues facing it become important to identify and address. This thesis aims at investigating and improving reliability of the ceramic blades under normal operating conditions. This is central to the adoption of ICT technology in mainstream engines.

The thesis is cut into three parts: (1) isolating the most probable cause of failure in the blades through observation of past experimental and numerical results, (2) quantifying the relative influence of the main design parameters on blade reliability through a numerical model, and (3) testing potential solutions which target the most critical design variables, to achieve a better reliability in the ICT blades.

As the blades are made of monolithic technical ceramic, currently silicon nitride, they do not tolerate tensile stress fields well. The highest stress level in the blades was found to be at the interface with supporting metallic components, as the blades are maintained in place through friction under large normal force, and a strain mismatch is present at the interface. This leads to first reduce the number of interfaces to a minimum, i.e., only at the blade tip pressing up against the rotating structural shroud. Second, at this remaining interface, efforts to reduce coefficient of friction especially, as well as reduce thermal expansion mismatch and hoop strain between the blade tip and the shroud, are key to achieving low tensile stresses at the blade tip. Experimental validation of coatings was successfully conducted: thermal barrier coating (TBC) applied between the blade tip and the shroud, could increase blade tip temperature and decrease shroud temperature, thus leading to a closer match in thermal expansion; hexagonal boron nitride (hBN) is a high temperature solid lubricant which significantly reduces coefficient of friction, even under extreme load, and could lead to at least double the amount of strain mismatch tolerance.

Thus, a double coating of TBC and hBN is expected to reduce the load at the blade tip. Actual stress levels depend on blade geometry and overall turbine design, but a simple numerical tool was developed which could allow the designer to determine what level of friction reduction and thermal expansion fit is required to achieve an adequate reliability in the blade.

Keywords: Ceramics, Turbomachinery, Turbine, Thermal Stresses, Boron nitride, TBC, Silicon nitride, Friction.

Ceramic pillars
Wound up tight, spinning in fire
Guard the cutting edge

ACKNOWLEDGEMENTS

I would first like to acknowledge my research supervisor, Professor Mathieu Picard, for his time, his availability, his passion, and his patience. He let me have fun in my sandbox and encouraged me to spend time on extra-curricular activities. Through this, I had the experience of helping set up the Concours Createk – Famille J.R. André Bombardier during its critical growth phase and took a major part in the purchase and installation of a laser powder-bed fusion metal 3D printer in University of Sherbrooke's facilities. He also encouraged me to mentor and help fellow graduate students, as well as present work in international conferences. Most of all, he let me take my time when I needed it, and pushed me when I needed it, too.

I would also like to extend thanks to my co-supervisor, Professor Vladimir Brailovski, at École de technologie supérieure, in Montréal. The co-supervisorship was a sort of living lab of what process- and design-oriented research could yield when brought together. Although the initial goal was to rely heavily on metal 3D printing and Prof. Brailovski's world-class expertise in the field, he stayed involved in the project even as it moved away from that initial assumption. His inputs on methodic modeling and work, and the time he generously supplied to train me on metal 3D printing, ultimately enabling me to import the knowledge into the University of Sherbrooke, were all very appreciated and still are. Thanks also to Professor François Charron, an inspiration for intellectual curiosity and a master of the simplified model. Thanks go out to Dr. Michael Vick, for generously providing time, for insights on research in turbomachinery and on the importance of a good, finished thesis.

A young engineer could not have asked for a better lab environment than that offered in the melting pot of passionate machine designers found at Createk, with a great many experts and too many memorable moments to list. Developing ICT technology within Createk at University of Sherbrooke, and more recently with Exonetik Turbo, is a true pleasure. Antoine Gauvin-Verville, Céderick Landry, Dominik Thibault, Benoît Picard, Alexandre Landry-Blais, Louis-Philippe Jean and Nicolas Courtois especially deserve mention here, as many hours were spent discussing work and everything else with them. Credit goes to Professor Jean-Sébastien Plante, the 1000 hp instigator of both Createk and Exonetik, paving the way for a creative revolution in the University of Sherbrooke's mechanical engineering ecosystem.

Heartfelt thanks go out to my parents for their support and pride throughout the entirety of my lengthy studies. Thank you for imbuing me with a sense of utter freedom, a desire to learn, and the confidence to try stuff out for myself and to make my own way. And finally, to my wife and best friend, for your extraordinary patience and understanding, your unwavering support and encouragement, and for our deep, powerful bond: merci Marie-Ann.

TABLE OF CONTENTS

LIST OF FIGURES

LIST OF TABLES

LIST OF SYMBOLS

Variables

A	Blade tip area
B	Ceramic static fatigue parameter
b_l	Blade length
b_t	Blade thickness
E	Young’s modulus
F	Force
G	Shear modulus
g	Gravitational acceleration
M	Mass
m	Weibull modulus
N	Ceramic static fatigue parameter
P_f	Probability of failure
R	Blade tip radius
t/l	Thickness to length ratio
T	Temperature
V	Volume
γ	Shear strain
ε	Normal strain
ϑ	Part service life
μ	Coefficient of friction
ρ	Density
σ	Stress
σ_0	Weibull characteristic strength
τ	Shear stress
ω	Rotational velocity

Acronyms

APS	Air Plasma Spray
BC	Bond Coat
CTE	Coefficient of thermal expansion
DIC	Digital Image Correlation
DOD	Domestic object damage
DOR	Degree of reaction
EDS	Energy-Dispersive X-ray Spectroscopy
FE	Finite Element
FOD	Foreign object damage
hBN	Hexagonal boron nitride

ICT[1]	Inside-out Ceramic Turbine
SCG	Subcritical crack growth
SEM	Scanning Electron Microscope
TBC[2]	Thermal Barrier Coating
TC	Top Coat
TIT	Turbine inlet temperature
UTM	Universal Testing Machine
YSZ	Yttria-Stabilized Zirconia
μCT	Micro Computed Tomography

Subscript

b	Blade
CR	Cooling ring
eq	Equivalent
f	Frictional
FR	Full rotor
i	Along the i^{th} principal direction
k	Kinetic
m	mechanical
r	Radial direction
RR	Rim rotor (also named carbon hoop)
s	Static
th	Thermal
z	Axial direction
θ	Hoop direction

---

[1] ICT is used interchangeably to represent the inside-out concept, as well as the specific rotor designs presented in this work.

[2] TBC is used to designate thermal barrier coatings at large conceptually, as well as for the YSZ-based TBC used in the numerical and experimental studies contained in this work.

CHAPTER 1

INTRODUCTION

1.1 Motivation

Increased cycle efficiency in turbomachinery has been one of the great endeavours of research surrounding the field over the past several decades, among many others. The main driving force for this has historically been fuel economy, to decrease air travel and power generation costs. However, more recently, emission targets set by international agreements have given a new sense of urgency to the development of efficiency-improving technologies. This, coupled with huge improvement in sustainable technology, has motivated the emergence of high-level change such as the electrification and hybridization of aircraft propulsion [1–3], the serious consideration of hydrogen or synthetic fuel for flight and ground transportation [4–7], and the integration of significant renewable energy production in grid power around the globe [8].

All these new aircraft and grid architectures will require – as fully emission-free technologies phase in – a highly efficient, fuel-flexible, scalable thermal powerplant at their core, either for its unbeatable power density or reliable base-load energy production. As emission regulations tighten and sustainable, expensive fuels become the norm, the development of high-efficiency, high-temperature turbine rotors remains relevant to the future of turbomachinery.

The high temperature tolerance of ceramics makes them an attractive candidate for use throughout new-generation turbine hot section components, and much progress has been made in that regard. However, the integration of ceramics in a turbine rotor is no mean feat and has been intensely investigated in the later part of the 20th century. One critical concern that emerged from the attempts at integrating ceramic blades in turbine rotors has been blade structural reliability, which has proven insufficient for serious consideration in commercial products. At the University of Sherbrooke, in partnership with Exonetik Turbo, development of the inside-out ceramic turbine has been underway for the better part of the last decade [9–14], with this goal in mind: change the turbine blade structure paradigm. Over time and following economic trends, this has morphed into an endeavour to integrate ceramics into a potentially relatively low-cost, highly reliable rotor. The inside-out geometry, pictured in Figure 1.1, illustrates the current development of the ceramic turbine rotor as envisioned by the researchers, named the Inside-Out Ceramic Turbine (ICT). This rotor uses a composite carbon fiber hoop to maintain the blades in a compressive state. More details about this configuration are given in Chapter 2.

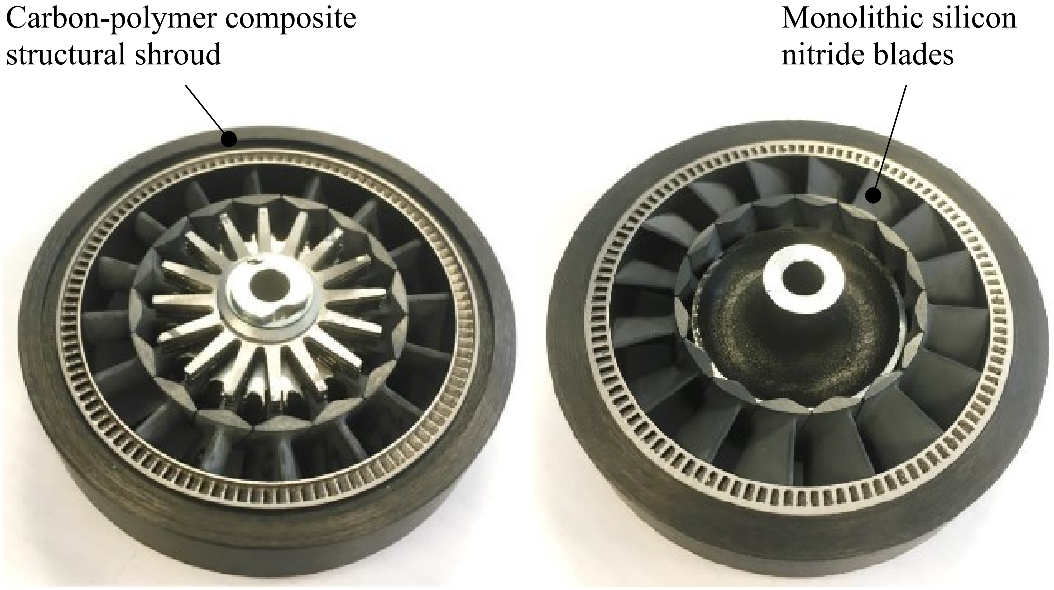

Figure 1.1 Current design iteration of the inside-out ceramic turbine (ICT) developed at University of Sherbrooke

1.2 Research Question and Goals

While testing the different iterations of the ICT rotor, blade cracking was noticed under certain loads. Considering that reliability is one of the cornerstones of turbines and aircraft in general, this was a concern and a potential hindrance to the development of ICT technology. The Federal Aviation Administration has stringent recommendations for critical component reliability [15], depending on aircraft weight and number of engines, shown in Table 1.1. This table is included to give an idea of the type of consequences critical engine failure can cause. The likely effects are kept in black-on-white in the table, as it is estimated a severe ICT rotor failure would most probably cause a hazardous or catastrophic failure of the aircraft. These probability figures concern the entire airplane, so blade failure is one failure cause among many. This gives more reason to reduce probability of failure for ICT rotor blades.

Table 1.1 Maximum allowable probabilities per flight hour (adapted from [15])

	Failure type			
	Minor	Major	Hazardous	Catastrophic
Effects on aircraft	Slight reduction in functional capabilities or safety margins	Significant reduction in functional capabilities or safety margins	Large reduction in functional capabilities or safety margins	Normally with hull loss
Effects on passengers	Physical discomfort for passengers	Physical distress to passengers, possibly including injuries	Serious or fatal injury to an occupant	Multiple fatalities
Effects on crew	Slight increase in workload or use of emergency procedures	Physical discomfort or a significant increase in workload	Physical distress or excessive workload impairs ability to perform tasks	Fatal injury or incapacitation
Aircraft type				
Class II Single or multiple turbines, < 6000 lbs	10^{-3}	10^{-5}	10^{-6}	10^{-7}
Class III Single or multiple turbines, > 6000 lbs	10^{-3}	10^{-5}	10^{-7}	10^{-8}
Class IV Commuter aircraft	10^{-3}	10^{-5}	10^{-7}	10^{-9}

This leads to the research question:

How can tensile stresses be reduced in ICT rotor blades?

The following primary and secondary goals are derived from this question:

1) Determine and quantify the main causes of potential failure in ICT rotor blades.
    a) Observe where failure occurs and identify the plausible root causes
    b) Develop a finite element model for comparing the effects of the identified causes
2) Imagine and test solutions which could address and reduce the probability of failure.

a) Gain a preliminary assessment of solutions suitability in a laboratory environment

b) Test the solutions in an ICT rotor

These goals set the roadmap for the research project, which culminated to the contributions in the following section.

1.3 Contributions

The following original contributions that emerged from this work are as follows:

1. **Identify the frictional interfaces as a reliability issue in ICT blades**, namely at the contact between the ceramic blades and metallic supporting components. The high-force contact of the blade tip with the structural shroud, illustrated in Figure 1.2, is central to the design of ICT rotors.

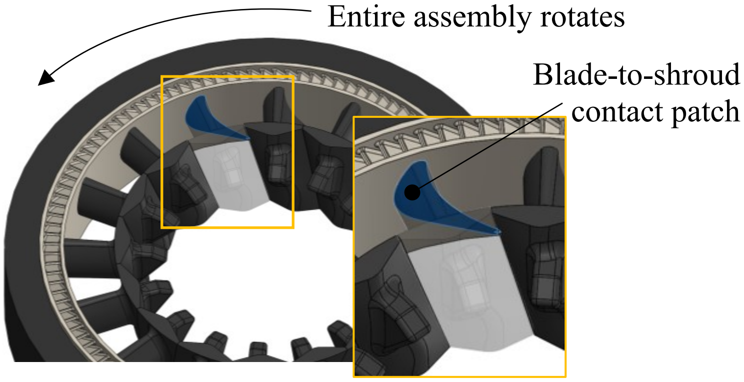

Figure 1.2 The high-normal-force contact between the blade tip and the structural rotating shroud, critical to the ICT architecture, is shown in blue (hub is not shown)

2. **Identify and quantify the contributions of the main variables to the stress state at the blade tip**, namely hoop strain, thermal expansion mismatch and coefficient of friction. These variables have interdependent effects which are quantified through a simplified model. The studied interface is unique to the ICT rotor configuration. The work done allowed to get a better understanding of the physics of the issue at hand, and chart a path to potential solutions.
3. **Experimentally investigate thermal barrier coating (TBC) and hexagonal boron nitride coating (hBN) as potential solutions to address the issue**, through a series of laboratory tests validating resistance to high normal force and high-temperature

operation. Both coatings are already quite common, with TBC being the most commonplace in turbomachinery. hBN is mostly used as a high-pressure lubricant and has been used in turbines in the past.

1.4 Thesis Outline

This thesis is a combination of traditional and paper-based. It starts with a brief state of the art of ceramics in turbomachinery and the ICT's inception, followed by three chapters:

3) Chapter 3 is a paper titled "Benefits and Challenges of the Inside-Out Ceramic Turbine: An Experimental Assessment". This paper completes the state of the art, presents the ICT working principle and compares two designs. From the experimental results obtained from both designs, it was determined that friction at the blade tip leads to a tensile stress state, which dominates probability of failure. The paper was published in AIAA Journal of Propulsion and Power.
4) Chapter 4 is a traditional chapter consisting of previously unpublished work. A simplified model is analyzed through a Design of Experiments (DOE) approach, to assess which design variables have the most significant impact on blade reliability. Coefficient of friction, rotational speed and thermal expansion mismatch stand out as important variables.
5) Chapter 5 contains experimental work published at the ASME Turbo Expo 2021, in a paper titled "Thermal Barrier Coating Applied to the Structural Shroud of an Inside-Out Ceramic Turbine". This section focuses on the experimental assessment of TBC to partly address the findings in. TBC was found to significantly reduce heat flux in the ICT and could allow a control on thermal expansion mismatch.
6) Chapter 6 is a traditional chapter which focuses on the experimental investigation of a second coating, hBN, which could reduce coefficient of friction at the interface, also to address findings in Chapter 4. hBN was found to provide a significant reduction in frictional stress levels in a high-preload test rig. This could allow a more forgiving interface between the blades and their supporting metallic components.

Finally, the work is wrapped up in a set of conclusions and recommendations on the path forward for improving blade reliability in an ICT.

CHAPTER 2

BACKGROUND

Complex, integrated blade cooling is out of bounds for low-cost, small-scale, high thermal efficiency turbines. Thus, designers must look outside of the superalloy material base from which they typically choose. More specifically, engineering ceramic blades could offer a far superior resistance to high temperature than uncooled nickel-based superalloys. This paradigm shift began in the 1970s, with several government and private programs throughout the world funding development in refractory materials. Several initiatives targeted the automotive industry, stemming from government programs, for the development of ceramic microturbines and were ultimately killed off due to high cost, a lack of modeling tools, the poor reliability of 1970-vintage ceramics, and vapor-induced material degradation. Since then, important breakthroughs were achieved in both brittle material modeling and the improvement of ceramics' mechanical properties and coatings. This has led to ceramics being recently introduced in static components in mid- to large-scale turbines.

2.1 Ceramics in Turbines: Structural Challenges

Turbine rotors are particularly difficult to convert to ceramics because of the tensile loads applied to the blades. Radial and tangential stresses σ_r and σ_θ levels throughout the disk are proportional to density ρ and tip speed ωR squared:

$$\sigma_r, \sigma_\theta \propto \rho(\omega R)^2 \tag{2.1}$$

Density in ceramics is typically lower than superalloys, but tip speed is invariably high in high temperature microturbines, making $\sigma_r, \sigma_\theta \gg 0$ and therefore the stress state in classic ceramic turbine rotors are fundamentally tensile.

Ceramics are highly sensitive to tensile loading, as their brittleness means that crack growth is hardly inhibited. Crack growth in ceramic components is a concern due to the inevitable presence of manufacturing-induced flaws which act as crack initiation sites. Tensile loading has been the pitfall of past trials to get monolithic ceramic rotors to surpass the performance of uncooled metallic turbines [16]. Furthermore, ceramic components under constant stress suffer from subcritical crack growth (SCG), which reduces part life considerably. SCG is related to fracture toughness and is dependent on both the material and its operating environment.

Because defects have a dominant impact on material strength and part life, material test data must be treated stochastically, and the designer must use statistical tools to develop components. The Weibull distribution, specifically developed for brittle material reliability, best represents probability of failure of a ceramic component. Probability of failure P_f, based on the two-parameter Weibull crack density function – Weibull modulus m and distribution parameter σ_0 – for a given stress σ, adjusted for fatigue and polyaxial loading, is used in the literature:

$$P_f(\sigma) = 1 - e^{-\left(\frac{\sigma}{\sigma_0}\right)^m} \tag{2.2}$$

Test specimen geometry and volume are considered when determining Weibull properties. P_f increases with total stressed volume, analogously to how a longer chain will have a higher probability of containing a very weak link. This prompts the designer to reduce part size and avoid large highly stressed components. Currently, monolithic part size is limited to a characteristic length of roughly 20 cm [17].

Conversely, a purely compressive state results in $P_f = 0$. This is derived from the fact that compressive loading inhibits crack growth, resulting in compressive strength generally one order of magnitude higher than tensile strength, making compressive failure a rare concern. Compressive loading is where engineering ceramics truly excel and what ceramic component designers strive towards.

Through finite element (FE) modeling, the designer can now determine the stress field in the component, provided meshing is sufficiently fine to fully capture the local stress states. The emergence of post-treatment software such as CARES/LIFE allows to interpret FE results and estimate P_f for a given operating time under a certain stress field, including material Weibull and fatigue properties [18].

On a more practical note, and alongside these advances in modeling tools, it was quickly discovered that toughness and strength were an issue for making turbines out of 1970-vintage ceramics. After iterative improvements in microstructure, fabrication process and chemical composition by key suppliers to the aero industry, silicon nitride (Si_3N_4) was heralded as the most versatile, toughest, strongest, and promising monolithic ceramic. However, field testing of silicon nitride components by many OEMs revealed the unreliability and catastrophic failure mode characteristic to monolithic ceramics. FOD-driven failure and SCG prompted researchers and OEMs to enhance toughness K_{Ic}, typically 4 to 8 $\mathrm{MPa}\sqrt{\mathrm{m}}$ in monolithics [19,20].

Toughness-oriented research efforts in Japan led to the manufacturing of silicon carbide (SiC) in long fiber form. This, coupled with a SiC matrix, was the major enabler for the emergence of SiC/SiC ceramic matrix composites (CMC), or continuous fiber ceramic composites (CFCC). CMCs inhibit crack propagation and tolerate a certain amount of fiber slip, thus allowing the material to fail gracefully, as opposed to the typical catastrophic failure exhibited by monolithics. SiC/SiC CMCs are the object of the most current research and have all but replaced monolithics as contenders to the next turbine material of choice. Years of development in proprietary fiber coatings and composite manufacturing processes mean CMCs are currently mainly used and developed by major aero OEMs. Although it dramatically increases apparent fracture toughness K_{Ic}, the composite nature of CMCs means flexural strength is lower than monolithics. Some military turbofan engines now have CMCs in low-pressure rotating components [21], and many have started integrating as well as static components [22,23].

The modeling and manufacturing of complex geometries is challenging and costly, due to the added complexity of designing and layering of the anisotropic ceramic fiber fabric [24–26]. Monolithic ceramics present the significant benefit of being simpler to manufacture to a near net-shape of intricate aerodynamic geometries [27,28], which is especially relevant at the scale and cost-levels required for smaller turbines.

Issues of chemical interaction with their environment are also of concern for engineering ceramics in the oxidizing environment of gas turbines. The formation of water vapor in the combustion process causes significant recession of silicon-based ceramics [29]. The silica scale formed on the surface is not stable and current work is largely focused on coatings for protecting silicon-based ceramics from dramatic recession and achieving sufficient part life [30–32]. Work in this thesis does not address this specific issue, but rather aims at relieving critical stress levels in the ceramics blades.

2.2 ICT Rotor Configuration

Although brittle, ceramics have extraordinary strength in compression. This is exploited in the inside-out architecture. Figure 2.1 shows a conceptual illustration of the three main rotor concepts that have been tested in the literature: (a) a single-piece, bladed disk, or “blisk”, (b) dovetailed ceramic blades in a slotted disk and (c) an inside-out rotor, which relies on an additional component: a structural rotating shroud.

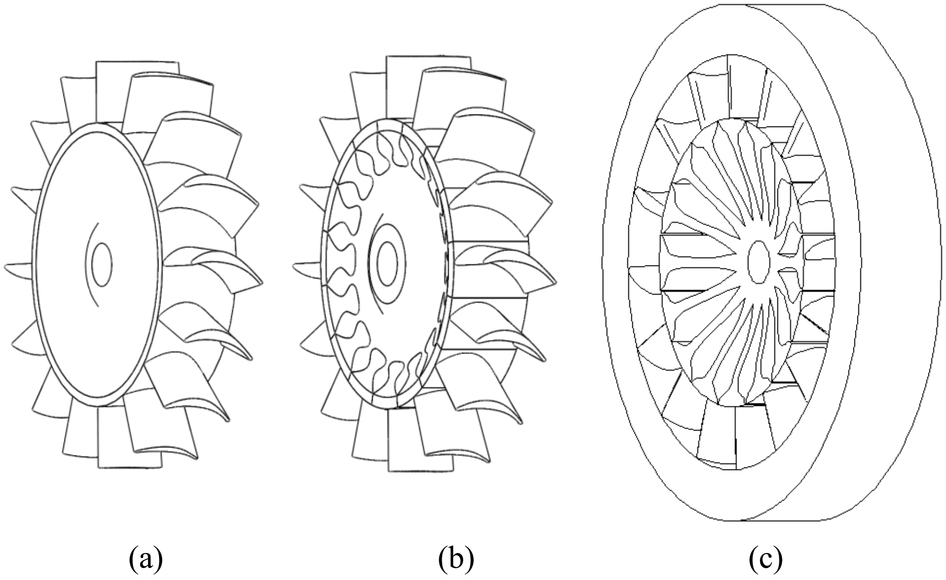

Figure 2.1 Three ceramic turbine rotor concepts: (a) integral bladed disk, (b) rooted individual blades and (c) inside-out configuration.

Blisks are integral molded monolithic ceramic rotors that incorporate both rotor functions into one part. Rooted dovetail or fir-tree assemblies enable the decoupling of the blade geometry from the hub. The inside-out configuration holds ceramic blades in place from the tip. This configuration uses the centrifugal field in the rotor to press the blades against an outer, rotating, continuous structural shroud, similarly to the hoops used for the containment of high-energy flywheels. The inside-out design discussed in this thesis is first introduced in Ref. [33], based on past innovations stemming from work at University of Sherbrooke using the structural shroud [34,35,13,11,36–38].

To illustrate the conceptual effect the ICT configuration has on ceramic blades, Figure 2.2 shows the maximum and minimum principal FE stress results, σ_1 and σ_3, of an inverted taper blade at a tip speed of 500 m/s. Radial body motion is prevented at the tip in the r axis – motion is permitted in the θ-z plane – and loading is purely centrifugal. The blade is a simple radial extrusion and FE calculations are performed in ANSYS Workbench.

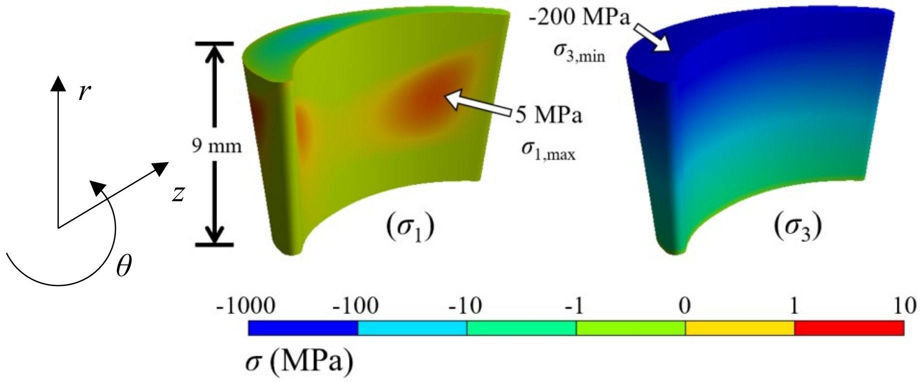

Figure 2.2 FE maximum (σ_1) and minimum (σ_3) principal stress distribution ($\log_{10}$ scale) in an inverted taper Si_3N_4 ICT blade at a tip speed of 500 m/s

This analysis does not include real blade boundary conditions and serves to showcase the advantage held by the inside-out configuration over traditional configurations. In operation, the blade is in an overall purely compressive stress state, greatly inhibiting crack propagation. Maximum tensile stress values are potentially two orders of magnitude lower than dovetail or blisk blades, which tend toward 200 MPa local stress values [39]. This means that sensitivity to increased tensile loading, such as upon impact or overspin, is reduced or cancelled. Creep rate is also reduced by the blade's compressive stress state, by approximately one order of magnitude [40]. True boundary conditions could induce tensile stresses, however these stresses were thought to be of a secondary nature. A more in-depth explanation and history of the inside-out configuration is given in Section 3.5, as part of a paper published in the AIAA Journal of Propulsion and Power [41].

With the advent of next-generation hybrid powertrains and ever more strict emission standards, for both stationary and mobile applications, there is a renewed need for high-efficiency, high-density powerpacks. The wealth of knowledge brought by industry and academic research in ceramics modeling and testing makes a compelling case for the renewed development of a turbine rotor configuration that overcomes the structural challenges of monolithic ceramics and enables their use in microturbines. The following chapters cover the benefits and the challenges of the inside-out ceramic turbine developed at University of Sherbrooke, in this regard.

CHAPTER 3

ICT BLADE TIP STRESSES

3.1 Foreword

As discussed in Chapter 2, it is not trivial to integrate ceramics in turbine rotors. Work done in this regard has spanned decades and has yielded a great deal of relevant scientific discoveries but has not resulted in the promised ceramic turbines. The ICT aims at changing the design paradigm of turbine rotors to integrate technical ceramics in a novel way. However, for this new paradigm to gain mainstream traction, it must prove that it has a positive impact on stress levels, which could alleviate the difficulties found in past development attempts.

Work presented in this chapter was published as a research paper and aims at identifying sources of stress in ICT blades, through a combination of finite element analyses and experimental results centered around the ICT blade. The paper starts with a literature review of design paradigms for converting metallic turbine rotors to ceramics. The study presented here reveals that the main challenge concerning ICT blade reliability is its contact with supporting components. The thermal expansion mismatch and the strain induced by centrifugal loading differ between the ceramic blades and the metallic components in direct contact with it. This generates tensile stress at the interface, as strain in the metallic components is superior to that in the ceramic blades. This is supported by comparative experimental findings, between a design which fully clamps the blade and one which frees the blade base: the design which has two high-pressure interfaces failed whereas the design with a free blade base did not. Numerical findings also point to a dominant stress field at the interface, with probability of failure 5 to 10 orders of magnitude higher at the stressed interfaces. The conclusions from this paper serve as a starting point for addressing potential blade failure in the ICT blades in the following chapters of the thesis.

- **Title**: Benefits and Challenges of the Inside-Out Ceramic Turbine: An Experimental Assessment

- **Authors**:
    - Patrick K. Dubois, PhD candidate, University of Sherbrooke, Faculty of Engineering, Createk Innovation Group (Contributions: Design, analyses and conclusions)
    - Céderick Landry, PhD candidate, University of Sherbrooke, Faculty of Engineering, Createk Innovation Group
    - Dominik Thibault, Master's student, University of Sherbrooke, Faculty of Engineering, Createk Innovation Group
    - Benoît Picard, Chief Engineer, Exonetik Turbo Division
    - Jean-Sébastien Plante, Professor, University of Sherbrooke, Faculty of Engineering, Createk Innovation Group
    - Mathieu Picard, Associate Professor, University of Sherbrooke, Faculty of Engineering, Createk Innovation Group

- **Date of acceptance**: July 5th, 2021
- **State of acceptance**: Accepted, published online August 31st, 2021.
- **Publication**: Journal of Propulsion and Power
- **Reference**: Dubois, P.K. et al., 2021, "Benefits and Challenges of the Inside-Out Ceramic Turbine: An Experimental Assessment," Journal of Propulsion and Power, Ahead of press.
- **Version**: Final, as accepted. Adapted to institutional thesis format. Some minor clarifications are made.

French title

« Avantages et défis des turbines à pales en céramique en configuration renversée : une évaluation expérimentale »

French abstract

La propulsion distribuée pour les aéronefs a renouvelé l'intérêt pour les groupes motopropulseurs à forte densité de puissance et à haute efficacité. Les turbomachines en céramique pourraient jouer un rôle majeur, bien qu'aucune conception réussie n'ait été réalisée pour les rotors de microturbine. Le chargement des pales du rotor est en tension, un obstacle à la conversion en céramique. Le rotor de turbine en céramique à configuration renversée (ICT)

utilise les propriétés supérieures en compression de la céramique monolithique, en supportant les pales en céramique contre un carénage rotatif en composite structurel. Cela permet de faibles niveaux de contrainte dans toute la pale, augmentant la fiabilité et prolongeant la durée de vie. Une démonstration expérimentale de deux conceptions ICT a été réalisée avec des prototypes à l'échelle de 15 kW pour identifier les problèmes critiques : (A) un moyeu flexible qui serre les pales contre le carénage structurel et (B) une configuration à pales coulissantes qui permet un déplacement libre de la pale. La conception du moyeu flexible a été testée jusqu'à 1000 °C. L'intégrité du rotor a été préservée, mais de la fissuration locale de la pale s'est produite. La conception à pale coulissante a été testée avec succès jusqu'à 1 100 °C pendant plus d'une heure à une vitesse de bout de pale de 350 m/s sans aucun problème. Le chargement en tension aux interfaces céramique/métallique reste le principal défi à relever. La réduction du frottement devrait surmonter la fissuration des pales et permettre à l'ICT proposée d'atteindre la température cible de 1275 °C et une vitesse de bout de pale de 425 m/s.

Benefits and Challenges of the Inside-Out Ceramic Turbine: An Experimental Assessment

3.2 Abstract

Distributed aircraft propulsion has renewed the interest in power-dense, high-efficiency powerpacks. Ceramic turbomachinery could be a major enabler, although no successful design has been achieved in microturbine rotors. Rotor blade loading is tensile and a hurdle for successful conversion to ceramics. The inside-out ceramic turbine (ICT) rotor uses the superior compressive properties of monolithic ceramics, by supporting ceramic blades against a structural composite rotating shroud. This enables low stress levels throughout the blade, increasing reliability and extending service life. An experimental demonstration of two ICT designs was conducted with 15-kW scale prototypes to identify critical issues: (A) a flexible hub which clamps blades against the structural shroud and (B) a sliding-blade configuration which allows free displacement of the blade. The flexible-hub design was tested up to 1000 °C. Rotor integrity was preserved, but local blade cracking occurred. The sliding-blade design was successfully tested up to 1100 °C for over 1 hour at a tip speed of 350 m/s with no issue. Tensile loading at the ceramic/metallic interfaces remains the key challenge to address. Reducing friction should overcome blade cracking and allow the proposed ICT to reach the targeted temperature of 1275 °C and tip speed of 425 m/s.

3.3 Nomenclature

B	Static fatigue parameter
CTE	Coefficient of thermal expansion
DOD	Domestic object damage
FOD	Foreign object damage
m	Weibull modulus
N	Static fatigue parameter
P_f	Probability of failure
SCG	Subcritical crack growth
V	Part volume
σ_i	i^{th} principal stress

σ_0	Material characteristic strength
ϑ	Part service life

3.4 Introduction

Turboelectric distributed propulsion (TeDP) is an upcoming aircraft propulsion architecture, which could significantly reduce fuel burn and emission levels for commercial aircraft [42]. Several technological breakthroughs must occur in order for TeDP aircraft to supersede traditional podded turbofan aircraft, notably the improvement of high-speed electric motors in conjunction with high-efficiency, lower-output, power-dense gas turbines [43,44]. Future eVTOL vehicle concepts and UAVs, as well as current turbine- and piston-engine-powered regional and business aircraft and turboshaft helicopters will benefit from the improvement of turboelectric technology powered by a new generation of efficient small gas turbine engines.

Turbines with an output of the order of 1 MW – microturbines – suffer important losses at the high pressure ratios at which large aero turbines operate, which heavily penalize cycle efficiency due to size effects [45]. To reach higher efficiencies, microturbines typically operate under the recuperated Brayton cycle. In a recuperated cycle, high thermal efficiency is achieved by maximizing turbine inlet temperature (TIT) at a relatively low pressure ratio, typically between 5:1 and 10:1 [46]. This reduces the number of compressor and turbine stages and avoids loss mechanisms associated to high-pressure flows in small gas paths. The introduction of a heat exchanger affects powertrain weight, however the high thermal efficiency increases propulsion system total power density, thus offering performance gains in longer missions [47].

Microturbines typically rely on uncooled, low-cost components, limiting TIT despite highly TIT-dependent thermal efficiency. Introduction of current advanced cooling techniques used in high-output gas turbines would decrease exhaust temperature by diluting coolant air in the main flow, penalizing cycle efficiency. In order to achieve sufficient thermal efficiency at reasonable power density, and thus be truly competitive in small aircraft and future small TeDP architectures, an undiluted temperature of 1275 °C is a desirable target TIT value [48]. This roughly represents a 300 °C increase over the current achievable TIT for uncooled metallic turbines.

A significant, cost-effective increase in TIT requires a shift in design paradigm. Modern engineering ceramics have been widely appraised as the leading material family to achieve high performance at low cost in numerous high-temperature applications. Although it is no trivial matter to incorporate ceramics into turbomachinery, it remains the most promising approach to significantly increase TIT for MW-scale turbines, due to the impracticality of integrating traditional cooling techniques.

Turbine rotors are notoriously difficult to convert to ceramics, due to the tensile loading applied to the blades. Ceramics brittleness means that crack growth is hardly inhibited. Crack growth in ceramic components is a concern due to the inevitable presence of manufacturing-induced flaws which act as crack initiation sites. Furthermore, ceramic components under constant stress suffer from subcritical crack growth (SCG), which reduces part life considerably in a turbine’s extreme environment.

The rotor has two basic components: (1) a set of airfoils, or blades, to extract the energy from the hot air flow, (2) an intermediate component (e.g. a hub) that structurally couples the airfoils to an output shaft. This may seem trivial; however, no reliably successful approach has been achieved in the literature to use ceramics for these components. Figure 2.1 illustrates four rotor configurations and their blade free body diagrams: (a) a single-piece, integral bladed disk, or blisk, (b) and (c) dovetailed ceramic blades in a slotted disk and (d) an inside-out ceramic turbine (ICT) rotor, which relies on an additional component: (3) a structural rotating shroud.

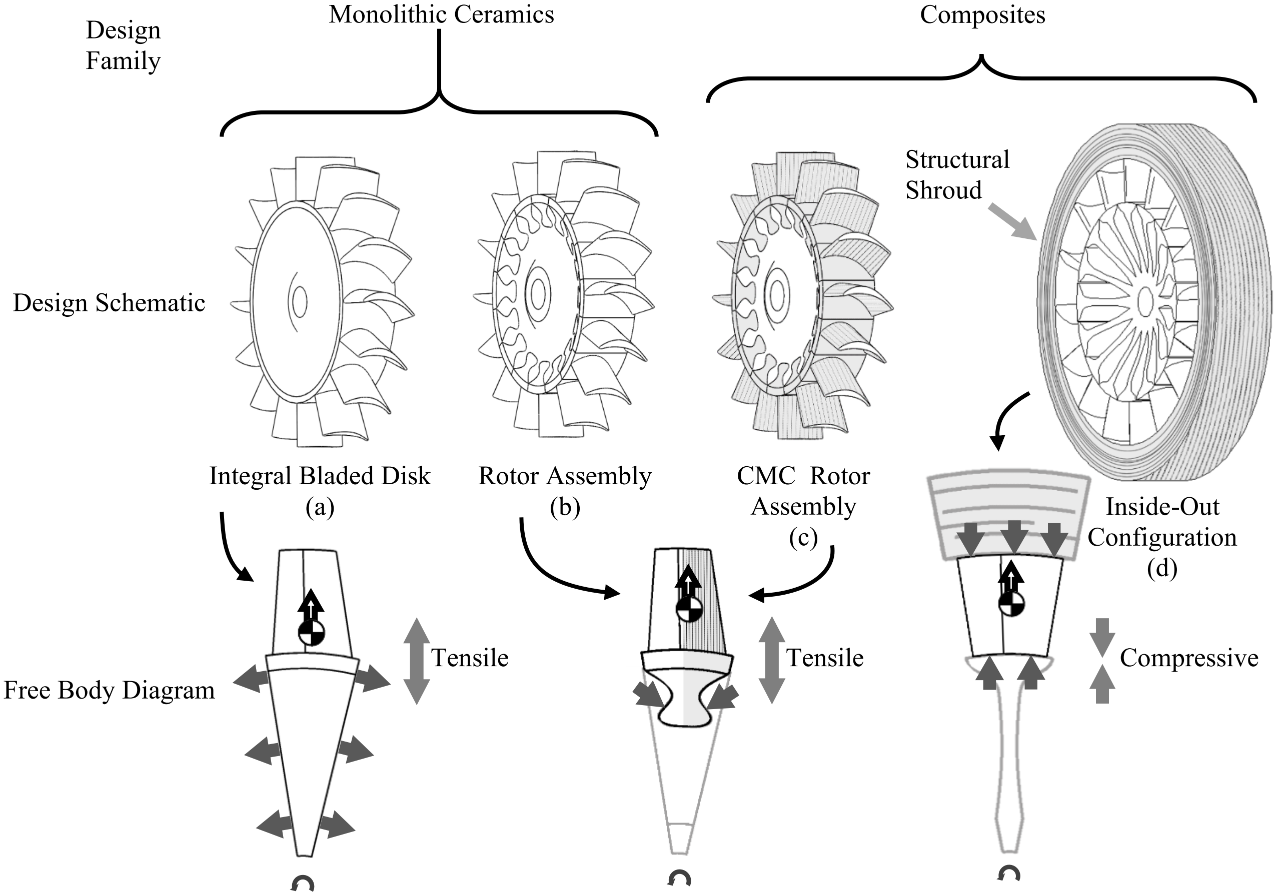

Figure 3.1 Ceramic turbine rotor design paradigms. Only the inside-out configuration (d) maintains compressive loading on ceramic blades.

Blisks are integral molded monolithic ceramic rotors that incorporate the airfoils and hub into one part. Testing in the past has proved this architecture can cumulate several hundred hours of testing time [49,50]. However, it is comprised of a voluminous stressed ceramic part, prone to breaking during operation or manufacturing [51,52,28]. Additionally, this configuration is sensitive to foreign or domestic object damage (FOD/DOD), which results in failure of the prototype under test due to cascade blade failure [53]. FOD sensitivity is inherent to the blade boundary conditions and associated bending stresses [54].

Rooted dovetail or fir-tree assemblies enable the decoupling of the airfoil components from the hub component. This configuration allows the designer to choose materials according to the function, resulting in ceramic-metallic rotors [55,56] and ceramic-ceramic rotors [57]. Fitting the blade to the hub generates local tensile stresses at the blade fixation feature. The main takeaway of the research that went into dovetail ceramic blades contact stresses was the requirement of a compliant interlayer system between the metallic hub and ceramic dovetail [56]. However, low FOD tolerance is still a major roadblock for rooted ceramic blades [53].

Toughness-oriented research efforts led to the emergence of ceramic matrix composites (CMCs). CMCs inhibit crack propagation and enable graceful failure, as opposed to the fragile failure exhibited by monolithics. CMCs however have lower flexural strength than monolithics [58,59], and modeling and manufacturing of complex geometries is challenging and costly [60]. These are significant hurdles for the integration of CMCs into rotating components, even at the high-output turbine scale, making trickle-down into microturbines improbable. An alternative approach must be attempted for the introduction of low-cost monolithics in microturbines.

The inside-out ceramic turbine (ICT) configuration uses the centrifugal field in the rotor to press ceramic blades tips against a rotating, high-strength, structural shroud. The addition of the structural rotating shroud translates into the fundamental benefit of compressive blade structural loading, resulting in significantly higher blade reliability and paving the way to the use of monolithic ceramic blades in turbine rotors. This configuration decouples tensile strength requirement from the airfoils, thus avoiding the complex manufacturing of composite blades.

Few iterations of ICT configurations have been attempted in the literature, with mitigated success and little physical demonstrations [61,62]. Prototypes failed, as they were exceedingly stiff, all-ceramic assemblies, relying on high interference fitting and prone to local stress hot spots. They did introduce a new failure mode for ceramic rotors: the compressive loading maintained global integrity of the rotor, despite cracking of the individual components. This indicates that failure concerns that motivated the development of CMCs could be superseded by ICT robustness. However, no convincing attempt at an ICT was achieved.

This paper presents a first numerical and experimental assessment of the benefits and challenges of two proposed ICT designs. Both introduce the use of compliant metallic components, though they differ at the ceramic blade interface with the rotor hub. Both ICT designs are presented with experimental results of 15-kW scale prototypes tested at TIT up to 1100 °C and tip speed up to 350 m/s. Experimental results indicate that the proposed ICTs can currently operate at the test conditions while resisting minor FOD events, and that blade interface with the compliant metallic components is the main challenge to be addressed for improving long-term ICT reliability.

3.5 ICT Rotor Designs

The inception of the ICTs explored in this paper is derived from a series of highly power-dense supersonic turbomachine concepts, relying on the rotating composite structural shroud [13,11,37]. This approach differs from the design process behind traditional blisk and dovetail configurations, which are adapted from or retrofitted to existing turbine geometries. The ICT blade is in a radially purely compressive stress state, resulting in a ceramic blade that could potentially never suffer from crack propagation. Creep rate is also reduced by the blade's compressive stress state, by approximately one order of magnitude compared to tensile loading [40]. The blades' tip support is also favorable to inverted tapering of the blade, thus allowing to potentially reduce the rotor inlet deviation angle. It is surmised that the compressive stress state of the blade should reduce tensile stress rise upon transient events such as FOD. Nevertheless, three main design challenges must be addressed to achieve a functional ICT configuration.

The first challenge is maintaining the contact at the blade root and tip at elevated operating speed. The rotating structural shroud supports the blades' apparent centrifuged weight as well as its own, thus inducing considerable hoop strain. The specific modulus and specific strength of the shroud must thus be very high. ICTs typically use wound carbon-polymer composite, used for applications which require such extreme specific properties [63]. As the hoop expands under centrifugal load, radial blade displacement becomes significant. This must be tolerated at the hub to continue transferring power to the shaft.

The two designs are presented in Figure 3.2. The flexible-hub ICT design (Figure 3.2, Design A) uses a flexible leaf spring hub to clamp the ceramic blades against the structural shroud and follow the blades' radial displacement. The blades are clamped at rest and throughout turbine operation, as centrifugal force applies to the hub spring fingers which load the blade base. The blade tip and base are both flat for uniform clamping force. The sliding-blade ICT design (Figure 3.2, Design B) uses a rigid hub with inclined planes on which individual ceramic blades slide outward and inward, according to centrifugal force magnitude. The blades are thus decoupled from the hub and operate under rigid body motion. A blade shoe is incorporated to this blade design, and passage height increase is possible along the blade base. A set of springs press upon the front of the blade shoe, which slides in the hub track, thus maintaining pre-load. Both blade designs are held in place through friction at the shroud interface.

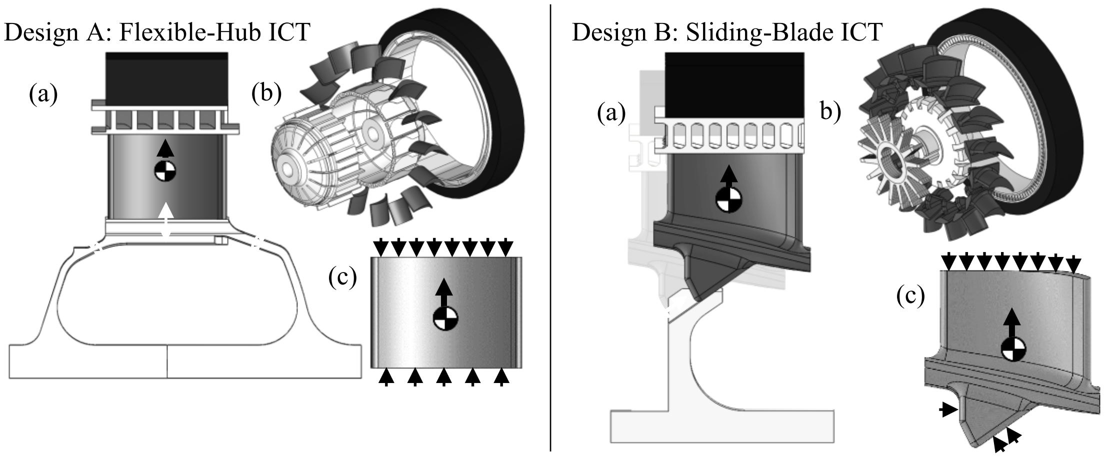

Figure 3.2 Designs A and B: a) blade motion compensation mechanism with the leaf-spring design and rigid-body motion with the sliding-blade design, b) components required in each configuration and c) blade free body diagram.

The second challenge is shielding the polymer-based composite structural shroud from the extreme temperature of the hot gas path. The polyimide matrix in the shroud has an operating temperature of roughly 345 °C and thus requires cooling. This means a significant thermal gradient must be achieved in a dedicated cooling layer between the blades and the shroud. This introduces a shrink-fit metallic cooling ring in the assembly, which is the focus of previous work of Courtois et al. [64]. Because the cooling flow is confined within a single layer running axially between the shroud and blade tips, it is possible to incorporate a dedicated cooling inlet and outlet, thus controlling mixing the main flow and the cooling flow and subsequent cooling of the exhaust gas temperature.

The third challenge is inducing as little tensile stresses as possible at the blade contacts. The blade is not bonded to the structural shroud, merely pressed against it, and compression is due to the normal force between its tip and the structural shroud's inner surface. Ceramics typically have a low coefficient of thermal expansion (CTE), which makes high-pressure contacts which undergo high variations in temperature prone to cracking [65]. Thus, friction between the blades and the shroud is a challenge, as the components expand at different rates under immense normal force.

3.6 Numerical Analyses

Preliminary coupled thermal and mechanical finite element (FE) analyses evaluate the expected structural performance each configuration – flexible-hub and sliding-blade – could achieve. CeramTec (Germany) SL200BG silicon nitride is used for the flexible-hub proof-of-concept prototype blade, for its low cost and rapid availability in the simple form factor required for that design. The complex shape of the sliding blade requires more advanced manufacturing knowledge and thus Kyocera (Japan) is selected to manufacture the prototype blades. SN235P grade silicon nitride is used for cost and availability reasons. Ceramic properties at room temperature, unless otherwise noted, are listed in Table 3.1. Stochastic ceramic properties are assumed to be in the same range as those in Ref. [66]. Metallic components are Inconel 718, with temperature-adjusted properties based on Ref. [67].

Table 3.1 Ceramic properties for the ICT proof of concept rotors

		CeramTec SL200BG	Kyocera SN235P
4-pt flexural strength, MPa	RT	850	880
	1000 °C	580[a]	600
Estimated Weibull modulus *m*		16	15
Estimated fatigue parameter *B*		400	
Estimated fatigue parameter *N*		20	
CTE, µm/m°C		3.2	2.6
Thermal conductivity, W/m°C		30	21
Density, kg/m³		3210	3200
Compressive strength, MPa		> 3000	

[a]Same proportional decrease in strength as Kyocera SN235P is assumed

The operating conditions are set at a TIT of 1026 °C and a rotational speed of 115 000 RPM. The boundary conditions for both the thermal and structural analyses are shown in Figure 3.3. Main flow temperature is assumed constant and convective heat transfer coefficients are taken from Ref. [68]. Rotor warm-up is done at half the final rotational speed, i.e. 57 500 RPM, to allow for thermal expansion before achieving full speed. The rotor hub base is cooled via the turbine shaft and the flexible hub has additional cooling channels running beneath the blade as well (not shown). Cooling of the composite hoop requires a cooling air mass flow around 20 g/s for the proof-of-concept prototypes [64] and its temperature increase along the channels is taken into account. This is roughly 17 % of the main flow, but it is expected that optimization, better thermal management, and a larger turbine scale should reduce this significantly.

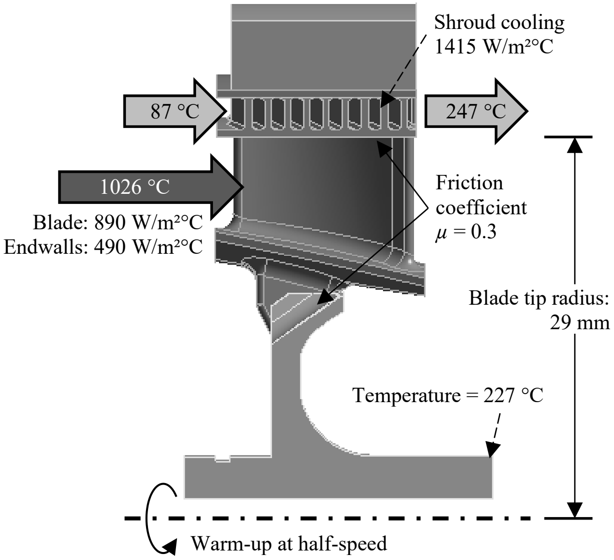

Figure 3.3 Boundary conditions for thermal and structural coupled FE analyses, identical for both designs (sliding-blade design shown)

FE Analysis results are shown in Figures 3.4 to 3.6. The intense cooling of the composite hoop causes a significant temperature gradient in the blade. This is due to the conductive heat flux which must be extracted to keep the composite hoop under 300 °C, and the hubs in the acceptable range for Inconel 718. The maximum achieved temperature for the blades is similar. Better thermal management in future iterations should allow higher temperatures to be achieved in the blades, at higher TIT.

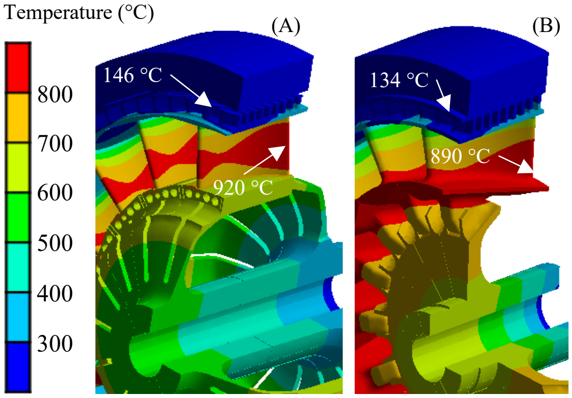

Figure 3.4 FE temperature distribution results for the (A) flexible-hub and (B) sliding-blade designs.

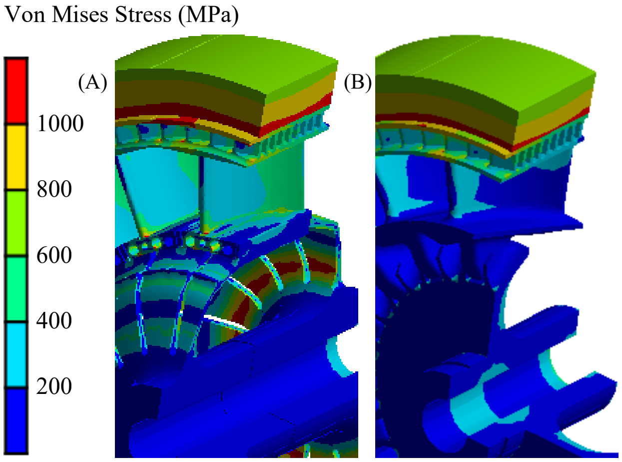

Figure 3.5 Rotor assembly Von Mises FE equivalent stress results for the (A) flexible-hub and (B) sliding-blade designs, at operating conditions

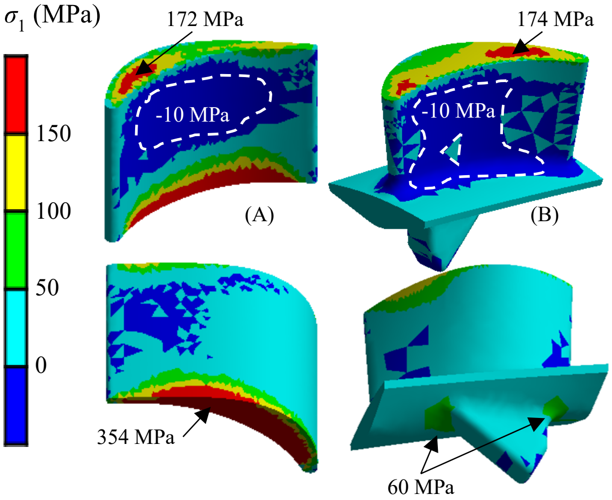

Figure 3.6 FE maximum principal stress (σ_1) results in the silicon nitride blade for the (A) flexible-hub and (B) sliding-blade designs

Figure 3.5 illustrates that the main stress in both rotor assemblies is located in the structural carbon hoop. Von Mises stress results are used to simplify the illustration, and hoop stress is so dominant that Von Mises and hoop stress results are in fact very close in the carbon hoop. The flexible hub is more stressed than the sliding-blade hub, as it undergoes larger radial deformation. The blades' maximum principal stress in both designs, illustrated in Figure 3.6, show a practically purely compressive core, with tensile stress rising at the high-load frictional contact with metallic components, i.e. the clamping hub and shroud in the flexible-hub design, and only the shroud in the sliding-blade design as the blade shoe is free. Tensile stress is caused by frictional interface stresses, due to the expansion mismatch between the blade and the supporting parts. This mismatch is caused by the difference in thermal expansion and centrifugal deformation, which are both greater in the metallic components than the silicon nitride blades.

Thermal expansion is dominated by the difference in coefficients of thermal expansion (CTE), which are typically 2-4 µm/m°C for silicon nitride and 12-17 µm/m°C for Ni-based superalloys. The CTE mismatch is amplified in the flexible-hub ICT design, as there are two frictional, high-temperature contacts of ceramic to metal, whereas the sliding-blade design only has one at the blade tip. Furthermore, in the flexible-hub design, the bottom interface is hotter, thus inducing much higher thermal expansion stresses, which are absent in the sliding-blade design. Centrifugal deformation causes significant hoop strain in the shroud, which adds to blade tip contact stresses in both designs.

Probability of failure P_f is calculated using the elemental mean stress in the blades, using the 2-parameter Weibull density function, in Eq (3.3).

$$P_f = 1 - e^{-\frac{1}{\sigma_0}\int \varphi^m dV} \tag{3.3}$$

where

$$\varphi = \sum_i \left[\left(\frac{\sigma_i^N \vartheta}{B} + \sigma_i^{N-2} \right)^{\frac{1}{N-2}} \right] \tag{3.4}$$

where σ_i is the principal stress value in direction $i = \{1,2,3\}$, dV is element volume, σ_0 is the material characteristic strength, m is the Weibull modulus, B and N are static fatigue parameters and ϑ is service life. Integrated across the blade for all positive principal stress values according to the principle of independent action (PIA), P_f results are listed in Table 3.2.

Table 3.2 Single ceramic blade probability of failure

Time	Flexible-hub design	Sliding-blade design
1 minute	8.4×10^{-5}	8.5×10^{-9}
1 hour	0.031	2.6×10^{-7}
1000 hours	1.0	8.2×10^{-5}
1000 hours, blade core only[b]	$< 1.0 \times 10^{-10}$	3.0×10^{-10}

[b] Excludes blade contact stresses, see Figure 3.7

When the highly stressed blade extremities are removed – regions >150 MPa in Figure 3.6, resulting in the blade core illustrated in Figure 3.7 – P_f falls by a significant amount, indicating clearly that the blade core compressive state is a major benefit, and that high-pressure blade interfaces with surrounding components is a key issue.

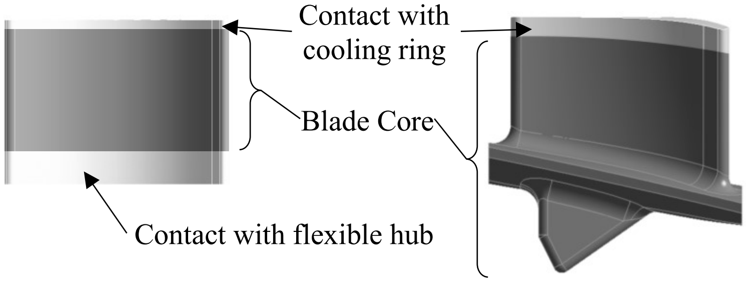

Figure 3.7 Blade core used in Table 3.2, high stress comes from identified contact zones

Results in Table 3.2 also suggest an inherent advantage of the sliding-blade design over the flexible-hub design, as there is only one interface to address, i.e. the blade tip, even if it does come at the cost of inducing low tensile stresses around the blade foot. The sliding-blade design's advantage is particularly obvious in long service-life results in Table 3.2, which indicate a 16-blade rotor would have a 99.9% chance of achieving 1000 hours. It must be noted that the long-term P_f are approximate values, sensitive to the estimated parameters B and N, thus this serves only as an indication to the reader. Considering this is a friction-based, non-linear issue, which is greatly affected by true test conditions and material properties, experimental evaluation was undergone to validate the modeling of this critical interface, as well as to determine whether other issues could emerge.

3.7 Experimental Assessment

Both designs were prototyped and tested to validate their structural and thermal resistance under representative operating conditions. The prototype structural shrouds are tape-wound Hexcel IM7 carbon fiber in a polyimide matrix, at 74.6 mm OD. The shroud cooling layer is a shrink-fit DMLS 3D-printed Inconel 718 ring with helix cooling channels. The hubs were DMLS 3D-printed Inconel 718 in both designs. The flexible-hub prototype used simplified CeramTec SL200BG silicon nitride blades, whereas the sliding-blade prototype used Kyocera SN235P 5-

axis machined silicon nitride blades. Blades were machined in the green state. Critical surfaces were ground post-firing. Both blades are shown in Figure 3.8.

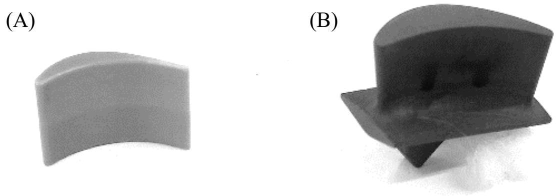

Figure 3.8 (A) Straight CeramTec SL200BG blade used in the flexible-hub prototype and (B) 5-axis machined Kyocera SN235P blade used in the sliding-blade prototype

The hot spin test rig is shown in Figure 3.9. A Garrett GTX2860R automotive turbocharger compressor wheel is coupled to the ICT prototype for the main flow. The cut view in Figure 3.10 shows the flows specific to the ICT configuration: the composite rim cooling layer, the main hot gas path and the hub cooling flow.

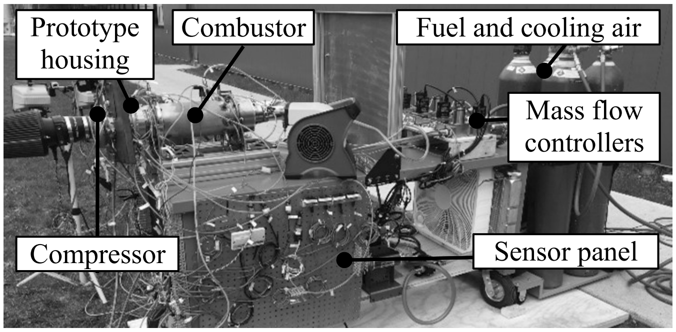

Figure 3.9 High temperature test rig, fueled with hydrogen/propane mix, using an automotive compressor

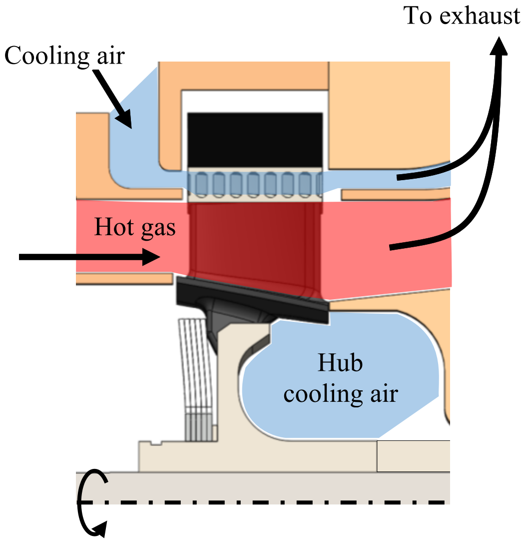

Figure 3.10 Flow paths in the turbine test rig (sliding-blade design shown)

Hub cooling is rudimentary in this assembly, as current work is not focused on auxiliary flow economy. The combustor is fueled by a hydrogen/propane mix. The shroud-cooling flow is supplied by an external compressor. The turbocharger ball bearings squeeze films are used for damping. A capacitive sensor measures rotordynamics response at a 10 kHz sampling rate. Rotational speed is measured by the turbocharger eddy current speed sensor and validated using fast Fourier transform on the capacitive sensor's signal. Temperature and pressure in the main stations in the test rig are respectively measured with Omega TJ36 thermocouples and SSI Technologies pressure sensors, recorded at 80 Hz. Maximum TIT achievable by the test rig is 1100 °C.

Test procedure included rapid initial heating of the turbine wheel, at low rotational speed. This allows the bulk of the thermal expansion of the components to occur at low centrifugal loading, thus inducing less frictional stress in the assembly as rotational speed subsequently increases. Tests were conducted for intervals 2-5 minutes long for preliminary assessment, followed by longer test duration up to 1h for the sliding-blade prototype.

A. Results with flexible hub

Preliminary tests were run at room temperature up to 287 m/s, with no damage to any of the components. TIT was then increased to 720 °C, at a tip speed of 300 m/s, for a total of 14 minutes, with no degradation of the rotor assembly. An uncooled hub was used at this stage. The combustor used in these tests degraded rapidly, sending molten fragments on the silicon nitride blades, as shown in Figure 3.11. This high-temperature DOD event caused no problem with the ceramic blades.

Figure 3.11 Silicon nitride blades speckled with melted combustor debris (DOD) after preliminary testing at a TIT of 720 °C and tip speed of 300 m/s

All subsequent tests on the flexible-hub prototype were done with the cooled hub shown in Figs. 3.1 and 3.13, as well as a revised combustor, for higher temperature testing. The rotor was tested at 800 °C TIT for a 40-second run with no damage. Subsequently the prototype was tested at 1000 °C TIT and a tip speed over 325 m/s, for a 2-minute and a 5-minute run, with hydrogen fuel. Figure 3.12 shows the temperature and blade tip speed graph of the 5-minute test run. Testing was interrupted due to hydrogen fuel depletion.

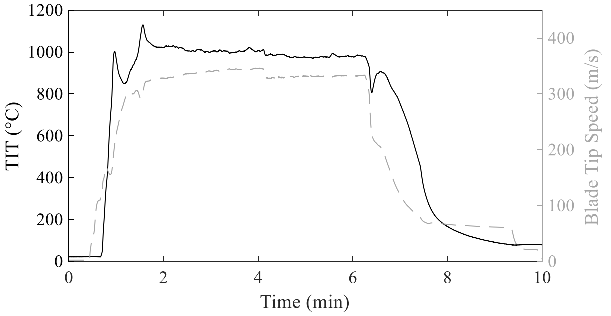

Figure 3.12 5-minute test run at 1000 °C TIT and over 325 m/s blade tip speed for revised flexible-hub prototype.

Visual inspection after the high-temperature 2-minute and 5-minute runs did reveal that fine cracking, initiating radially from the blade tip and base, had occurred on all silicon nitride blades during both tests. This failure indicates that the model was correct in predicting a relatively high P_f for the flexible-hub design, even for short test durations. The hub and shroud supported the blades in their cracked state and no rotor failure occurred. One blade leading edge was missing. Figure 3.13 shows the flexible-hub prototype after the high-temperature runs. Cracks are coherent with Figure 3.6: blade extremity contact stresses cause a crack to open and propagate in the radial direction. The crack closes as it progresses in the compressive core.

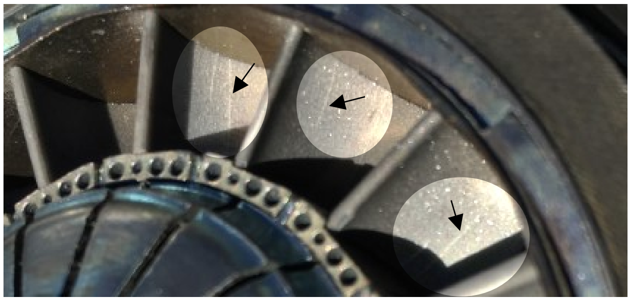

Figure 3.13 Flexible-hub prototype after 7 cumulated minutes of testing at TIT over 1000 °C and tip speed between 325 and 350 m/s, leading to cracked silicon nitride blades

B. Results with sliding blade

Several short test runs were performed at a TIT ranging from 800 °C to 950 °C at a tip speed of 300 m/s. Visual inspection of the prototype revealed no damage in this configuration. The temperature and speed were then increased progressively with multiple 5-minute tests to a TIT of 1100 °C and a tip speed of 350 m/s. Following this, a 1h continuous test was completed in these conditions, with a hydrogen/propane fuel mix for increased test duration. Figure 3.14 illustrates TIT and tip speed during the 1h continuous test.

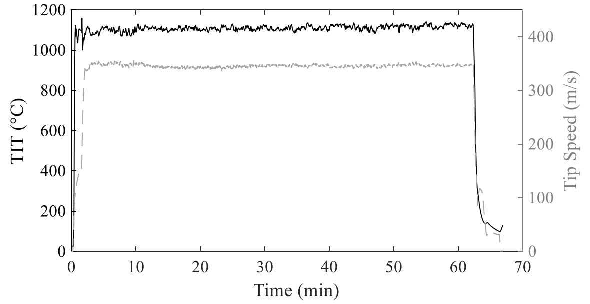

Figure 3.14 Hour-long test data for the sliding-blade prototype, at 1100 °C TIT and 350 m/s tip speed.

Ramp-up management proved a key parameter to test success, i.e. low-speed prototype warm-up at high temperature. This testing method was more heavily integrated in the sliding-angle prototype testing, as test experience indicated that it could provide a difference in blade stress. After the 1 h test, visual inspection revealed no damage to any component of the rotor. A close-up view of components after test is shown in Figure 3.15.

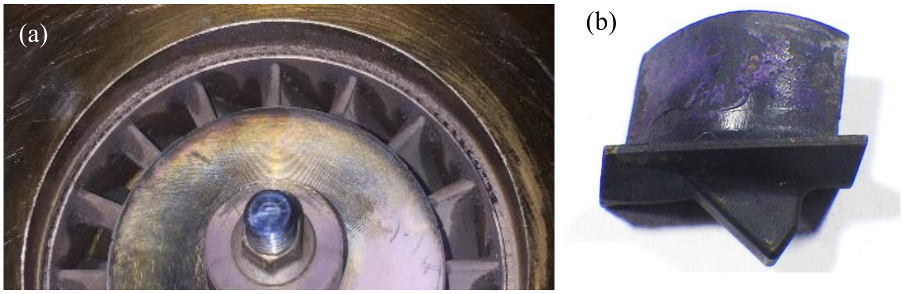

Figure 3.15 (a) Sliding-blade ICT prototype after testing over one hour at a TIT of 1100 °C and tip speed of 350 m/s, (b) no visible damage to the blade. Coloration is due to thermochromic paint applied to the prototype.

3.8 Discussion

Tests demonstrate that the inside-out configuration can support stiff, fragile ceramic blades at high temperatures and for hour-long test durations. Whereas previous full-ceramic inside-out design efforts failed at room temperature, both (A) the flexible-hub and (B) the sliding-blade ICT design support blades at temperatures up to 1000 °C and 1100 °C, respectively. It is surmised that this is due to the integration of metallic components in the rotor assembly, allowing for light compliance where needed to reduce tensile loads and thus not rely solely on heavy interference fitting as was the case in Ref. [62].

Failure mode for the flexible-hub prototype was graceful and was only noted upon inspection after the tests. The use of a flexible metallic hub increases the robustness of the rotor as it adjusts to the blade cracked state. However, important design changes would have to be made to the flexible hub to increase reliability and achievable rotational speed. The sliding-blade ICT design reached the milestone of hour-long testing. By removing the high-pressure, high-temperature blade/hub frictional interface in the flexible-hub design, local blade tensile stress is eliminated at the blade base.

Although the sliding-blade design removes the problematic interface at the blade base, ceramic/metal interface remains the main challenge that must be addressed in future ICT iterations at the blade tip. The inside-out configuration depends on a high-pressure interface at the blade tip, which creates a problem due to friction at this interface. Further work should concentrate on achieving a better CTE compatibility, as well as reducing friction coefficient at the interface. For multiple-turbine-engine small aircraft, the hazardous failure rate should be below 10^{-7}/h [15]. With no modification of the sliding-blade design, a reduction of friction coefficient from $\mu = 0.3$ to $\mu = 0.1$ at the blade tip would lead to single-blade probability of failure at 1000 h falling from 8.2×10^{-8}/h to 6.0×10^{-11}/h, an increase in reliability of 3 orders of magnitude, meeting FAA reliability requirements and paving the way to higher TIT and tip speed. Furthermore, a CTE-related problem was noted in ceramic dovetailed blades development literature, as the slots would pinch and lock up upon transient operation [69,70]. Boron nitride was added to the interface, cancelling lockup and increasing thermal cycling capability in a static tensile blade testing rig, from 2 cycles before failure to 120 successful cycles totaling 5000 test hours. Although the load case was not identical, these lubrication results remain encouraging for future development of the blade interface in ICT rotors.

3.9 Conclusions and Perspectives

Although significant efforts and financing have been poured into the development of monolithic ceramics for turbine rotors, none of the classic configurations have achieved the viability thresholds required to truly be competitive. Past trials have shown that FOD/DOD sensitivity and local stress rises in ceramic blisks and dovetail ceramic blades are roadblocks to the integration of ceramics to turbine rotors. The Inside-Out Ceramic Turbine (ICT) addresses these problems by using centrifugal loading in the rotor to compress individual monolithic ceramic blades against a high-specific-strength, structural rotating shroud. In theory, this has the effect of using ceramic strengths instead of suffering its weaknesses, i.e. using it in compression rather than tension. This reduces all principal stresses, thus probability of failure, in the blades, for a given rotational speed.

Experimental testing was undertaken to identify real-life ICT pressure points in two concurrent designs, (A) using a flexible hub to clamp the blades and (B) using sliding-planes to allow free displacement of the blades. The flexible-hub prototype withstood temperatures up to 800 °C and DOD events without cracking, but blades showed evidence of cracking at 1000 °C during 5-minute testing, although no catastrophic failure occurred. The sliding-blade prototype withstood a TIT of 1100 °C (2012 °F), at tip speeds over 350 m/s for over 1 hour, a significant milestone on the way to the targeted temperature of 1275 °C and tip speed of 425 m/s. The structural composite shroud showed no degradation throughout testing. More investigation into the structural shroud is ongoing to increase tip speed, with the use of more lightweight alloys.

Blade stress is surmised to be caused by thermal and centrifugal expansion mismatch between the ceramic blade and the metallic supporting elements. Stressed regions are limited to the interface, whereas the blade core is in a compressive state. The sliding-blade design is superior to the flexible-hub design, as it eliminates a highly stressed interface at the base of the blade. Better matching CTEs, as well as reducing friction coefficient at the ceramic/metal interface, e.g. with lubricant coatings successfully tested in the literature to treat thermal lockup for a ceramic turbine rotor blade, should lead to high reliability ceramic blades in the ICT configuration.

3.10 Funding Sources

This work was funded by Exonetik Turbo and the Natural Science and Engineering Research Council of Canada (NSERC) through CRD PJ 477320-14, as well as Defense Research and Development Canada (DRDC) contract W7714-196710/001/SV. Scholarships were provided by NSERC and the Fonds de recherche du Québec – Nature et technologies (FRQNT).

3.11 Acknowledgements

The authors would like to express their regards for the technical support provided by the research professionals, engineers and professors of Université de Sherbrooke and Exonetik Turbo, involved in the development of ICT rotors, as well as LAMSI at École de technologie supérieure for their support in additive manufacturing.

CHAPTER 4

BLADE TIP INTERFACE DESIGN EXPLORATION

4.1 Introduction

As inferred in Chapter 3, frictional stresses, which are due to the greater deformation of the shroud relatively to the blade tip, are the main driver of high probability of failure in the ICT rotor in its current configuration. Figure 4.1 shows the principal stress vectors in the blade under normal operation. When observing σ_1 and σ_2, two physical phenomena appear to occur simultaneously at the blade tip interface: σ_1 is in the tangential θ direction, aligned with the shroud's hoop strain, and σ_2 is in the axial z direction, aligned with axial component of the shroud's thermal expansion. Finally, σ_3 is in the radial r direction, demonstrating the overall compressive stress field on the airfoil. The vectors are scaled according to stress magnitude, indicating that the primary loading is indeed compressive and radial, and that the tensile stresses are due to secondary effects at the blade tip.

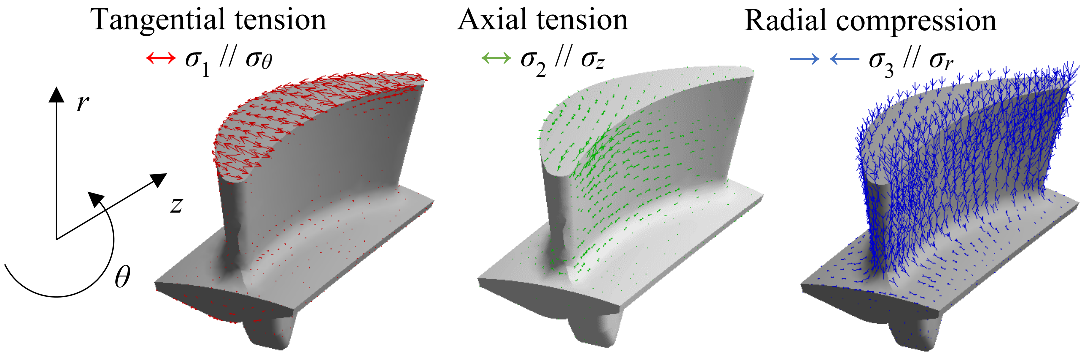

Figure 4.1 Orthogonal nature of principal stress vectors ($\sigma_{1,2,3}$) in the ICT blade, just about aligned with the rotor's cylindrical coordinate system r-θ-z

These directional stresses are caused by the mechanical loadings specific to the inside-out rotor configuration. The analysis in this chapter aims at relating the tensile stresses to design variables, so that they can be reduced in future rotor designs. To generalize the problem as much as possible and faithfully model non-linear behaviour, a simplified geometry, parameterized finite element model is used to test thousands of combinations of the main driving variables and relate them to probability of failure in the rotor blades. This is done with a design of experiments (DOE), whose results pass through a neural network to establish correlation. According to the findings in this chapter, the dominant design variables were found to be the coefficient of friction, but also thermal expansion mismatch and rotational velocity, to a lesser extent. These should all be reduced as much as possible to decrease probability of failure in the ceramic blades.

4.2 Methodology

As mentioned above, a numerical approach is taken to model the frictional interface through finite element analysis (FEA). The interface geometry is first simplified, then a DOE is devised to simulate the interface several thousands of times, varying a selection of design variables. The simulation flowchart is shown in Figure 4.2, where ***X*** is the input variables vector, and ***Y*** is the output vector, which is fed into the neural network.

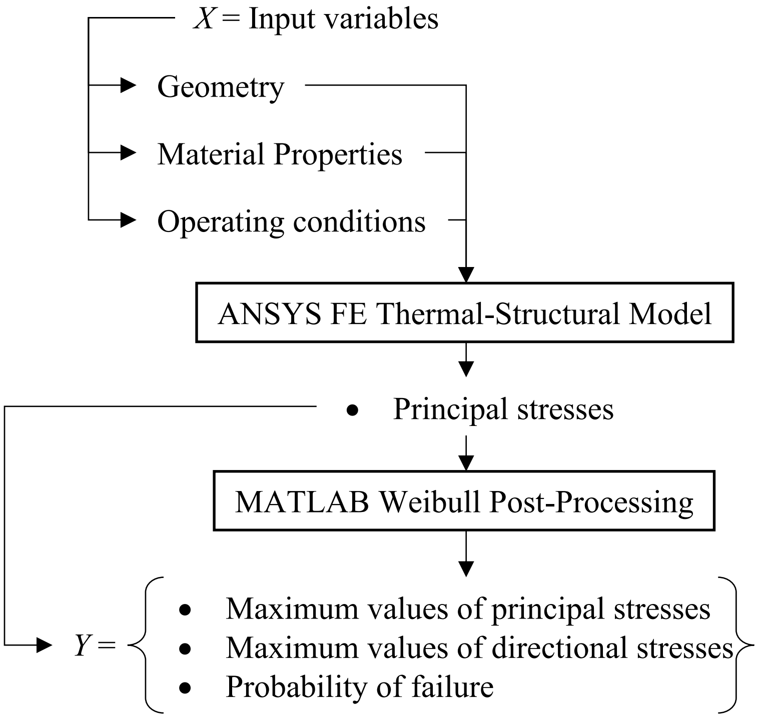

Figure 4.2 Numerical analysis flowchart

The main equations which are thought to affect blade tip interface are drawn up, to determine the variables of interest playing a role at the interface. As it is a frictional interface, the friction coefficient, normal force, and forced displacement at the interface – caused by hoop strain and thermal expansion – are of interest. Following that, a simplified, parameterized turbine rotor computer-aided design (CAD) is created in SolidWorks® as a basis for a DOE, which is created and run through FE software Ansys Workbench®. Blade probability of failure is calculated in MATLAB® and a hyperbolic tangent-based neural network is created in SAS JMP®, a data visualization software, to compare the effects of the different DOE inputs. A neural network is chosen over a Gaussian process for its good predictive ability and capacity to rapidly fit a great number of data points with what is expected to be significant non-linearities.

4.2.1 DOE Variable Selection

Before starting the numerical analysis, the underlying physics which are thought to affect tension in the rotor blade tips are drawn up as equations, from which the DOE variables are chosen. These equations are simplified to capture de underlying phenomena; however, the actual physics are fully simulated through FE modeling. Should the variable selection be insufficient to define the problem, the neural network fit will be poor in the end. On the other hand, should there be redundant variables, they will have little effect on the fit. Although transient phenomena should be explored, steady-state operation is used here to simplify the model and reduce the number of critical physical quantities in play.

The problem is thought to be due to (1) friction between the blade tip and the structural shroud. As shown in Figure 4.1, tensile stress is dominant in the axial and tangential directions. The following phenomena can explain this: (2) large hoop strain of the shroud, due to extreme internal force and centrifugal body force applied to the shroud and (3) thermal expansion of the shroud which is expected to be greater than the ceramic blade tip's thermal expansion, due to a large difference in coefficient of thermal expansion. Both these phenomena yield a forced displacement in the shroud and blade tip, which results in two phenomena: sticking or slipping. This is shown in a simplified schematic in Figure 4.3, where the shroud is compounded into one equivalent layer and the ceramic is either sticking or slipping against it. For ceramic stuck to the shroud, stress is dictated by displacement δ and the stiffnesses E of the layers, bending notwithstanding. For ceramic slipping on the shroud, shear stress τ is dictated by the interface's capacity to convert centrifugal force F_g to an effective frictional force F_f acting upon a given surface A, across a hypothetical thickness t. The transition from one regime to another is non-linear and can occur within the surface, hence the numerical approach.

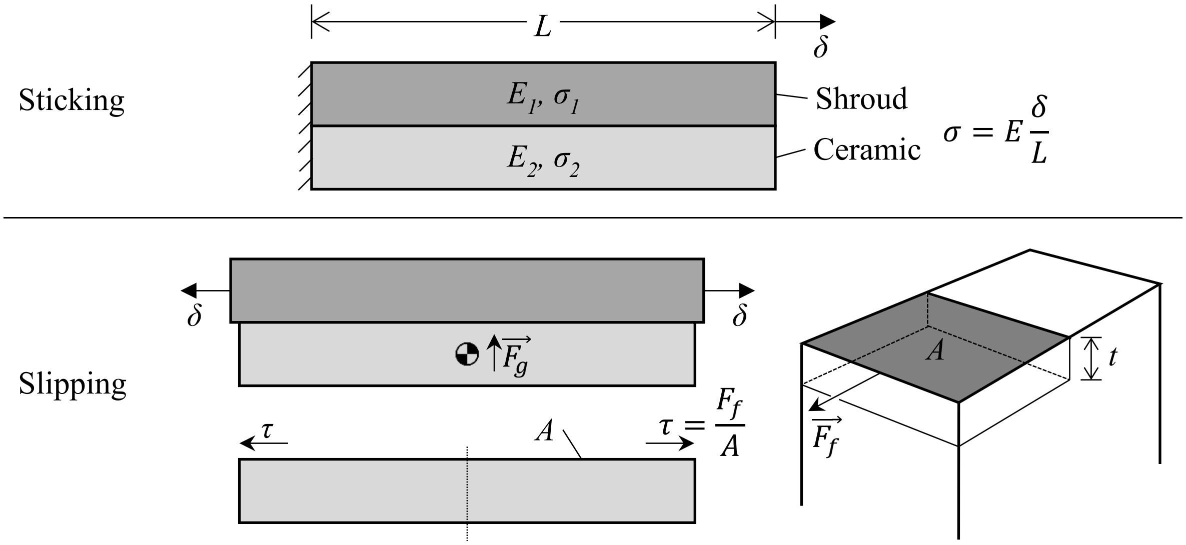

Figure 4.3 Conceptual schematic of the two phenomena occurring upon forced displacement at the interface between the blade and the shroud

From this simplified approach, stiffness and frictional interface characteristics seem to be involved, as well as forced displacement and centrifugal force. It is possible to relate this to centrifugal and thermal forces, by dissecting the resulting strain field in the θ-z plane on the shroud, shown in Figure 4.4. Local strain $d\vec{\varepsilon}$ is transferred, through friction, either sticking or slipping, as local shear strain vector $d\vec{\gamma}$ at the blade tip contact area dA.

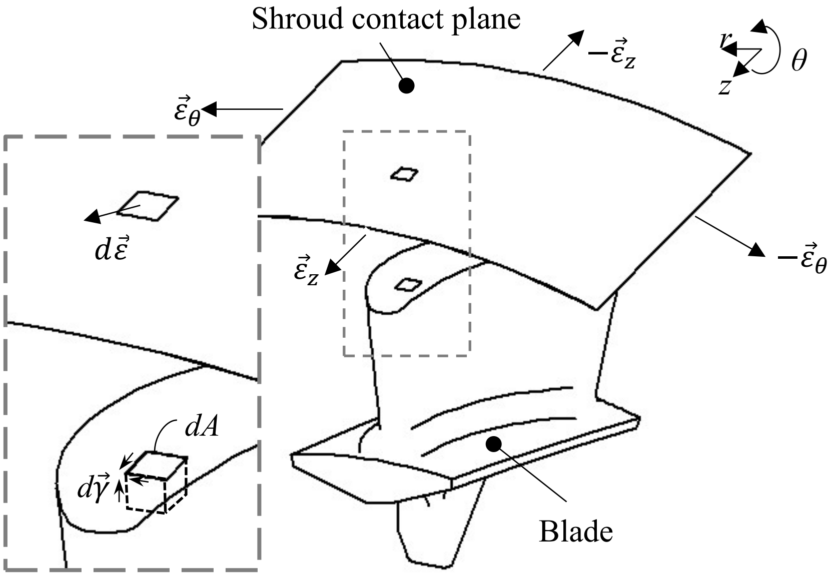

Figure 4.4 Illustration of the infinitesimal contact patch transferring shroud strain to shear in the blade tip

Figure 4.5 shows the full simplified CAD geometry used in the DOE, along with the DOE variables. Blade base and tip radii are kept constant, thus blade height does not vary. Tip radius is 60 mm, which corresponds roughly to a 200 kW net output ICT turbogenerator scale. Blade solidity is kept constant at 50%, meaning that the number of blades increases as blade thickness b_t decreases, and internal centrifugal load is only dependent on blade density ρ_b. A symmetry plane is introduced in the axial and tangential directions, to save on calculation time. The variables selected in the DOE are identified as **bold** in Eqs (4.1)-(4.6).

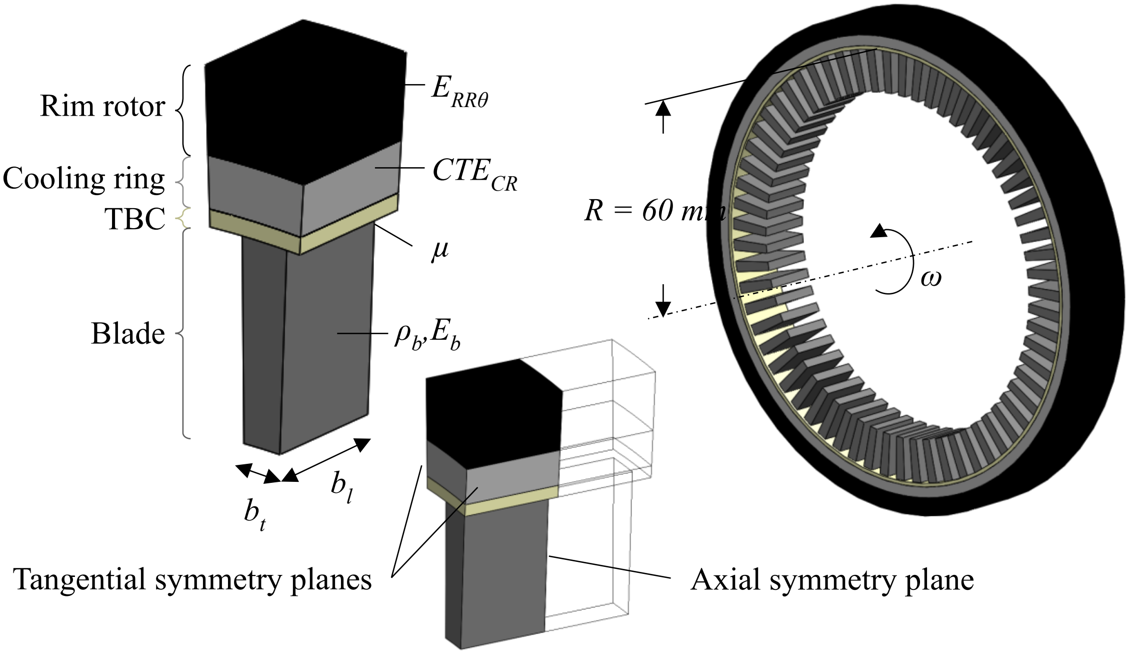

Figure 4.5 Simplified turbine geometry: single turbine segment for FEA (left), symmetry plane location (center), full rotor for illustrative purposes (right) and identified DOE variables.

The first suspected actor – shroud mechanical hoop strain ε_θ due to centrifugal loading – is related to the load it must contain at a given tip speed ωR, in Eq. (4.1) [71]. The shroud is a multi-material composite structure, with a metallic cooling system and a carbon fiber containment hoop. Weight can be represented by an equivalent density ρ_{eq} – comprised of the supported blades, the metallic cooling system and the carbon-polymer hoop – and stiffness can be represented by an equivalent Young's modulus E_{eq} of the shroud only, as the blade does not contribute to tangential stiffness. Mechanical hoop strain is varied in the DOE by varying blade rotational velocity ω, density ρ_b and carbon rim tangential Young's modulus $E_{RR\theta}$.

Overall hoop strain:

$$\varepsilon_\theta \propto \frac{\rho_{eq}(\boldsymbol{\omega} R)^2}{E_{eq}} \tag{4.1}$$

where

$$\begin{aligned} \rho_{eq} &= f(\boldsymbol{\rho_b}, \rho_{CR}, \rho_{RR}) \\ E_{eq} &= f(E_{CR}, \boldsymbol{E_{RR\theta}}) \end{aligned} \tag{4.2}$$

The second actor, which acts in all directions, is thermal expansion. A positive mismatch in thermal expansion, i.e., a larger thermal expansion in the shroud than in the blade, will cause tensile loading in the blade tip. This is caused by a combination of different temperature increases ΔT and different coefficients of thermal expansion *CTE* in the blade and the metallic cooling system upon which the blade tip rests. The mismatch $\Delta\varepsilon_{th}$ is represented by Eq. (4.3). Because all effects are linear, only the cooling ring's CTE, CTE_{CR}, is varied in the DOE. Table 4.1 lists two combinations of candidate materials and ΔT to convey an appreciation of what $\Delta\varepsilon_{th}$ represents in design terms. A thermal barrier is expected to provide the temperature difference between the blade tip and the cooling ring inner diameter (ID).

Thermal strain mismatch:

$$\Delta\varepsilon_{th} = (\boldsymbol{CTE} * \Delta T)_{CR} - (CTE * \Delta T)_b \tag{4.3}$$

Table 4.1 Material combinations and associated thermal expansion mismatch $\Delta\varepsilon_{th}$

Cooling ring ID	**Cooling ring CTE[a] [72]**	**Blade tip[b]**	**$\Delta\varepsilon_{th}$ (%)**
Inconel 718, 600 °C	14.9 µ/m°C	Si_3N_4, 1000 °C	0.67
Titanium 6-2-4-2, 450 °C	9.47 µ/m°C	Si_3N_4, 1000 °C	0.063

[a] CTE is taken at given temperature

[b] Si3N4 CTE @ 1000°C = 3.5 µm/m°C **[73]**

Actual frictional shear stress $\vec{\tau}$ is caused by frictional force F_f due to the relative strain difference between the shroud and blade tip. Eq. (4.4) is the well-known Coulomb equation of friction and highlights the central importance of the coefficient of friction μ, and that a maximum frictional force value exists, beyond which slipping occurs. Normal force F_b applied by the blade body at its tip is due to the centrifugal pseudo-force, applied to the blade mass, caused by the centripetal acceleration field in the rotor. Although the actual force is a result of integration along the blade height, it is a safe approximation to use a constant centripetal acceleration taken at the blade tip radius R, as in Eq. (4.5). Blade mass is varied in the DOE by varying density ρ_b, affected by material selection. Rotational velocity ω is also varied.

Maximum frictional force: $$F_f \leq \boldsymbol{\mu} F_b \tag{4.4}$$

Normal contact force: $$F_b \cong \boldsymbol{\rho_b} V_b \boldsymbol{\omega}^2 R \tag{4.5}$$

The maximum local frictional shear stress is assumed to be the maximum load which can induce tensile loading in the *θ-z* plane at the blade tip, as further shear will cause the interface to slip. Shear stress is parallel to the total strain in the shroud at the contact point. The shear strain is related to the local frictional force F_f and the blade's shear modulus G_b. Frictional strain is varied in the DOE by using blade Young's modulus E_b, and coefficient of friction μ.

$$\vec{\gamma} \parallel \vec{\varepsilon}\,; \tau = \frac{F_f}{A}$$

$$G_b \overset{\text{def}}{=} \frac{\tau}{\gamma} = \frac{E_b}{2(1+\nu)}$$

Maximum frictional shear strain: $$d\vec{\gamma} \propto \frac{d\vec{F}_f}{\boldsymbol{E_b} dA} \tag{4.6}$$

Blade aspect ratio is varied to assess its effect on stress at the blade tip. Airfoil geometries vary significantly from one turbine design to another, depending on stage loading, degree of reaction (DOR), twist, etc. This is circumvented with an extremely simplified prismatic, block-shaped "blade", as shown in Figure 4.6. For readability's sake, these blocks are called blades throughout this chapter. Thus, blade volume DOE variable V_b is simply (length × thickness × height) and total contact area A is (length × thickness).

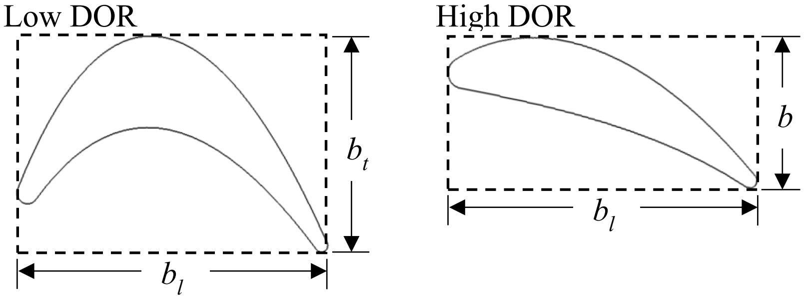

Figure 4.6 Examples of bounding boxes (dashed line) described by simplified dimensions of blade length b_l and blade thickness b_t

Finally, the selected DOE input variables and variation range are in Table 4.2. Variable range is selected to represent reasonably expected values. Thermal expansion mismatch $\Delta\varepsilon_{th}$ between the cooling ring and blade can vary significantly, according to cooling conditions and material selection and thermal barrier coating (TBC) thickness, and this is lumped into the wide-ranging CTE_{CR} variable. Rim rotor modulus $E_{RR\theta}$ depends on available fiber modulus. Orthotropic carbon fiber properties have been compiled by the ICT development team over time, and representative values were used here; fiber modulus is the main variable that can be chosen by the designer. Blade modulus E_b and density ρ_b depend on selected blade material: Zirconia, alumina, silicon carbide and silicon nitride are covered by these ranges. Blade length b_l is taken to be 90% of a rim rotor which could vary from 14-40 mm in length, according to engine power output and turbine stage. Blade thickness b_t is varied by applying a thickness-to-length ratio t/l, over a range that was deemed sufficient to cover slim to thick aspect ratio blades. Rotational velocity depends on overall turbine stage design. For the current tip radius, this range is equivalent to a blade tip speed of 282-471 m/s.

Table 4.2 DOE inputs and range

Input variable	Description	Range
CTE_{CR}	Cooling ring CTE	4-20 µm/m°C
$E_{RR\theta}$	Rim rotor tangential Young's modulus	120-210 GPa
E_b	Blade isotropic Young's modulus	200-400 GPa
ρ_b	Blade density	2.5-6 g/cc
b_l	Blade length	12.6-37.8 mm
t/l	Blade thickness-to-length ratio	0.1-0.4
ω	Rotational velocity	45-75 kRPM
μ	Coefficient of friction	0.05-0.55

The FE model is comprised of 3 steps, shown in the schematic in Figure 4.7. First, a thermal gradient is applied, based on thermal results from analyses such as that shown in Section 3.6. Second, centrifugal loading is applied to as coarsely meshed model to extract radial displacement. Third, the radial displacement is converted to a forced displacement in a finely meshed model. Stress results are extracted from the third and final step. The third step is added to ensure that the contact area remains flat – it is not allowed to bend around the tangential θ axis under centrifugal load.

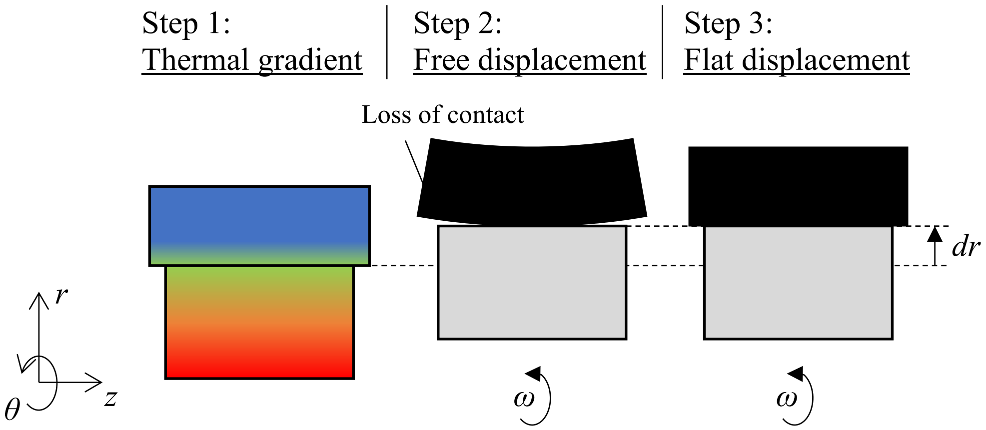

Figure 4.7 Schematic of FE model steps: to ensure a predictable contact patch shape between the simplified blade and shroud during centrifugal loading, an equivalent forced radial displacement *dr* is applied to the shroud inner skin

This numerical artefact simulates a semi-infinite body and enables the entire simplified prismatic blade tip to be in contact with the shroud, and therefore the contact shape is known. Analysis of results after Figure 4.7's Step 2 would add contact patch size and shape variables, which is deemed to be out of the scope of this analysis, as it is too dependent on airfoil shape, blade center of mass location and blade tip pressure distribution. Further details about the model and this particular assumption are given in Appendix A.

4.2.2 ANSYS FEM DOE

The variables in Table 4.2 are used with the Design Exploration module in Ansys Workbench. Geometry is varied through the SolidWorks associative interface, using the CAD model already shown in Figure 4.5. Figure 4.8 shows a few geometries generated by the Design Exploration tool. The geometry is adjusted to ensure the total number of model segments is an integer for all blade dimensions, to achieve correct tangential symmetry conditions. Coefficient of friction μ is set as a boundary condition, and rotational velocity ω is set as an inertial load in the structural analysis. Details of the analysis setup and workflow are in Appendix A.

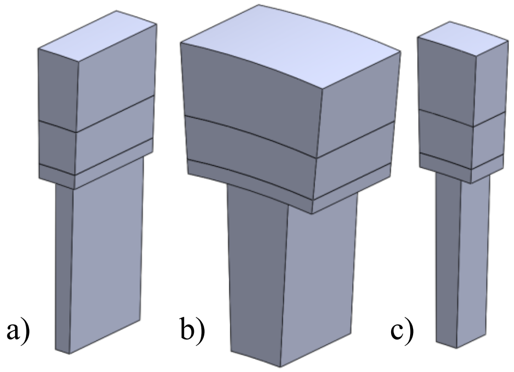

Figure 4.8 Sample of geometries generated using the DesignModeler/Solidworks associative interface: a) and b) have the same length, b) and c) have the same *t*/*l* ratio.

The material properties listed in Table 4.2 are set as variables in ANSYS Workbench Parameters. Other material properties are kept constant and are listed in Table 4.3. Ceramic constant properties are based on Kyocera silicon nitride. The cooling ring is based on Inconel 718. TBC properties are based on literature and an estimation based on the tests presented in Chapter 5.

Table 4.3 Constant material properties used in this analysis.

Material	Constant values in FEA		Material assignment
Ceramic [73]	Poisson's ratio	0.28	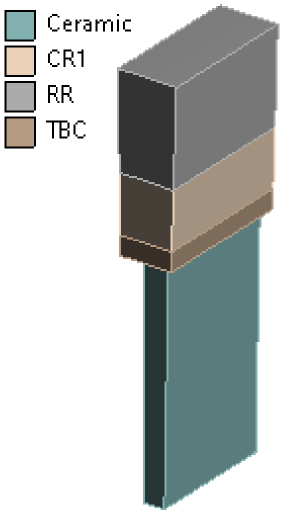
	Thermal conductivity	30 W/m°C	
	CTE	2.6 μm/m°C	
Cooling ring (*CR1*) [72]	Density	8193 kg/m³	
	Isotropic *E*	150 GPa	
	Poisson's ratio	0.3	
	Thermal conductivity	11.1 W/m°C	
Rim rotor (*RR*)	Density	1800 kg/m³	
	Radial, axial *E*	9.4 GPa	
	Shear modulus	5.5 GPa	
	Thermal conductivity	0.635 W/m°C	
TBC [74]	Density	5147 kg/m³	
	Out-of-plane *E*	200 GPa	
	In-plane *E*	20 GPa	
	Poisson's ratio	0.04	
	Shear modulus	9 GPa	
	Thermal conductivity	1.5 W/m°C	

For 8 inputs, an ideal amount of design points would be around $3^8 = 6561$, based on the rule of thumb that three points per dimensional combination allow a reasonable assessment of sensitivity. However, to cut down on calculation time, simulations were stopped after a total of 4800 points over 5 DOEs, as it was determined that the main trends were apparent. Latin hypercube sampling was used to generate the DOEs. Probability of failure is evaluated using the same approach as in Chapter 3, i.e., using the principal stresses of the simplified blade to compute P_f. The output variables are listed in Table 4.4. All these outputs are probed at the blade tip, which is the area of interest and deemed to be the most highly stressed segment of the body, except for P_f which is computed for the whole body. P_{fFR} uses the number of blades calculated during the geometry generation to assess P_f of the full rotor. Figure 4.9 shows an example of the location of various outputs at the blade tip.

Table 4.4 DOE outputs

Output variable	Description
$\sigma_{1,max}$	Maximum value of maximum principal stress
$\sigma_{2,max}$	Maximum value of middle principal stress
τ_{max}	Maximum value of interface frictional stress
σ_z	Maximum value of axial normal stress
σ_θ	Maximum value of tangential normal stress
P_f	Probability of failure in fast fracture
P_{fFR}	Probability of failure in fast fracture, for the full rotor

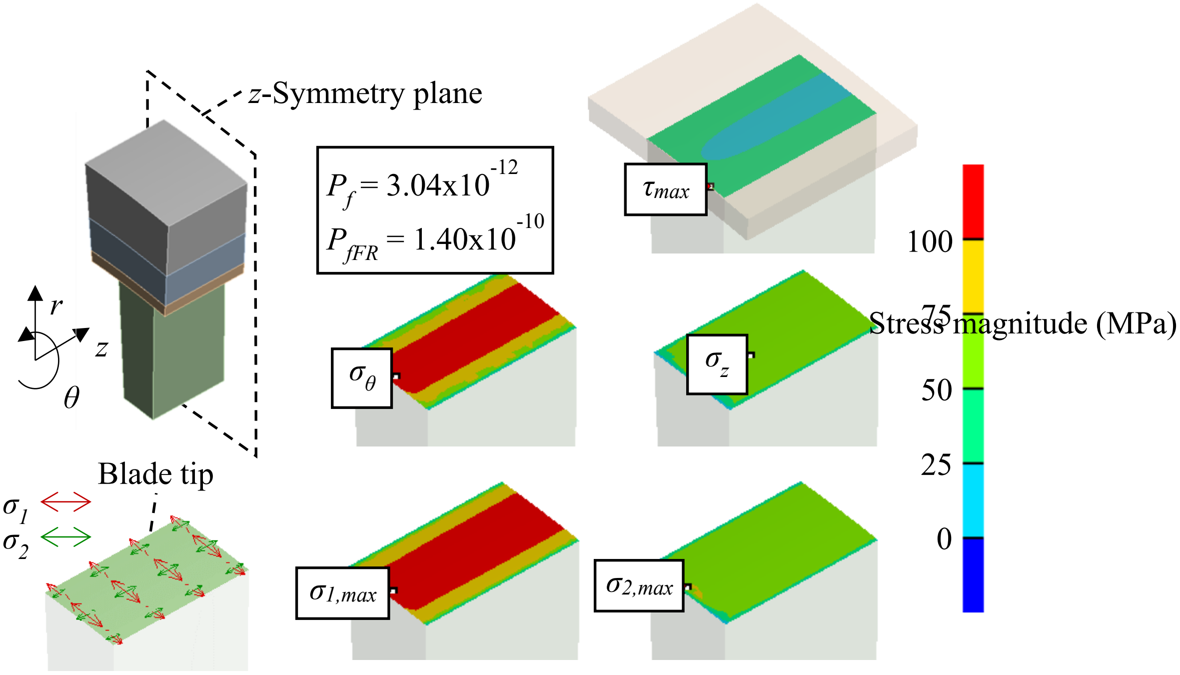

Figure 4.9 DOE outputs identified in Table 4.4, for calculation point #1062

4.2.3 MATLAB and JMP Post-treatment

ANSYS' capabilities are limited when it comes to data visualization and data post-processing. Thus, MATLAB and JMP were used to assess outputs. MATLAB is used to calculate probability of failure P_f in the blade, associate P_f to Ansys design point inputs, and generate the Excel input and output table used for JMP. JMP is used to assess sensitivity of the outputs to inputs with a metamodel generated with a neural network. Because of the simplifications listed above, a low fidelity metamodel ($R^2 > 0.9$) is sufficient and should correctly illustrate the sensitivity of the outputs to the selected inputs. Fast fracture P_f is calculated using the 2-parameter Weibull formula in Eq. (4.7).

$$P_f = 1 - e^{\frac{1}{\sigma_0}\int(\sum \sigma_i{}^m)dV} \tag{4.7}$$

Where σ_0 is the ceramic characteristic strength, m is its Weibull modulus, i is the principal stress component 1 to 3, as per principal of independent action (PIA), and V is the total blade volume. The profiler in JMP is used to correlate probability of failure to the inputs. Note that the $\log_{10}$ value of P_{fFR} is used, as JMP is unable to deal with numbers that are several tens of orders of magnitude apart. Seeing as variable t/l is linked to the number of blades, which influences full rotor probability of failure, P_{fFR} is used as the output variable of interest. A neural network, illustrated in Figure 4.10, is used to gain insight on the influence of the input variables. Validation of the fit is done with a random data holdback of 33 % – one third of data is not used for calculating fit, but rather to validate it. Four hidden nodes were found to give the best trends ($R^2 \approx 0.95$) without overfitting the data. This also validates that the selected input variables are sufficient to represent the desired output. Figure 4.11 shows the achieved fit, where the x-axis is the $\log_{10}(P_{fFR})$ predicted by the neural network fit, and the y-axis is the value calculated in MATLAB from FE results.

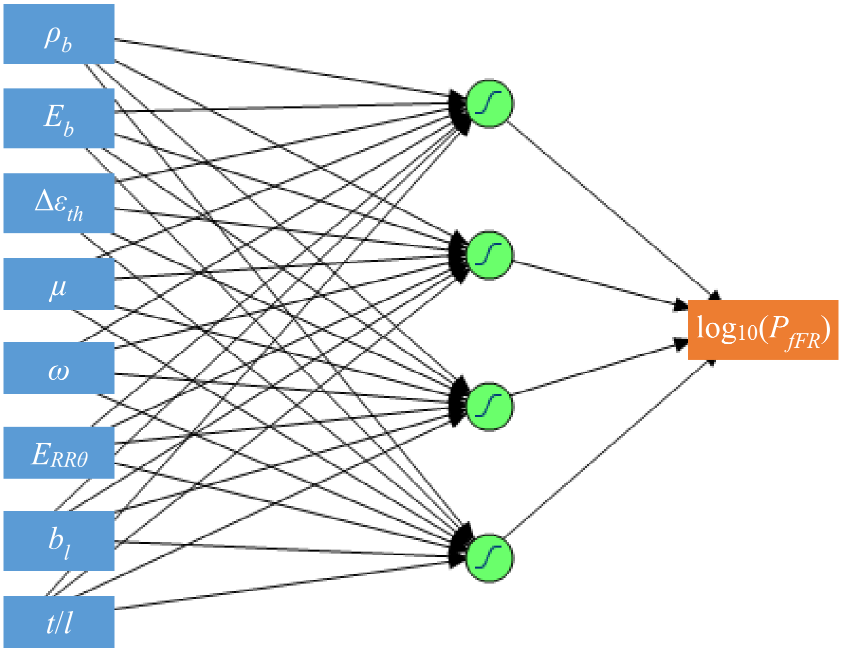

Figure 4.10 Neural network diagram, with 4 hyperbolic tangent nodes

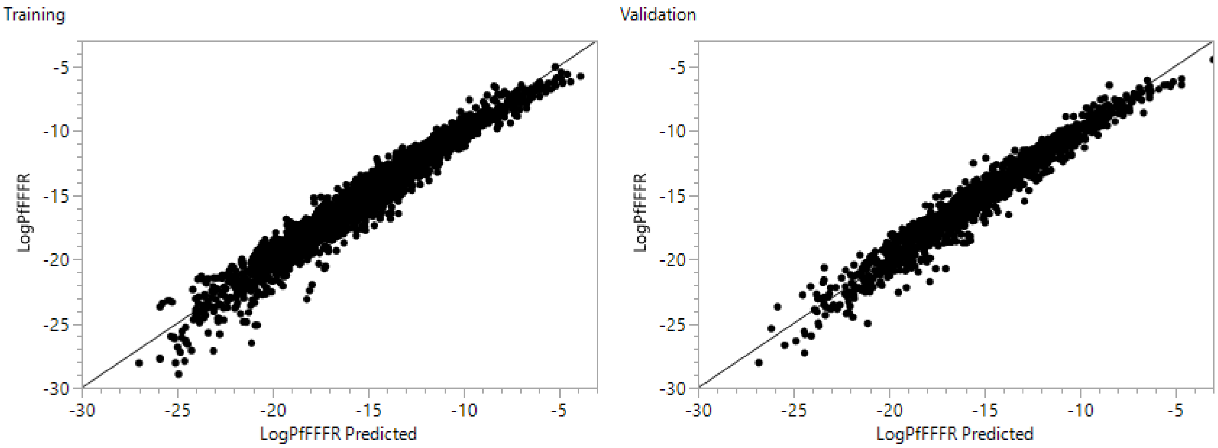

Figure 4.11 Actual vs predicted $\log_{10}(P_{fFR})$ values for the training (left) and validation (right) data

4.3 Results & Discussion

First, the relationships of design variables, directional stresses and P_f are established. Design variables are placed in descending order of influence over P_f, to give an intuition over which design aspect should be treated first. Following this, blade tip shape design guidelines are established which minimize P_f at given operating conditions.

4.3.1 P_f and directional stresses

Typically, P_f follows σ_1 quite closely, and it is the case in this DOE as shown in Figure 4.12 87 % of data points fall within the dense cluster of points along the log regression. This reveals that stress is localized in a single zone in most cases, which dominates the P_f output. The corollary of the tight correspondence of P_f to σ_1 is that a maximum value of local σ_1 can be used by the designer to estimate if the blade falls beneath a desired P_f value. For example, $P_f = 10^{-8}$ occurs at a maximum value of σ_1 = 206 MPa and $P_f = 10^{-10}$ at σ_1 = 153 MPa, for a single blade in fast fracture.

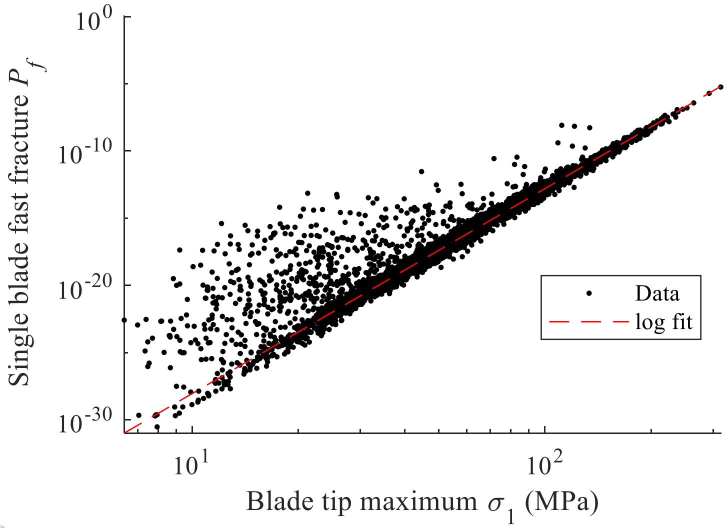

Figure 4.12 Probability of failure plotted against maximum value of σ_1 at the blade-to-shroud interface.

Figure 4.12 also shows an impressive spread in P_f, with roughly 25 orders of magnitude between the smallest and largest value. This indicates that conditions exist where a signification reduction of P_f is possible. The remaining 13 % presumably have multiple stressed zones, have a more important contribution of σ_2, or have larger stressed zones with more than one element dominating output. Figure 4.13 shows the influence of both σ_1 and σ_2 on P_f. P_f increases monotonically along the σ_1 axis, with hardly any effect from σ_2.

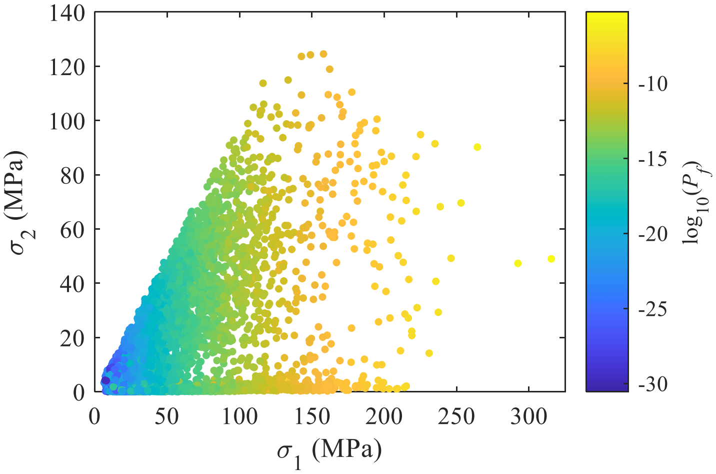

Figure 4.13 Distribution of maximum σ_1 and σ_2 values, coloured according to $\log_{10}(P_f)$

The stress at the interface is thought to be dominated by directional phenomena, i.e., friction in the tangential θ and axial z directions. The composition of the tensile principal stresses, σ_1 and σ_2, in terms of σ_θ and σ_z is plotted in Figure 4.14. All points fall into three planes, which are plotted in Figure 4.15 to help visualization.

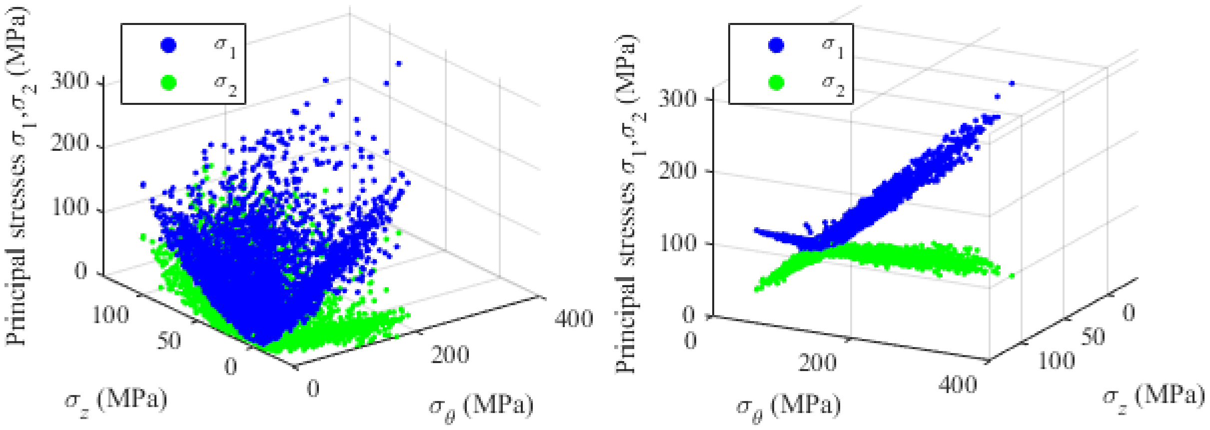

Figure 4.14 Composition of maximum and medium principal stresses σ_1 and σ_2 in terms of tangential and axial stresses σ_θ and σ_z: standard view (left) and view aligned with data planes (right)

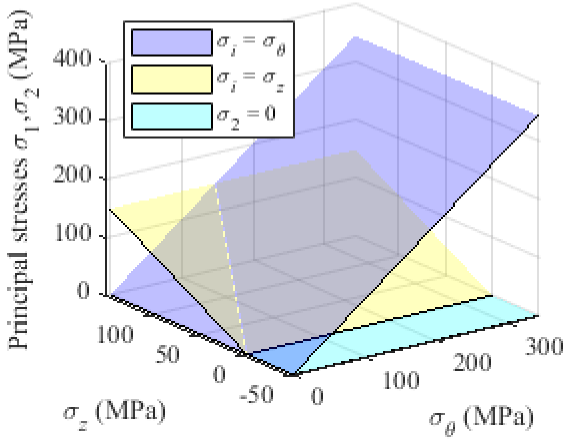

Figure 4.15 Result from Figure 4.14, grouped into simplified planes.

Figure 4.15 leads to 3 conclusions: (1) The principal axes are perfectly aligned with the cylindrical axes, which means that the loading directions should be predictable and that the equations in Section 4.2.1 should correctly capture them. (2) Most cases have a dominant tangential component ($\sigma_1 = \sigma_\theta$) but in some cases the axial stresses are larger. (3) When axial stresses are compressive ($\sigma_z < 0$), the medium principal stress falls to 0 ($\sigma_2 = 0$).

By using the Distribution tool in JMP, it is possible to check which combinations tend to land in the σ_θ or σ_z dominant regime. The dominant input variables which affect this are $\Delta\varepsilon_{th}$, ω and b_l. Figure 4.16 shows the total variable distribution in pale green and the distribution of the points where $\sigma_z > \sigma_\theta$ in dark green. From this information, high thermal expansion mismatch at low speed, for a short blade, leads to σ_1 to be oriented in the axial direction. All other scenarios will cause maximum σ_1 to be in the tangential direction.

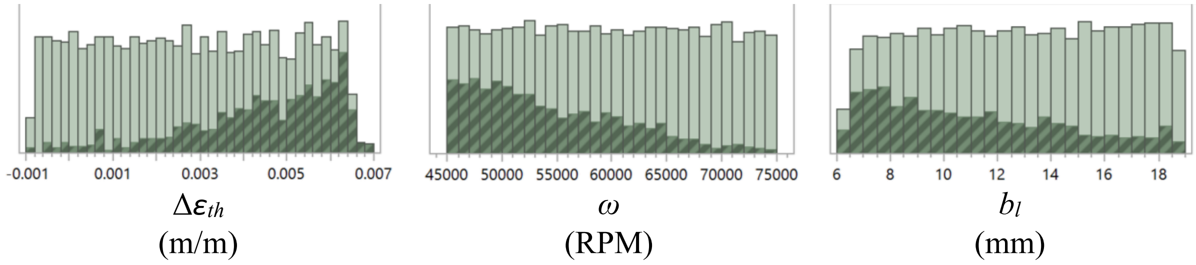

Figure 4.16 Distribution of variables which cause maximum values $\sigma_1 = \sigma_z$.

The compressive σ_z regime (cyan in Figure 4.15) is led by $\Delta\varepsilon_{th}$ and b_l, i.e. a negative or very low $\Delta\varepsilon_{th}$ (possible in this numerical analysis but improbable in true operating conditions) and a long blade, as indicated in Figure 4.17. Interestingly, a $\mu > 0.2$ seems to be required to achieve this regime consistently. This could indicate that $\mu = 0.2$ is a threshold for slip.

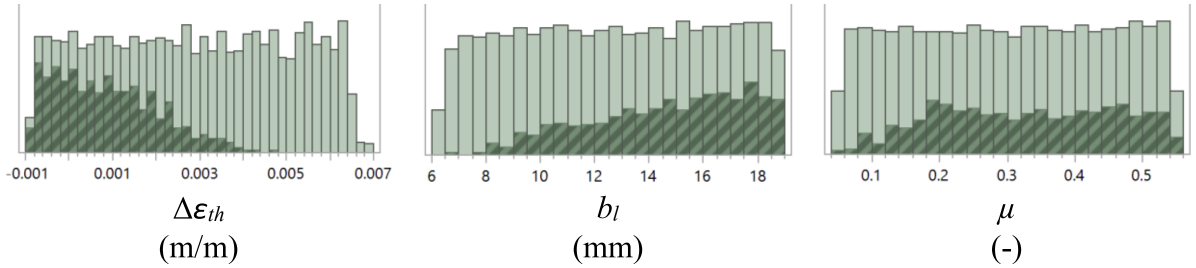

Figure 4.17 Simulation conditions which lead to compressive axial blade tip stresses ($\sigma_z < 0$)

P_f data points plotted against the different inputs, in Figure 4.18, gives a certain intuition of what the dominant factors are. The spread in P_f is enormous for all inputs, however the sensitivity is somewhat apparent.

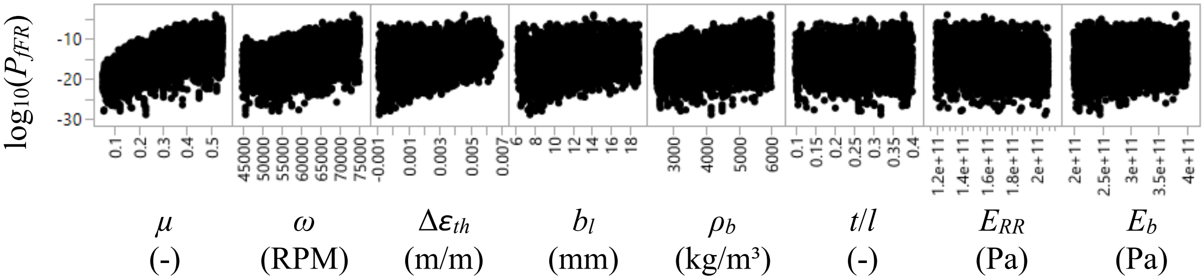

Figure 4.18 Log_{10} value of P_f data points according to input variables.

The sensitivity of P_{fFR} in the blade to the various inputs is represented by the contribution of each input in Table 4.5, assuming that all inputs are random, uniform, and independently varied, which is the case in this DOE. "Main Effect" considers each variable effect as totally independent and "Total Effect" includes combinations with other factors. A large difference between both values means that the factors show some level of dependence to each other, which the neural net can identify. In this case, combination is significant in most variables except for μ.

Table 4.5 Relative contribution of each input variable to P_{fFR}

Variable	Main Effect	Total Effect	Difference
μ	0.372	**0.418**	+12 %
ω	0.182	0.246	+35 %
$\Delta\varepsilon_{th}$	0.149	0.213	+43 %
b_l	0.048	0.098	+104 %
ρ_b	0.07	0.096	+37 %
t/l	0.017	0.049	+188 %
E_{RR}	0.008	0.014	+75 %
E_b	0.006	0.011	+83 %

The neural network profiler is shown in Figure 4.19. The local sensitivity is indicated with the purple triangle and the profiler is coloured according to total effect indicated in Table 4.5. Considering the important combinatory effects of most variables, the profiler can change significantly as values are changed, and thus it is recommended to view the html dynamic profiler, although the screenshot in Figure 4.19 gives a decent idea of the sensitivity to each variable.

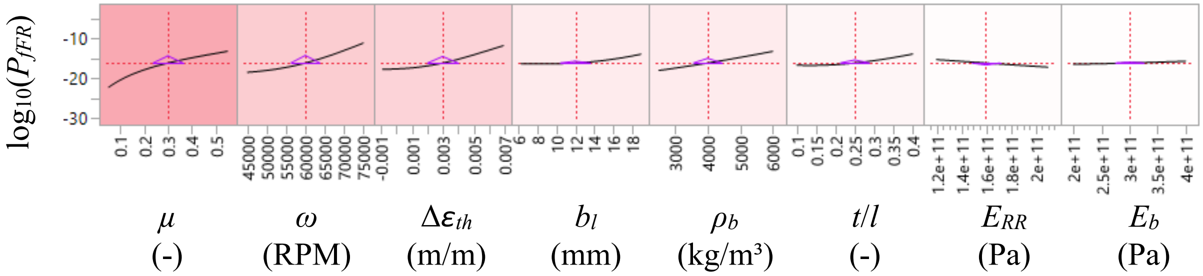

Figure 4.19 Neural network prediction profiler ordered and coloured by contribution importance

Table 4.5 shows that P_{fFR} is most sensitive to μ, by far. This makes sense, as μ is directly involved in any form of frictional stress, both centrifugal- and CTE-dependent. Rotational speed ω and thermal expansion mismatch $\Delta\varepsilon_{th}$ have a similar influence, indicating that both must be seen to in the design phase. Blade length b_l and blade density ρ_b also have similar overall influence. μ, ω, ρ_b, have a significant monotonic effect on P_{fFR}, meaning that reducing any of them has a positive effect on P_{fFR}. E_{RR} and E_b have little effect. t/l is treated in the geometric variables analysis in Section 4.3.2.

Finally, by including slow crack growth (SCG, see Section 3.6) in the calculation of P_{fFR} for 1000 h operation, it is possible to view the sensitivity of rotor design parameters ε_{th} and ω

(expressed in rotor tip speed, $v = \omega R$) to μ in Figure 4.20. This is calculated for Si3N4 material properties, $E_{RR\theta}$ is 160 GPa, blade length is 15 mm and t/l is 0.3. Isolines represent a $P_{fFR,1000h}$ of 10^{-7} for a given value of μ. A value of 10^{-7} was selected as it gives a 10^{-10}/flight hour failure rate, which provides a very safe margin for other components to fail in the engine and still be within FAA recommendations in Table 1.1. Blade failure will require further exploration in further research, as past experiments have shown that the rotor can indeed operate with a "failed" blade, as typically the crack will propagate and a small fragment will chip off, without causing any catastrophic failure. Therefore, Figure 4.20 is shown here as an indication only and the margin of safety will be adjusted in the future.

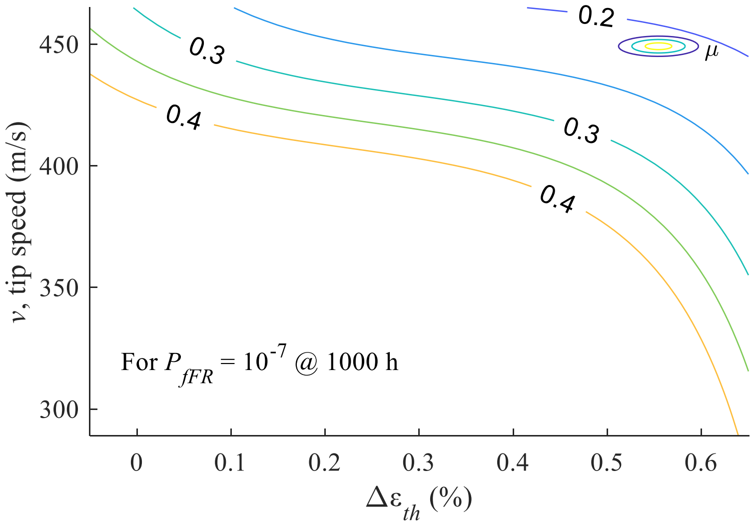

Figure 4.20 Coefficient of friction μ isolines for achieving $P_f = 10^{-10}$ after 1000 h, according to the difference in thermal strain between the shroud and blade, and blade tip speed

4.3.2 Blade geometry guidelines

Geometric variables b_l and t/l show possible optimum values in Figure 4.19, which change according to operating conditions and aero design. This is explored using Matlab's *fmincon* function applied to the neural net hidden nodes' equations. The exploration seeks to find the t/l ratio which minimizes P_{fFR} for a given blade length b_l and thermal expansion mismatch $\Delta\varepsilon_{th}$. These independent variables were chosen as it is estimated that rotor length will be dependent on packaging, stage number and stage power output, and that thermal expansion mismatch will be dictated by material selection, TBC thickness and cooling supply. Friction factor μ and rotational velocity ω are varied separately. Figure 4.21 shows the influence of μ for a

$\omega = 60$ kRPM (375 m/s tip speed), and Figure 4.22 shows the influence of ω for $\mu = 0.2$ (reasonable if hBN is applied at the interface). Other variables are fixed at realistic values of $\rho_b = 3200$ kg/m³, $E_{RR} = 160$ GPa and $E_b = 300$ GPa.

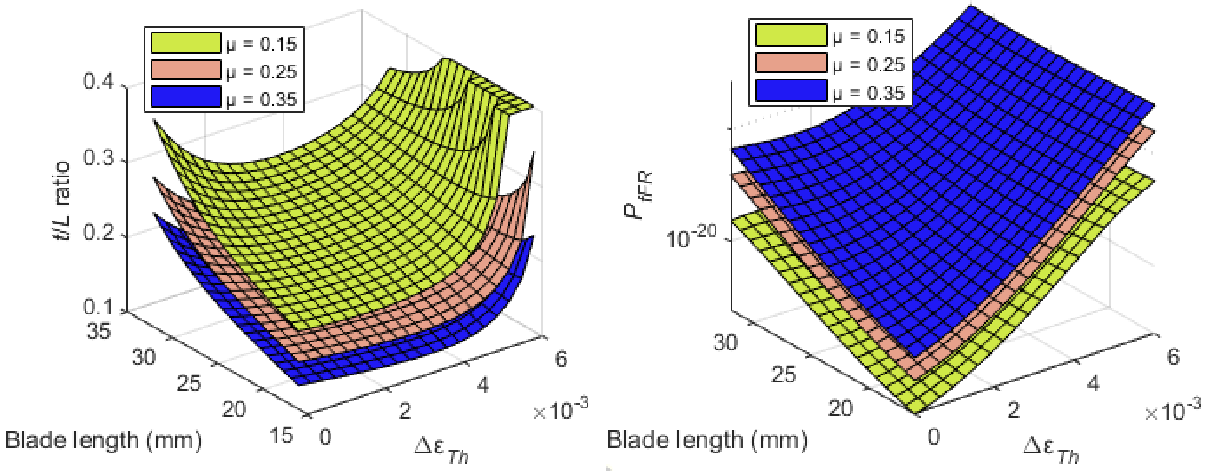

Figure 4.21 Optimal t/l ratio (left) for minimizing P_{fFR} (right) for given μ, b_l and $\Delta\varepsilon_{th}$, for $\omega = 60\,000$ RPM.

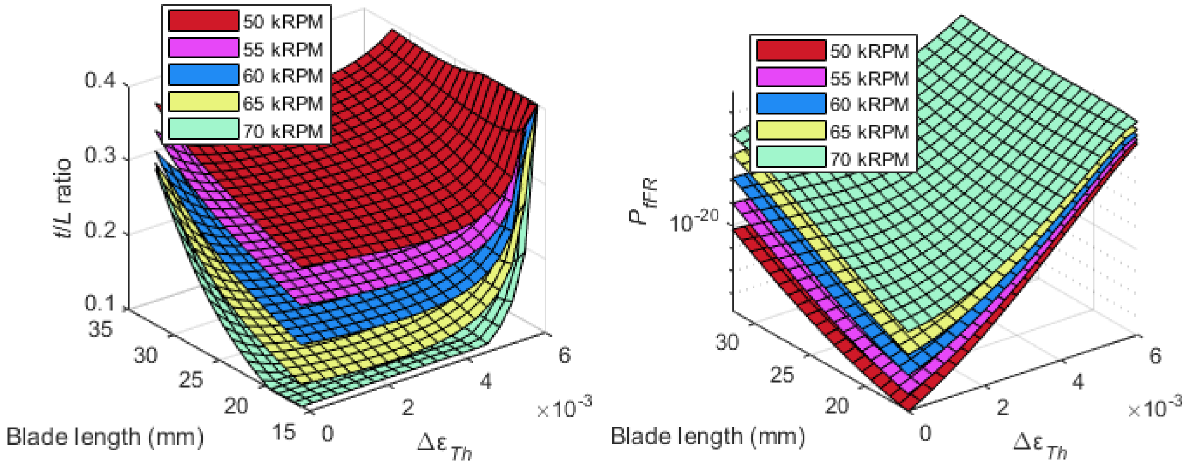

Figure 4.22 Optimal t/l ratio (left) for minimizing P_{fFR} (right) for given ω, b_l and $\Delta\varepsilon_{th}$, for $\mu = 0.2$.

The optimal t/l ratios shown in Figure 4.21 and Figure 4.22 are not intuitive. They originate from the non-linear behaviour of friction (stick vs slip) which will apply differently according to blade tip size and aspect ratio. However, purely in the intent of minimizing P_f, the shorter the blade and the smaller the thermal expansion mismatch, the better.

4.4 Conclusions

The analysis in this chapter aimed at determining which design variables had the most significant impact on blade failure potential introduced in Chapter 3, to guide the design requirements for the solution-searching phase in Chapter 5. Through an FE modeling approach, with appropriate simplifications, design variables were identified and hierarchized according to importance in the blade tip stress state and, therefore, failure probability P_f.

A DOE was set up and results were analyzed with a neural network. The main conclusions are illustrated in Figure 4.23. It was determined that friction coefficient μ is the single most important variable to affect P_f. Most operating conditions cause a tangential tensile stress state in the blade tip, indicating that hoop strain is the dominant stress-inducing phenomenon in the ICT blade in most design combinations. This indicates a lighter shroud should reduce hoop strain and thus tangential loading. Thermal expansion mismatch – the difference between the thermal expansion of the shroud and the blade – also has a significant effect and should be reduced to as close to 0 as possible. This can be achieved by keeping the cooling ring cold and the blade hot, such as through the use of a thermal barrier, as well as by selecting materials with close CTEs. Low rotational velocity and lighter blades are better for lower stresses, as this reduces normal load at the interface. This can prove difficult, as ceramics are already among the lightest engineering materials available and rotational velocity is linked to many other turbine design considerations. Optimum blade tip thickness/length ratio is not straightforward and is highly dependent on turbine operating conditions. Guidelines for operating conditions and blade geometry are shown in Figures 4.20, 4.21 and 4.22, and should be taken into consideration when designing the rotor. Rim rotor and blade Young's moduli have little to no impact on blade P_f.

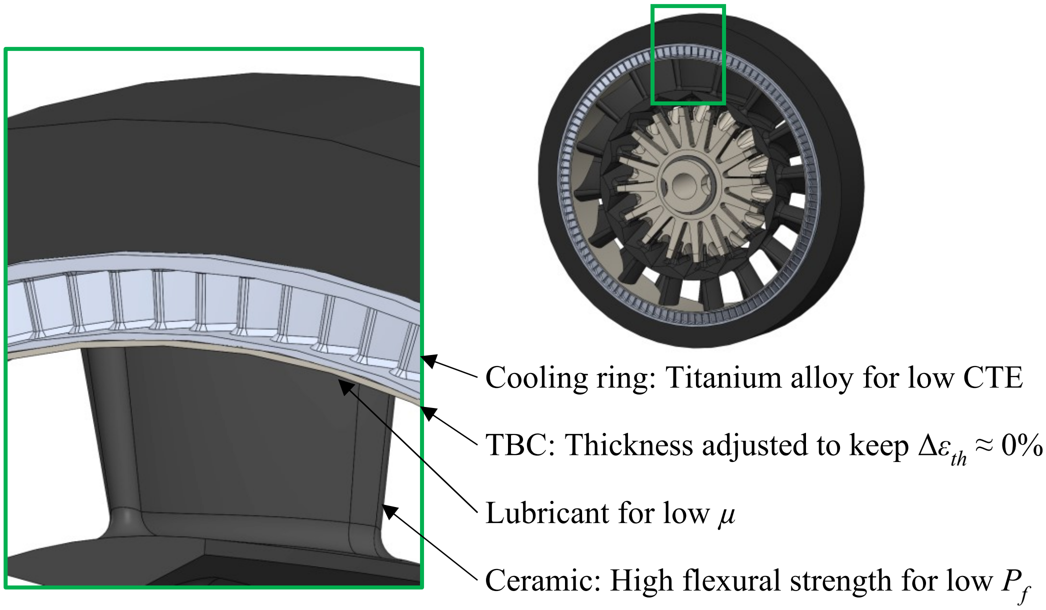

Figure 4.23 Conceptual conclusions from this chapter

It must be noted that important assumptions were made for simplifying the numerical setup. First, block-shaped "blades" were used instead of actual airfoils. It is assumed that stresses are representative of an ICT blade tip stress state nonetheless. Second, the contact patch in the FE model is forced to be as constant as possible along the entire "blade" surface, thus the conclusions concern contact aspect ratio than simply the blade aspect ratio, as in reality the blade extremities may unstick from the surface.

These conclusions are reinforced by the findings in Chapter 3, and confirm that reducing μ is a primary target for future development. Furthermore, a reduction in difference in thermal expansion can also help in reducing P_f. The designer has a limited latitude for these design variables, through lubrication and thermal management. TBC and hexagonal boron nitride (hBN) lubricant are explored experimentally in Chapter 5, to provide an assessment of whether these materials can be used in the ICT. TBC is already considered for ICT rotor design for thermal management, however it can also play a role in blade tip stress levels by managing thermal expansion of the substrate. hBN is among the only high-temperature lubricants which could withstand turbine operating temperatures and was identified as a candidate in Chapter 3.

CHAPTER 5

THERMAL BARRIER COATING

This chapter is divided into two feasibility studies for evaluating courses of action which should be taken to reduce blade tip stresses, as identified in Chapter 4. The first half investigates the viability of a thermal barrier coating to reduce the thermal expansion mismatch between the cooling ring and the blade tip. The thermal barrier coating (TBC) is applied to the inner skin of the ICT shroud. This work was presented at the ASME Turbo Expo 2021 and the proceedings paper is included below. The second half of this chapter investigates the use of boron nitride as a solid lubricant at the interface for reducing the coefficient of friction, under high load and at high temperature.

5.1 Foreword

TBC is the most widely used material in the turbine hot section designer's catalog for forcing a large temperature gradient across a thin layer. The very low thermal conduction of TBC, of the order of 1-2 W/m°C, means that it forms a significant resistance to heat flow. TBC had already been considered for the ICT shroud to cut down on cooling flow, however it could also be used as a control layer for thermal expansion of the cooling ring. Simply put, reducing the heat flux to the cooling ring keeps the cooling ring cooler and the blade hotter, and therefore reduces the gap in thermal expansion.

However, past iterations of the inside-out rotor architecture did not include TBC, and the typical use case of TBC does not involve much direct mechanical loading. Therefore, there is no information in the literature as to whether TBC can sustain the loads inherent to the ICT's structural shroud. The following paper, in Sections 5.2 through 5.8, presented at the ASME Turbo Expo 2021 conference, shows a series of experimental results, all of which point toward TBC being highly suited for use on the inner skin of the ICT structural shroud.

- **Title**: Thermal Barrier Coating Applied to the Structural Shroud of an Inside-Out Ceramic Turbine
- **Authors**:
    - Patrick K. Dubois, PhD candidate, University of Sherbrooke, Faculty of Engineering, Createk Innovation Group (Contributions: Test planning and execution, analyses)
    - Antoine Gauvin-Verville, Master's student, University of Sherbrooke, Faculty of Engineering, Createk Innovation Group
    - Benoît Picard, Chief Engineer, Exonetik Turbo Division
    - Jean-Sébastien Plante, Professor, University of Sherbrooke, Faculty of Engineering, Createk Innovation Group
    - Mathieu Picard, Associate Professor, University of Sherbrooke, Faculty of Engineering, Createk Innovation Group
- **Date of acceptance**: April 15th, 2021
- **State of acceptance**: In press
- **Publication**: Proceedings of ASME Turbo Expo 2021 Turbomachinery Technical Conference and Exposition
- **Reference**: Dubois, P.K. et al., 2021, "Thermal Barrier Coating Applied to the Structural Shroud of an Inside-Out Ceramic Turbine," Proceedings of ASME Turbo Expo 2021 Turbomachinery Technical Conference and Exposition, Ahead of press.
- **Version**: Final, with corrections required by reviewers. Adapted to institutional thesis format, sections renamed for clarity within this chapter.

French title

« Revêtement de barrière thermique appliqué au carénage structurel d'une turbine en céramique renversée »

French abstract

Les microturbines (< 1 MW) récupérées à haute température pourraient être un facilitateur clé pour les groupes motopropulseurs hybrides des petits avions de demain. Pour atteindre des rendements thermiques compétitifs, la température d'entrée de la turbine (TIT) doit augmenter jusqu'à 1550 K, bien au-delà des limites conventionnelles des microturbines métalliques. Cela

nécessite des céramiques réfractaires à haute température, qui requièrent une nouvelle conception de microturbine spécifique à la céramique, comme la turbine en céramique renversée (ICT). Cette étude se concentre sur l'applicabilité d'un revêtement de barrière thermique (TBC) à la surface interne de l'anneau de refroidissement de la ICT. En réduisant le flux de chaleur de l'écoulement principal vers le carénage, l'utilisation d'un TBC dans une ICT permet une TIT plus élevée et un débit massique d'air de refroidissement plus faible.

Une évaluation expérimentale préliminaire est effectuée à température ambiante sur des revêtements de 1 mm d'épaisseur de zircone stabilisée à l'yttria à 8 % (8YSZ), pulvérisée au plasma à l'air (APS) TBC, appliquée sur des coupons d'essai en Inconel 718 et Ti64. Les résultats montrent que le comportement fortement orthotrope du TBC testé correspond parfaitement à la mécanique de déformation de la configuration ICT sous charge. Premièrement, une grande tolérance de déformation dans le plan permet la grande déformation tangentielle imposée par le carénage structurel sous charge centrifuge. Deuxièmement, une rigidité hors plan et une résistance à la compression élevées se combinent pour supporter des charges de compression extrêmes sans aucun dommage apparent au TBC, même à plus de 3 fois la charge moyenne d'indentation de la pale de turbine. Une démonstration expérimentale sur un prototype à petite échelle montre une réduction de 40 % du débit de refroidissement dans un test ICT de 8 minutes, sans endommager le TBC, démontrant l'efficacité et le potentiel de la conception proposée.

Thermal Barrier Coating Applied to the Structural Shroud of an Inside-Out Ceramic Turbine

5.2 Abstract

Recuperated, high-temperature microturbines (< 1 MW) could be a key enabler for hybrid powertrains of tomorrow's small aircraft. To achieve competitive thermal efficiencies, turbine inlet temperature (TIT) must increase to 1550 K, well beyond conventional metallic microturbine limits. This calls for high-temperature refractory ceramics, which call for a new ceramic-specific, microturbine design like the Inside-Out Ceramic Turbine (ICT). This study focuses on the applicability of a refractory thermal barrier coating (TBC) to the internal surface of the ICT cooling ring. By cutting the heat transfer from the main flow to the structural rim-rotor, the use of a refractory TBC coating in an ICT enables higher TIT and lower cooling air mass flow.

A preliminary experimental assessment is done at room temperature on 1 mm-thick coatings of 8% yttria-stabilized zirconia (8YSZ), air plasma sprayed (APS) TBC, applied to Inconel 718 and Ti64 test coupons. Results show that the strongly orthotropic behaviour of the tested TBC fits perfectly with the deformation mechanics of the ICT configuration under load. First, large in-plane strain tolerance allows the large tangential deformation imposed by the structural shroud under centrifugal loading. Second, high out-of-plane stiffness and compressive resistance combine to support extreme compressive loads with no apparent damage to the TBC even at more than 3 times blade indentation average loading. An experimental demonstration on a small-scale prototype shows a reduction of 40 % in cooling flow in a 8-minute ICT test, with no damage to the TBC, proving the effectiveness and potential of the proposed TBC design.

Keywords: Thermal Barrier Coating, TBC, Orthotropic mechanical properties, Inside-out Ceramic Turbine, ICT.

5.3 Acronyms

APS	Air Plasma Spray
BC	Bond Coat
DIC	Digital Image Correlation
EDS	Energy-Dispersive X-ray Spectroscopy
FE	Finite Element
ICT	Inside-out Ceramic Turbine
SEM	Scanning Electron Microscope
TBC	Thermal Barrier Coating
TC	Top Coat
UTM	Universal Testing Machine
YSZ	Yttria-Stabilized Zirconia
μCT	Micro Computed Tomography

5.4 Introduction

Sub-MW turbines, or microturbines, could be an ideal power generation unit for short- to mid-range missions in the future for regional hybrid turboelectric aircraft [47]. They offer an appealing power density and fuel efficiency in a recuperated Brayton cycle, provided they operate at a sufficient TIT [46]. Considering the lack of cooling technology in the microturbine segment, the transition to ceramics could enable the significant jump in TIT required to achieve competitive recuperated cycle efficiency, i.e. a TIT minimum of 1550 K [48]. This has motivated work on the inside-out turbine (ICT) rotor architecture, a novel microturbine rotor design [10,75].

The ICT maintains the blades in compressive loading by means of a structural rotating shroud. The overall compressive state of the blades increases reliability in ceramic rotor blades, which has been the main issue in the development and adoption of ceramic turbines in the past [76]. The structural shroud is the key component for the integrity of the ICT, as it bears the centrifugal loading of the rotor. This shroud is composed of a composite hoop with a shrink fit cooling ring, as shown in Figure 5.1.

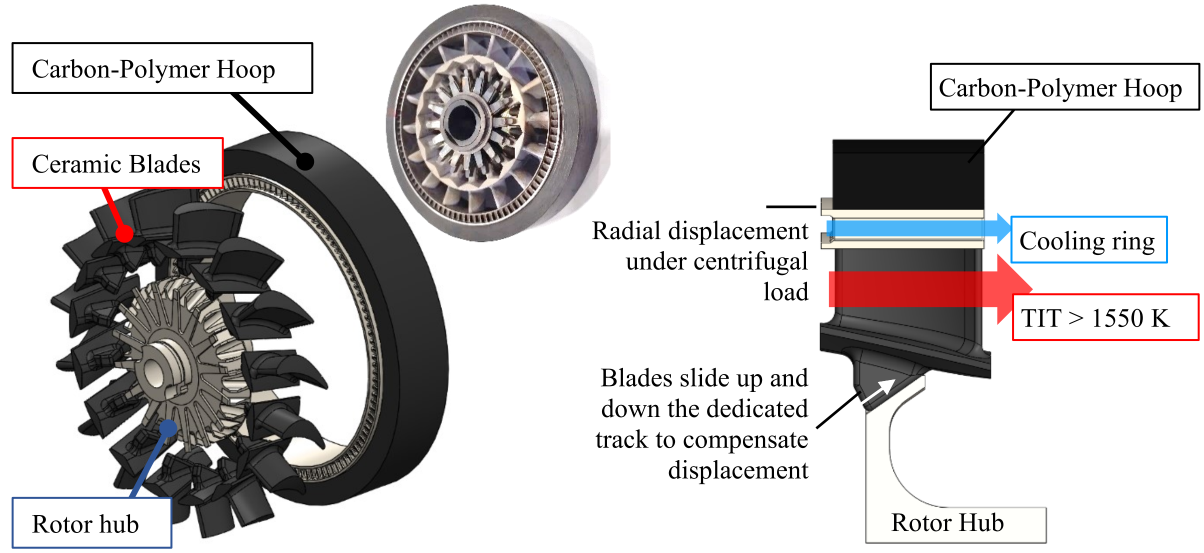

Figure 5.1 The inside-out ceramic turbine (ICT) rotor components and working principle

Carbon-polymer composite is the only material with sufficient specific strength and specific stiffness to withstand the centrifugal loading in the ICT. A heavier material would simply expand to failure under its own weight. The use of a polymer-based composite does require cooling, for the polyimide composite matrix to remain below its glass transition temperature of 600 K. Higher temperature matrices are too brittle (e.g. ceramic matrix, CMC) or too heavy (e.g. metal matrix, MMC).

The carbon-polymer hoop is the most coolant-intensive component in the turbine rotor since its inner surface is close to the main flow. A cooling ring must therefore be placed in between the structural carbon-polymer hoop and the main flow in order to create a large radial temperature gradient between the hot gas flow and the composite hoop, amounting to a temperature drop of roughly 1000 K over 3 mm. Even though the cooling ring remains a challenge, it simplifies cooling considerably compared to cooling metallic blade with intricate, hard to manufacture, internal cooling passages.

Cooling rings for ICT must remain at an adequate operating temperature. Past iterations relied solely on air-cooling through superalloy microchannels [33,77]. However, because of the mismatch in operating temperature between a metallic ring and ceramic blades, the blade-ring remains at a lower temperature and therefore cools the blade tips by heat conduction. This is counterproductive in the effort to fully benefit from ceramics in high-temperature turbine rotors.

As is the case in state-of-the-art turbines, the addition of a thermal barrier coating (TBC) should help in reducing the amount of heat extraction [78]. TBC systems comprise three layers: the superalloy substrate, a bond coat, and a top ceramic coat. They are applied to turbine blades to reduce metal surface temperature by inducing a severe temperature drop through the TBC top coat. TBC would be coated on the cooling ring's inner skin, as shown in Figure 5.2.

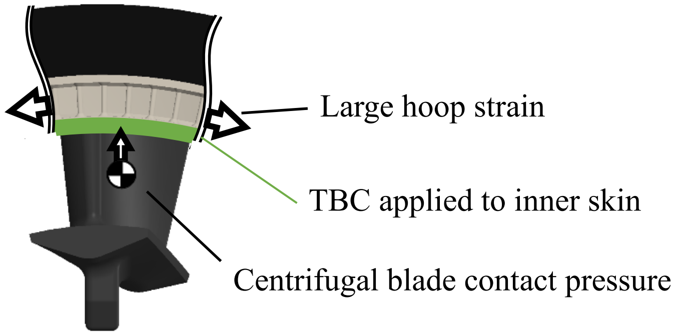

Figure 5.2 Thermal barrier coating (TBC) is applied to the inner skin of the ICT cooling ring, which undergoes two distinct mechanical loadings

The expected thermal management benefits of TBC in an ICT are twofold: (i) shield convective heat transfer to the structural shroud from the hot gases and (ii) cut conductive heat losses from the blade tips to the cooling ring. These are fundamental benefits for the ICT, which will enable it to achieve a significant increase in TIT with low cooling flow. An additional benefit of TBC could be the introduction of titanium-based alloys for the cooling ring material. The lower density and considerable strength of titanium alloys could help reduce hoop stress in the carbon rim at high rotational speed.

TBC in this context would be submitted to an unconventional set of loads. The ICT cooling ring undergoes 3 types of mechanical loads: (i) hoop strain under centrifugal loading, (ii) localized pressure of the blades' contact patch and (iii) thermal expansion as the turbine wheel heats up. Considering that TBC is typically quite strain tolerant and fairly hard [74,79], it is surmised that it should suit the application. A wealth of literature goes into thermal expansion mismatch within the TBC system [80], and standardized test methods exist to determine TBC adhesion [81]. However, little data is available for the adhesion of TBC to a substrate which undergoes high strain while being submitted to local constant normal forces from large bodies such as ceramic blade tips in an ICT. Therefore, this paper conducts an experimental assessment of the viability of using TBC under the particular loads of ICT cooling rings. Three critical test programs are conducted in growing order of complexity: (1) static tensile strain tests at room temperature, (2) macro-indentation tests at room temperature, followed by (3) high-temperature rotor tests on a fully-functional ICT prototype turbine wheel. Results are presented and analyzed to conclude on the potential and challenges of using TBC for ICT.

5.5 Materials and Methods

Strain tolerance of the TBC was evaluated via tensile testing. Compressive resistance was tested using various indenters on flat coated specimens. Turbine conditions were replicated in a 20-kW-scale turbine rotor test rig on an ICT rotor prototype. All test items were coated with air plasma sprayed (APS) 8 wt% yttria-stabilized zirconia (8YSZ) and tested in as-sprayed condition. 8YSZ is one of the most readily available types of TBC and was chosen for this first assessment of suitability for the ICT configuration. Coating was done by Nevada Thermal Spray Technologies (USA).

For static tests, coated alloy sheets were water jet cut into test coupons appropriate for tensile strain tests and indentation tests. Two sheet metal substrates, ASTM B670 Inconel 718 (In718) and ASTM B265 Titanium 6Al-4V (Ti64), were used to represent both Ni-based superalloys and Ti-based alloys respectively, as they are both candidates for the cooling ring substrate material. The TBC system layers are listed in Table 5.1 and a scanning electron microscope (SEM) cut view of the coated In718 coupon is shown in Figure 5.3.

Table 5.1 Materials used in this work

TBC Layer	Thickness	Ni Alloy Substrate	Ti Alloy Substrate
Substrate	3.18 mm	Inconel 718	Titanium 6Al-4V
Bond Coat	100 µm	Ni5Al (Metco 450)	NiCrAlY (Praxair NI-211)
Top Coat	1000 µm	8YSZ (HAI HA 9204)	

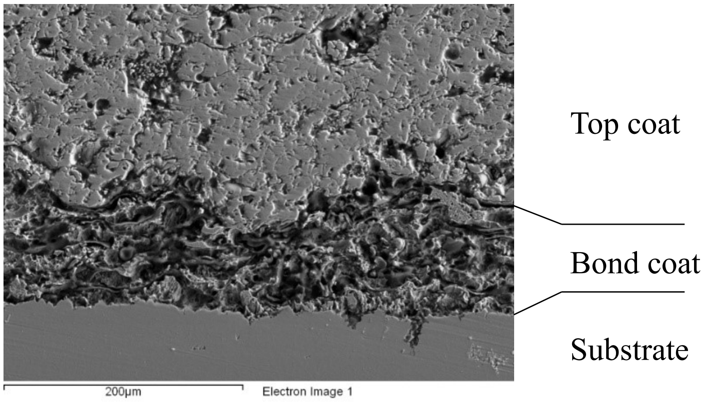

Figure 5.3 Scanning electron microscope (SEM) image of a cut section of the Inconel 718 coated coupon

5.5.1 Static tensile strain tests

Tensile tests were run at room temperature. Due to available coated sheet size restrictions, the tensile coupons were shorter than standard ASTM E8 size. All test coupons are shown in Figure 5.4 and their dimensions are given in Table 5.2. Testing procedure was completed to coupon rupture, and spallation was noted upon occurrence. As shown in Figure 5.4, some Ti64 coupons had no bond coat (BC) to investigate the effects of a BC on failure mode.

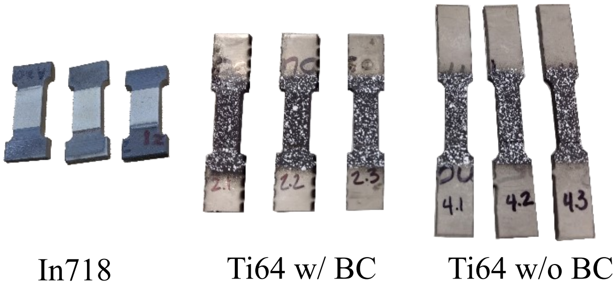

Figure 5.4 Tensile coupons for adhesion testing under high directional strain for Inconel 718 and Ti64 substrates. Ti64 coupons are painted with the stochastic speckle required for DIC

Table 5.2 Tensile coupon dimensions and test conditions

Substrate	TBC dimensions	Strain rate	No of specimens
In718	16 mm x 10 mm	0.25 mm/min	3 with BC
Ti64	25 mm x 6 mm	0.13 mm/min	3 with BC 3 without BC

In718 tests were run on an Instron 33R4206 100 kN universal testing machine and Ti64 was tested on an MTS 322 100 kN universal testing machine. To gain better understanding and granularity of TBC failure, Ti64 tests were coupled with Correlated Solutions VIC-3D digital image correlation (DIC) system [82]. The DIC setup is shown in Figure 5.5. The stochastic pattern on the Ti64 coupons was applied using aerosol paint through a fine steel mesh.

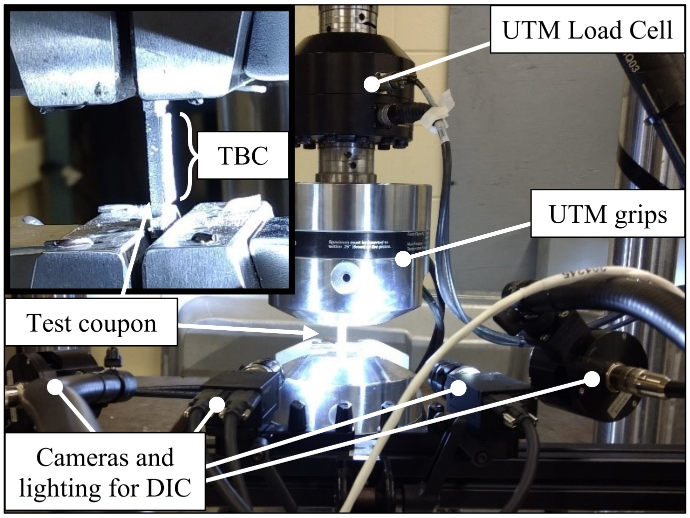

Figure 5.5 Test rig in a universal testing machine (UTM), with digital image correlation (DIC) tracking spallation on Ti64 coupons

For the In718 specimens, TBC failure was denoted visually, and energy-dispersive X-ray spectroscopy (EDS) was conducted with an Oxford Instruments X-Max 50 on the spalled interface to determine where spallation had occurred. For the Ti64 specimens, the DIC setup monitored the adhesion of the TBC and thus its failure was recorded in image post-treatment.

5.5.2 Macro-indentation tests

Indentation tests were run at room temperature on the In718 substrate only, as damage propagation within the top coat is the investigated mechanism and estimated to be substrate-agnostic under testing conditions. Square coated coupons were placed in a hydraulic press, monitored with a Transducer Techniques SBO-2K 2000 lb S-beam load cell. Three indenters were used for successively increased average pressure: a planar CeramTec (Germany) SL200BG silicon nitride turbine airfoil, a 3.18 mm diameter steel dowel pin and a 2 mm diameter steel dowel pin. They allow an indentation pressure up to 2830 MPa – much higher than the average blade pressure (300-500 MPa), given by the hydrostatic pressure of a silicon nitride blade at a tip speed of 450 m/s. The test rig is shown in Figure 5.6.

The hydraulic press is equipped with a pressure gauge, which was calibrated with the S-beam load cell to achieve higher, although less precise, compressive loads. Load increments were stopped at indenter failure. Table 5.3 shows the indenters and the maximum achieved average compressive stress.

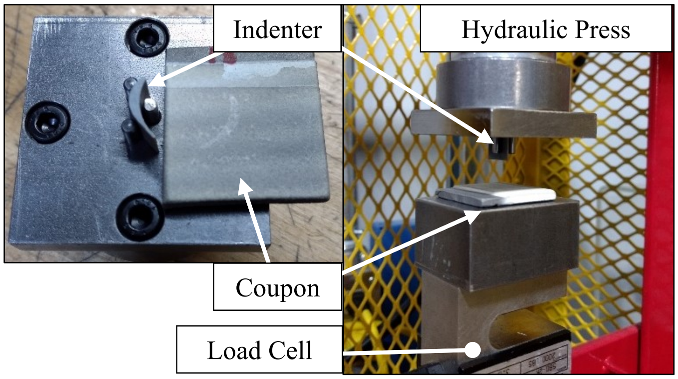

Figure 5.6 Indentation test rig

Table 5.3 Compressive loading values achieved with different indenters

	Ceramic airfoil	**3.18 mm Dowel Pin**	**2 mm Dowel Pin**
Contact pressure range (MPa)	200 - 1780	200 - 2250	500 - 2830

Indent depth and surface roughness was measured on the top coat using a Keyence VR-5000 3D optical profiler. Roughness was calculated using average spanwise and lengthwise profiles, corrected according to standard ASME B46.1. Mean roughness was $R_a = 11$ µm and peak roughness was $R_z = 70$ µm. Internal damage propagation was assessed using a Nikon XT H 225 computed tomography system (µCT scanner). The µCt scanner X-ray was set at 220 kV and 50 µA, with a copper filter. The resulting voxel cube side length was 22 µm.

5.5.3 High-temperature rotor tests

Field testing was conducted in an existing 20-kW-scale prototype turbine wheel. The prototype wheel used a polyimide-carbon fiber composite hoop and a 3D-printed In718 cooling ring, printed on a GE Additive Mlab 200R using AP&C In718 15-45 µm powder stock. An APS TBC layer consisting of 100 µm NiAl bond coat and an 8YSZ top coat was applied to the cooling ring inner skin, diamond-ground down to a thickness of 700 µm. The blades were 3D-printed

In718, to mitigate the added risk of using ceramic blades in this first trial with TBC. As blades are uncooled in the ICT, TIT was reduced to 1223 K, a safe temperature for short-term testing with In718 blades. Seeing as metal blades and the TBC layer add mass to the rotor assembly, rotational speed was scaled down to 80 000 RPM (tip speed 242 m/s) to ensure the structural composite hoop did not exceed ultimate strength, meanwhile imposing pressure and hoop strain on the TBC similar to standard ICT conditions. These operating conditions were determined via FE analysis, using temperature-dependent material properties. The prototype is shown in Figure 5.7.

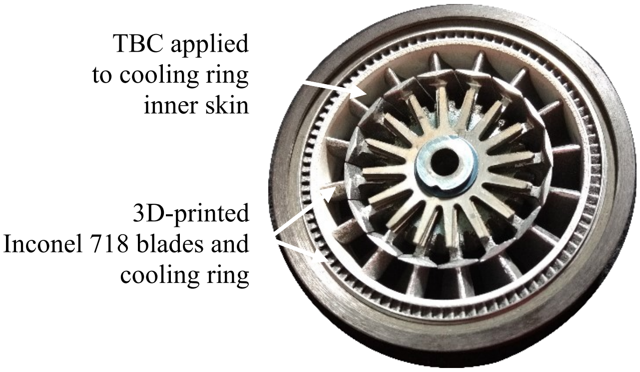

Figure 5.7 ICT prototype wheel for initial testing of TBC applied to the inner skin of the cooling ring

5.6 Results and Discussion

Results of the experiments conducted on the APS TBC suggest highly orthotropic properties, i.e. high in-plane strain compliance and out-of-plane indentation resistance, as well as an effective thermal barrier for the ICT.

5.6.1 Static tensile strain results

Coated In718 results indicated that TBC adheres well all the way to yielding of the substrate. All three tested coupons spalled exactly at the onset of the expected yield stress of In718. Figure 5.8 shows the typical failure observed.

EDS results in Figure 5.8 indicate that spallation occurred at the interface between the bond coat and the top coat, with top coat still attached to the coupon after spallation of the main bulk.

Upon coupon rupture, the bond coat pulverizes and little if none remains present on the substrate. Most of it could be found as a fine powder near the failed coupon.

DIC tracking on the Ti64 substrate coupons confirmed this behavior. Strain was tracked on the TBC as well as the substrate. A significant difference in strain was observed when the TBC spalled off the substrate. This point was systematically achieved at substrate yield, as noted in Figure 5.9. Substrate necking is the most probable cause of TBC spallation, which induces heavy shearing at the interface.

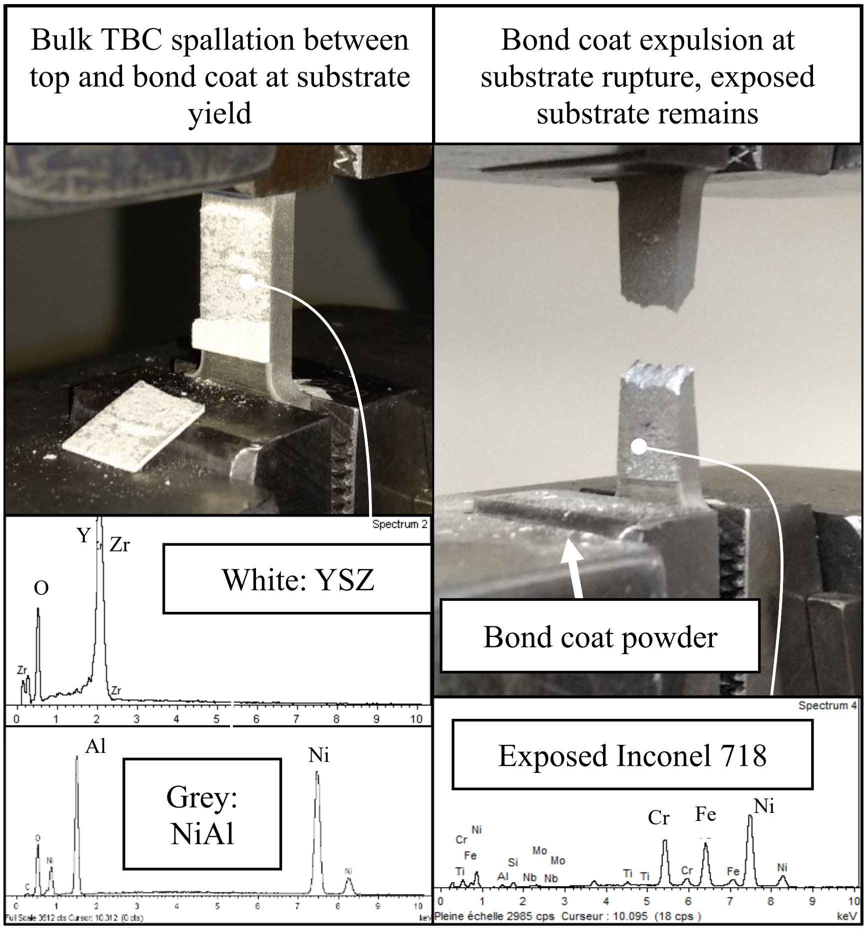
Bulk TBC spallation between top and bond coat at substrate yield

Bond coat expulsion at substrate rupture, exposed substrate remains

Figure 5.8 Tensile test spallation results for Inconel 718 coupons, along with EDS spectrum results after spallation (left) and rupture (right)

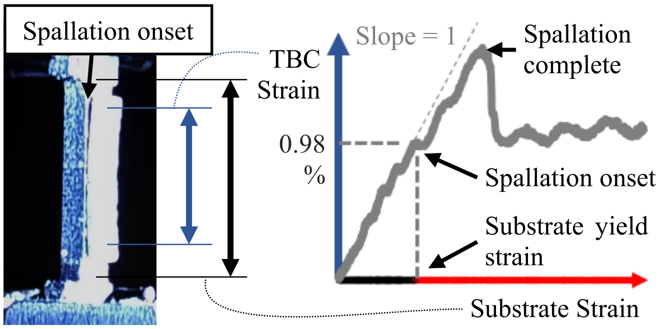

Figure 5.9 Correlation between onset and complete spallation with substrate strain, based on DIC tensile test results (left)

The addition of a NiCrAlY bond coat to the TI64 substrate adds gracefulness to the spallation, i.e. the TBC does not spall suddenly but rather peels off the surface, as can be seen in the test illustrated in Figure 5.9. Top coat applied directly to the substrate with no bond coat spalled abruptly, as soon as yield strength was reached. The bond coat did not change the strain value at which spallation onset occurred since it seems to be governed by the substrate material's necking upon yield.

5.6.2 Macro-indentation results

Although tested under extreme compressive loads, the top coat did not fail in any catastrophic way. Visible examination of the indents shows that roughness was smoothed out at around 400 MPa contact pressure, leaving a visual imprint on the TBC. This proved to be a cosmetic surface change, as confocal microscopy did not reveal any indent imprints before 1000 MPa average contact pressure, and very little indent accumulation even up to contact pressures of 2830 MPa. The most visually obvious damages are shown in Figure 5.10.

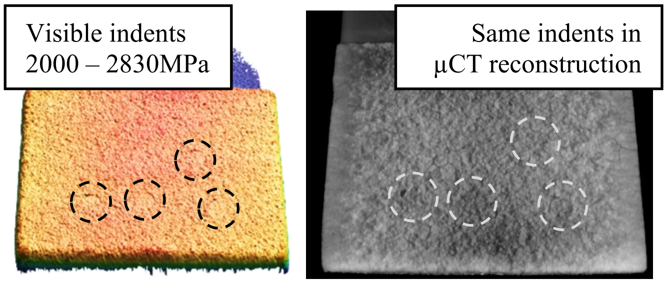

Figure 5.10 Confocal (left) and µCT (right) imagery used to determine permanent damage under macroscopic indentation

Micro-computed tomography (µCT) analysis allows to see the internal damage that occurred after macro-indentation. This was done by observing the circular imprint damage pattern caused by the dowel pin through the layers of the top coat. Damage at low depth is sharp and easily identified, but quickly blends as it penetrates the top coat. Observable internal damage was detected starting at an average contact pressure of 1400 MPa. Figure 5.11 shows the extent of observable damage under µCT scanning. Maximum achieved damage depth was 260 µm, shown in Figure 5.11, under a contact load of 2830 MPa.

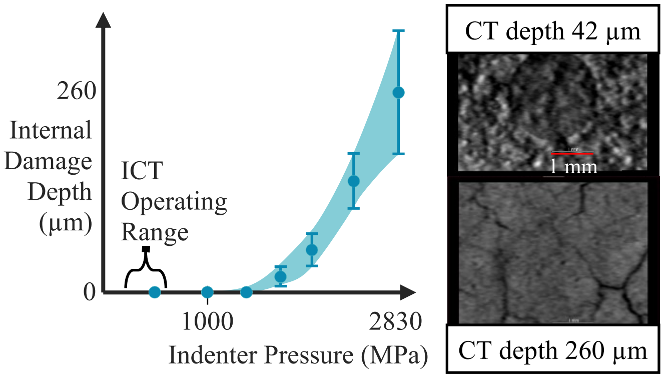

Figure 5.11 Indentation permanent damage range due to macroscopic indenters, evaluated with µCt scan, is beyond the pressure range applied by ceramic blades in the ICT

5.6.3 High-temperature rotor results

After both the strain and indentation tests, it was deemed safe to run tests in a turbine rotor. An 8-minute field test with In718 blades and an In718 cooling ring indicated a reduction from 25 to 15 g/s (-40 %) in required cooling mass flow to achieve a cooling flow outlet temperature of 419 K, with cooling flow inlet at room temperature. This confirms the initial motivation of applying TBC to this surface.

Figure 5.12 shows the TBC after the tests. Blade prints are cosmetic, due to carbon deposits. The TBC suffered no damage during tests, indicating it can support the ICT-specific mechanical loads. Testing with the proper materials will validate whether operating with ceramic blades causes any issue with the TBC.

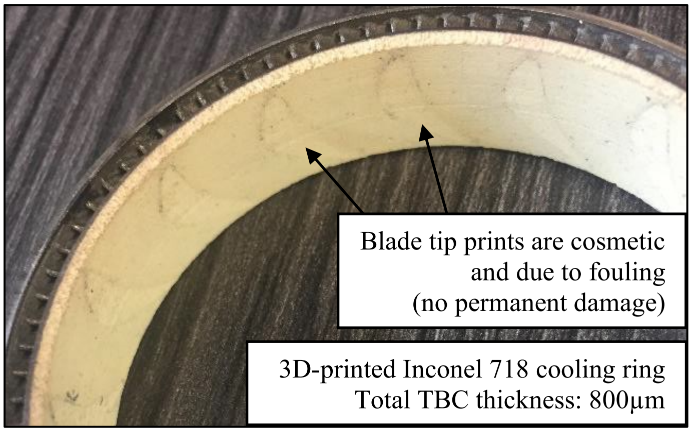

Figure 5.12 Cooling ring removed from the carbon hoop showed no sign of degradation during tests after turbine rotor testing

5.7 Conclusions

The use of a structural, polymer-based composite rotating structural shroud in the ICT rotor requires an aggressive cooling component, to properly make use of the refractory ceramic blades it supports. This component is a metallic air-fed cooling ring. The addition of TBC reduces cooling requirements and enables higher TIT for a given set of structural shroud materials. More specifically, the orthotropic characteristics of APS YSZ TBC are tailored to the high hoop strain and high normal load applied to the cooling ring substrate. Although limits were found in the TBC in both static tensile and indentation testing, they were well outside the expected ICT operating envelope, which indicates good compatibility with the ICT rotor.

Tensile tests with two substrate materials – In718 and Ti64 – in conjunction with DIC, confirmed that spallation of the TBC occurred at substrate yielding, in all likelihood due to substrate necking. Indentation tests with macro-scale indenters showed that the out-of-plane strength of APS TBC allows it to resist extreme normal loading, up to 1000 MPa before notable permanent internal damage, measured with confocal microscopy and µCT imagery.

Both of these properties were confirmed to enable the use of TBC in the ICT configuration with a functional, 20-kW-scale turbine rotor prototype. Initial tests using a nickel-based In718 cooling ring indicated a 40 % drop in required cooling flow.

TBC is paramount in achieving the target operating conditions of the ICT. This first assessment has shown that it is compatible with the specific loadings of the cooling ring in as-sprayed conditions. Further investigation will be necessary to study long-term compatibility of TBC under ICT load cases, including high temperature creep, sintering and stiffening [83,84]. However, these initial results offer confidence in the use of TBC in further ICT designs.

5.8 Acknowledgements

The authors would like to thank the research personnel at Université de Sherbrooke. Funding for the project is provided by the Natural Sciences and Engineering Research Council of Canada (NSERC), Defence Research and Development Canada (DRDC), the Government of Québec and Exonetik Turbo. Special thanks go out to personnel at École de technologie supérieures – LAMSI for their expertise in computer tomography. Funding for the first author is provided by Fonds de recherche du Québec – Nature et technologies (FRQNT).

CHAPTER 6

BLADE TIP INTERFACE LUBRICATION

6.1 Introduction

As determined in Chapter 4, reducing the coefficient of friction at the interface between the blade and the structural shroud has the most significant impact on blade reliability. This chapter aims at gaining an experimental assessment of the use of hexagonal boron nitride as a lubricant between the blade tip and structural shroud.

Boron nitride occurs in 4 different forms: hexagonal, cubic, amorphous and wurtzite. The form of interest here is hexagonal (hBN), for its lubricant capabilities and thermal stability. Boron nitride is a widely used lubricant for intense applications, such as high-temperature mold release or as a high-temperature lubrication additive [85]. Its slipperiness originates from its molecular structure, pictured in Figure 6.1.

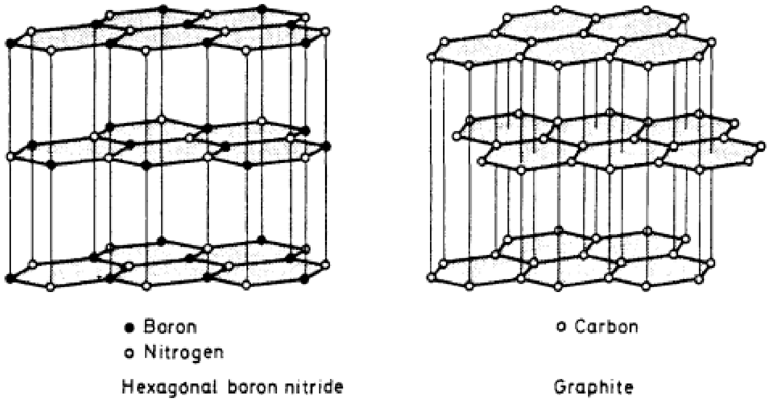

Figure 6.1 Similarity between the sheet-like form of hexagonal boron nitride (left) and graphite (right) Source: [85]

Like graphite, the weak Van der Waals forces between the flat hBN molecule sheets allow them to slide along each other with little resistance. However, unlike graphite, hBN is much more stable at high temperatures and doesn’t oxidize before 1100 °C in oxidizing environments [86]. hBN can be applied in a variety of different ways, including plating, thermal spraying, and aerosol. These properties make hBN an interesting candidate for applying at the high-friction, high-temperature interface between the blade tip and the structural shroud.

The ICT blade tip is under a large normal load. This chapter focuses on quantifying the reduction of frictional stresses under similar loads, with thermally induced strain. Several methods of hBN application are tested under light load, to quantify expected coefficient of friction. Following this, high normal load contact between silicon nitride and hBN is compared against TBC and direct Inconel, to assess potential improvement of application of hBN to the internal skin of the cooling ring.

6.2 Materials and Methods

The experimental evaluation of hBN was done in two consecutive steps: validation of its low coefficient of friction using a standard ASTM room-temperature friction test, followed by high-temperature, high-load validation in a thermomechanical press paired with digital image correlation (DIC). Results were compared to friction on bare Inconel and on TBC using the same two test methods. The ASTM test method is non-destructive and simpler to execute, thus more interfaces were tested than on the thermomechanical press, where only one type of hBN application was tested. The tested interfaces are listed in Table 6.1 and shown in Figure 6.2.

Table 6.1 Materials used for hBN friction tests

Interface Type	Thickness	ASTM test	Thermomechanical test
Bare Inconel 718	3.18 mm	✓	✓
Oxidized Inconel 718	3.18 mm	✓	
TBC (unground)	1000 µm	✓	
TBC (ground)	800 µm		✓
APS* hBN	100 µm	✓	✓
Microslik hBN	1-75 µm**	✓	
Lubricoat hBN	N/A	✓	

*APS: Air plasma spray
**Typical thickness according to manufacturer datasheet

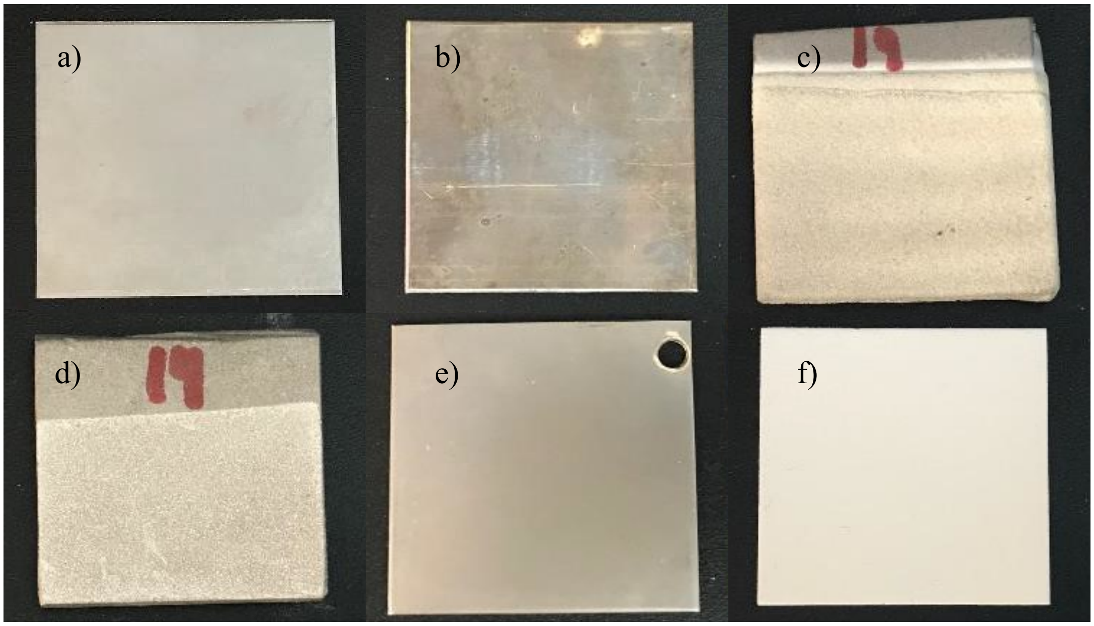

Figure 6.2 Interfaces used for friction tests: a) bare Inconel 718; b) oxidized Inconel 718; c) TBC; d) APS hBN; e) Miroslik (electroless plating) hBN; f) Lubricoat (aerosol) hBN

The test specimens are all Inconel 718 plates, roughly 1 inch x 1 inch. Oxidation of the specimens is done in a furnace, in an air environment at 800 °C for 1 hour. TBC is applied by air plasma spray, as described in Section 5.5, Table 5.1. Grinding of the TBC is done using a 0.25" diamond-grit wheel in a coolant-fed milling machine, where 0.008" is removed, as shown in Figure 6.3. Nevada Thermal Spray Technologies also applied the APS hBN with air plasma spray. Precise chemical composition of the APS hBN is unknown, and deposited material porosity is 2 %.

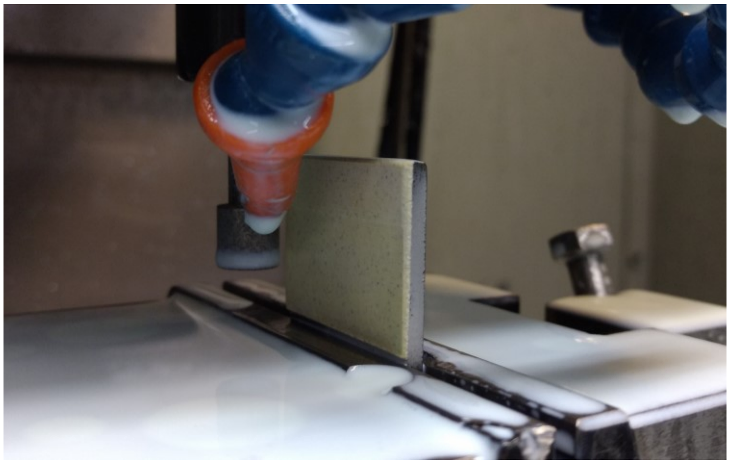

Figure 6.3 Coolant-fed diamond grinding setup for TBC specimens

Microslik® is a phosphorous-boron-nitride compound which can be applied to nickel alloys through electroless plating. This process uses an autocatalytic reaction between the coating and substrate to achieve uniform coating without the need for electrodes. Lubricoat® is a hBN-based mold release agent developed by ZYP Coatings. In this instance, it was applied with an aerosol spray. Except for respiratory protection, the simple application of Lubricoat makes it an interesting candidate for prototypes and for large-scale production.

6.2.1 Ambient conditions tests

The first test run is done using a rig inspired by ASTM Standard D1894-14 [87]. Tests are done with a TA.XT Plus texture analyzer, used as a tensile testing machine with a 10 N load cell, as shown in Figure 6.4.[3]

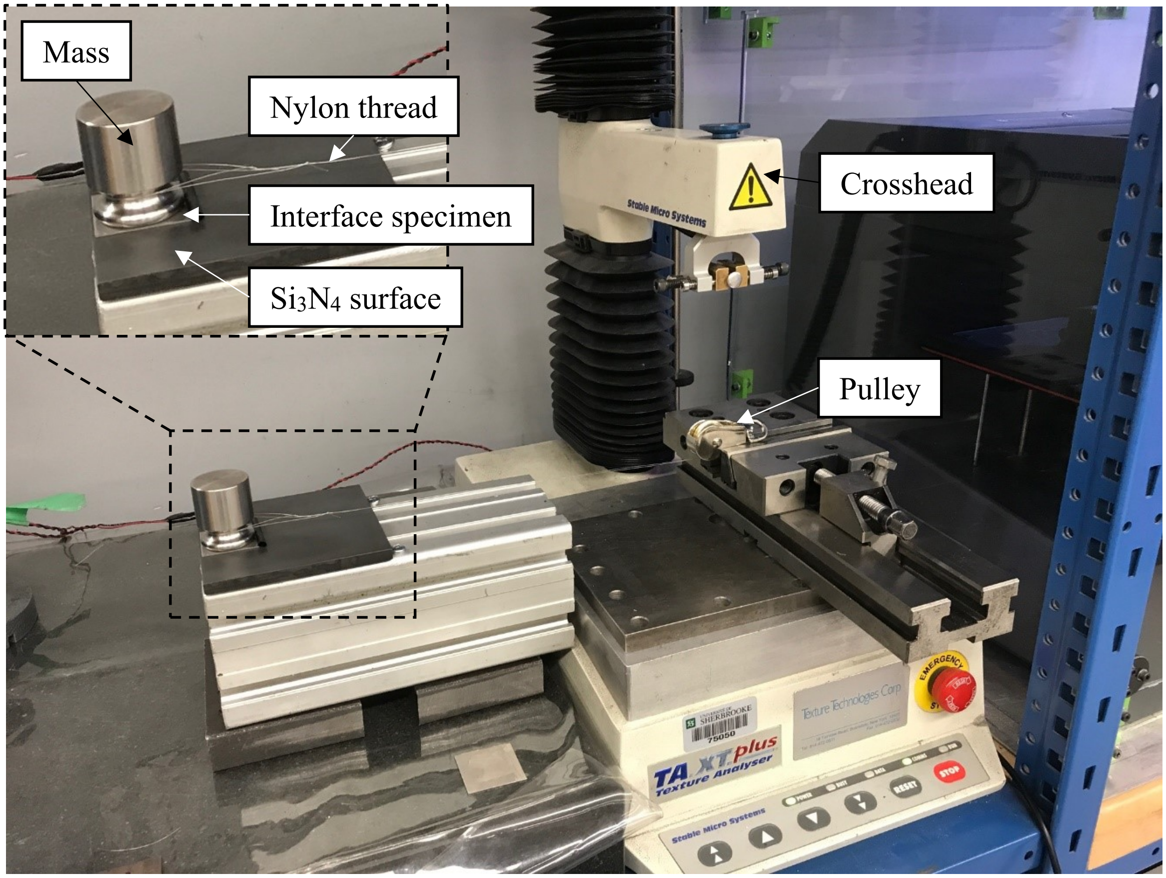

Figure 6.4 Testing apparatus for ASTM D1894-14 coefficient of friction tests

---

[3] *Tests described in Section 6.2.1 were designed and performed by Simon Richard, research engineer at Université de Sherbrooke, Createk Innovation Group.*

Although this testing apparatus setup is not explicitly listed in standard D1894-14, the overall concept remains sound: the only modification resides in the fact that the crosshead also acts as the load cell. A 0.23-mm nylon string was attached from the machine's crosshead, through a pulley, to a 200 g mass. The test sequence is as follows:

a) Place the specimen face down on the Si_3N_4 plate. Take care to align the specimen's trajectory with an area devoid of any surface imperfections on the plate.
b) Place the 200 g mass on the interface specimen. Lightly preload the nylon string to reduce system backlash.
c) Set the crosshead speed at 2 mm/s, for a 20 s test.
d) Test each specimen 3 times.

Both static and kinetic coefficients of friction μ_s *and* μ_k can be found by simply dividing the force F required to drag the specimen along the test surface by the weight (Mg) of the specimen, as shown in Eq (6.1).

$$\mu = \frac{F}{Mg} \tag{6.1}$$

Static coefficient of friction μ_s is determined by using the force just prior to when motion starts, or the maximum resistance offered by the system. Kinetic coefficient of friction μ_k is determined by using the stabilized force required to keep the specimen in motion.

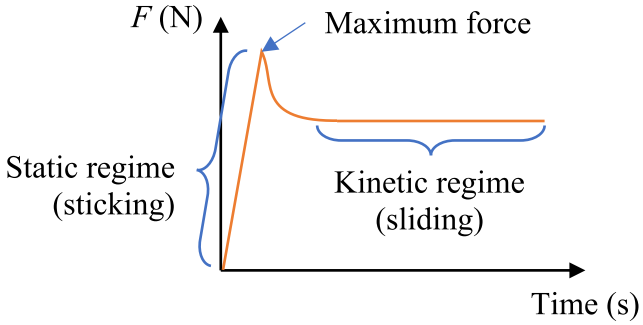

Figure 6.5 Typical friction test curve, illustrating the two frictional regimes quantified by the test

The static coefficient of friction μ_s is deemed to be the parameter of interest in this part of the study, as it represents the maximum force which can be applied at the frictional interface.

Following coefficient of friction tests, APS hBN specimens are mounted in the same indentation test rig as described in 5.5.2, using the same test method, as pictured in Figure 6.6.

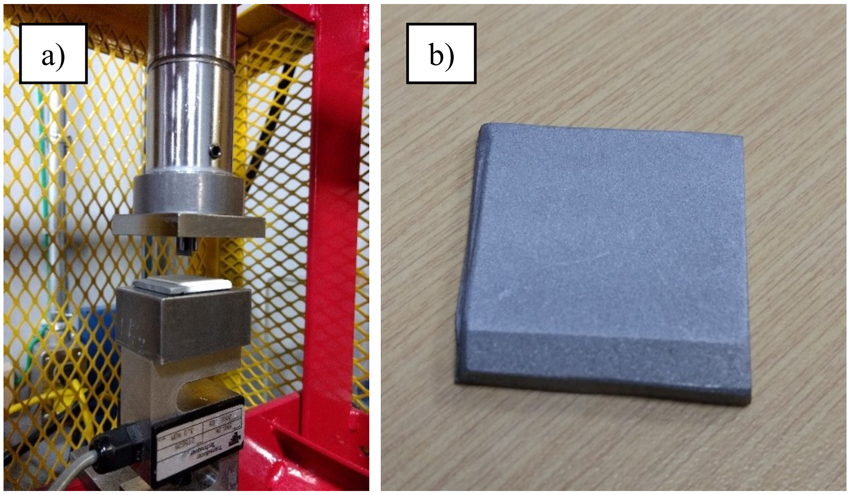

Figure 6.6 Indentation test rig (a) – see Section 5.5.2 – and APS hBN sample (b) before tests

6.2.2 High-temperature tests

Because conditions in the ICT are far from those in the room-temperature, low-load test above, a second round of friction tests was done to validate that a significant difference in behaviour could be measured under significant frictional forces. Thus, a heating test rig was designed to fit in a UTM, as shown in Figure 6.8. Silicon nitride specimens are rectangular Kyocera SN235P blocks, machined and ground by Kyocera. The specimens are prepared with white-on-black rattle can paint speckling for DIC. The specimens are shown in Figure 6.7. The test sequence is described below.

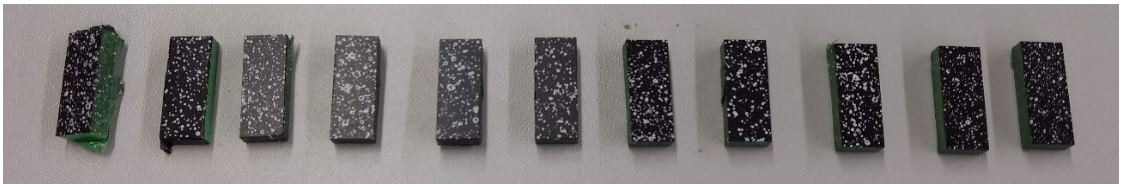

Figure 6.7 Si3N4 specimens prepared with white-on-black speckle pattern for DIC

a) Align the test rig and the UTM crosshead using the alignment jig (see Figure 6.9).
b) Set the first interface plate on the lower heating puck, then install the silicon nitride specimen with the specimen placement jig (see Figure 6.10), then stack the second interface plate and heating puck on the specimen.

c) Install the insulation box and fill it with alumina wool, taking care not to block the borosilicate lighting windows and viewing window.

d) Preload the specimen at a rate of 250 N/s. Compressive preload minimum value is 20 kN, increased by 10 kN increments when judged adequate, according to interface performance and limited number of test specimens. Capture preload phase with DIC at 1 Hz and UTM load cell at 10 Hz. Table 6.2 shows the conversion of UTM force to average contact pressure.

e) Once the final preload is achieved, start the thermal ramp. Capture heating phase with DIC at 1Hz and heating puck thermocouples. UTM is set at constant force and crosshead position automatically adjusts for test rig thermal expansion.

f) Once one or more failures are achieved, or infrared noise becomes too prominent, stop test and cool rig down for safe manipulation.

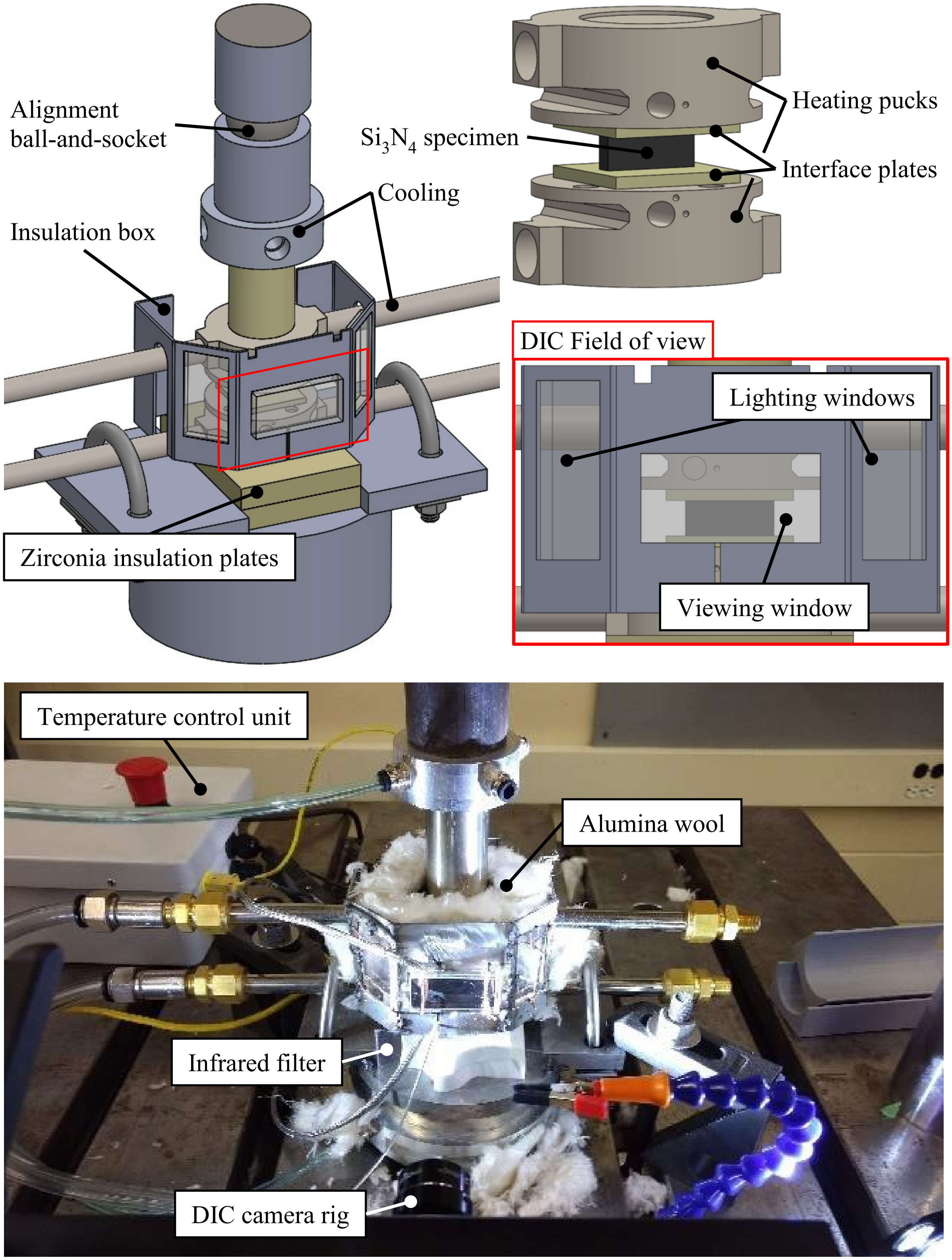

Figure 6.8 Thermomechanical press CAD and component views (top) and actual rig in UTM (bottom)

Table 6.2 Compressive force to average contact pressure conversion chart.

Compressive preload force	Theoretical average contact pressure
20 kN	160 MPa
30 kN	240 MPa
40 kN	320 MPa
50 kN	400 MPa
60 kN	480 MPa

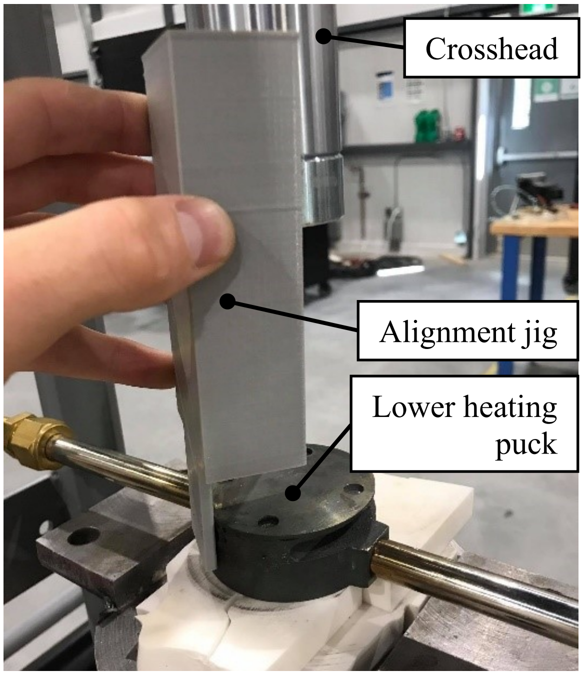

Figure 6.9 Test rig alignment jig

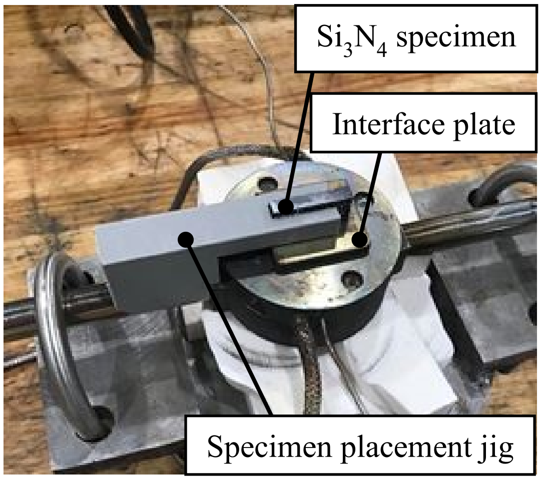

Figure 6.10 Ceramic specimen placement jig

Finally, a manufacturing test was done to validate whether both materials could be combined, and a thin layer of around 100 µm of APS hBN was applied to TBC, shown in Figure 6.11. This was not tested mechanically, but it serves as a proof of concept for a multilayer coating which could reduce thermal expansion mismatch and frictional stress at the interface between the blade tips and the structural shroud.

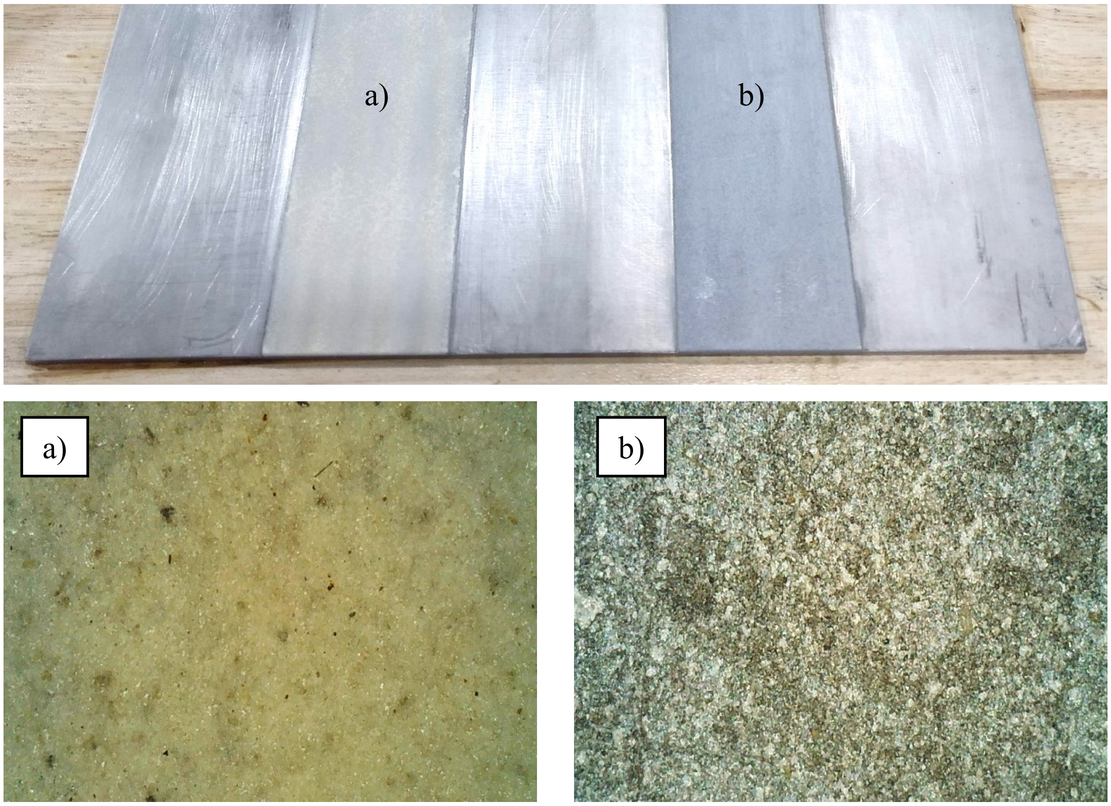

Figure 6.11 a) TBC and b) TBC coated with 100 µm APS hBN; bottom pictures are optical microscopy

6.3 Results and Discussion

Results indicate that hBN gives a significant advantage to reduce ceramic stress levels. A hBN coating reduces coefficient of friction and reduces stick-slip behaviour, when compared to ceramic on bare Inconel or TBC.

6.3.1 Ambient test results

The ASTM-inspired coefficient of friction test curves are all shown in Figure 6.12. All three runs are shown for each specimen, to illustrate the excellent repeatability between runs. Both μ_s

and μ_k are shown on Figure 6.12, where μ_s is the maximum value at the beginning of the test run – if different from the rest of the run – and μ_k is the average μ value of all 3 runs, over the 8 seconds preceding the end of the runs.

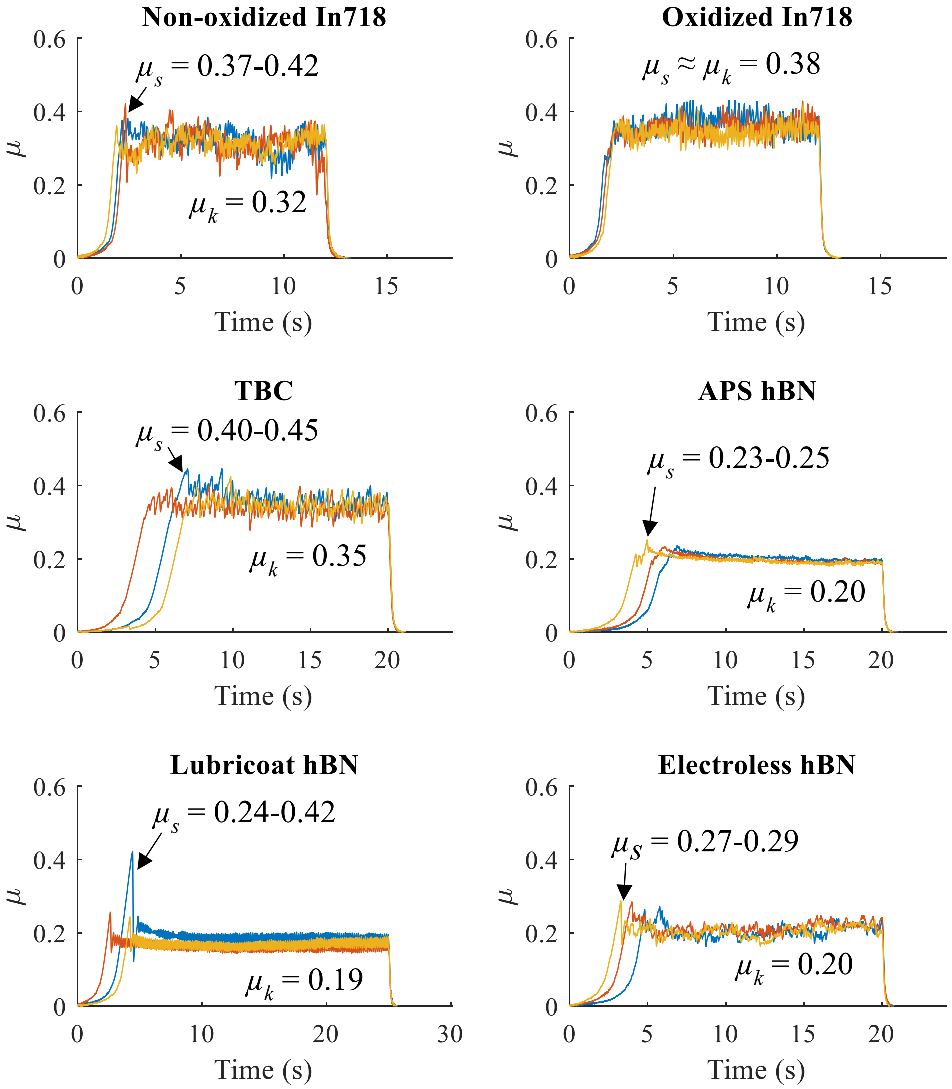

Figure 6.12 Coefficient of friction μ for RT friction tests

The effect of hBN is significant and reduces μ_s by 31 % and μ_k by 44 %, when compared to average values of In718 and TBC specimens. Stick-slip, i.e. rapid oscillation between a static and kinetic friction mode, is prevalent in the In718 and TBC specimens. Stick-slip also occurs at a lesser extent in the Lubricoat and Electroless versions of the hBN coating with Lubricoat showing a run where severe sticking occurred before sliding. The APS version shows the smoothest glide, with the smallest difference between μ_s and μ_k and the lowest stick-slip oscillation amplitude.

A low μ_s value is desirable. Moreover, a low difference between μ_s and μ_k is desirable to the interface designer, as it decreases the amplitude of force oscillation during stick-slip and on a more practical note, it decreases the uncertainty as to which coefficient of friction value to use while modelling.

Indentation tests showed that under relatively light load, hBN sticks to the indenter. As shown in Figure 6.13, marks are visible where hBN was removed from the substrate as early as 200 MPa. At 400 MPa, hBN was removed along the entire indenter, not just at the trailing edge. This indicates that adhesion between the substrate and APS hBN is much poorer than TBC. This may also indicate a propensity for lubricant depletion between the indenter and the substrate, although it remains unknown what the minimal hBN layer thickness is and whether it remains trapped between the assembled bodies or not.

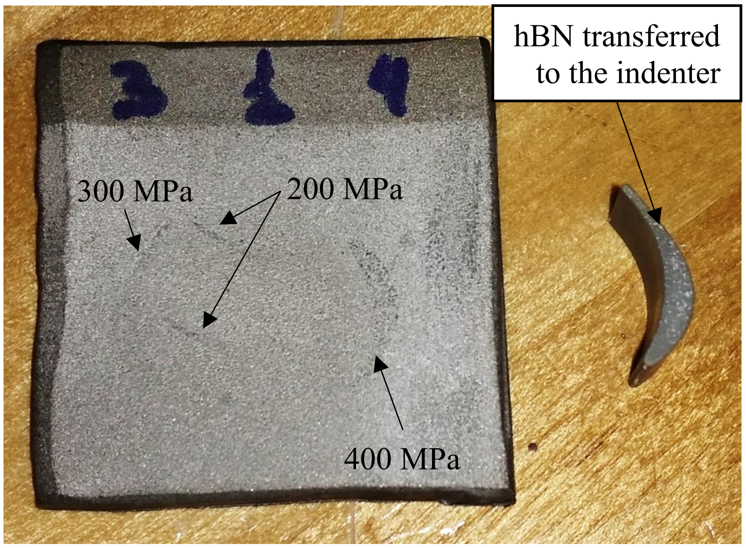

Figure 6.13 Macro-indentation tests done on APS hBN

6.3.2 Thermomechanical test results

Figure 6.14 shows specimen segments after failure on a typical test run in the high load, high temperature test rig. Specimen segments were manually spaced far apart to show the direction of failure, i.e., normal to the thermal strain direction. Actual displacement between segments during a test run is not as extreme and is visible in DIC data.

Figure 6.14 Failed specimen segments in test rig after test run; broken segments are purposely spaced further apart to show failure

The interface sheet metal pads after a test are shown in Figure 6.15. Friction leaves visible marks on all interfaces. The most dramatic appearance change is on hBN. The initially grey coating (see Figure 6.2, Figure 6.13) whitens after high-temperature operation, and remains grey in the test region. SEM imagery shows that although there seems to be hBN depletion at the interface, there is still a significant amount of hBN left at the interface and no Inconel can be seen through it. Figure 6.16 shows the hBN splat macrostructure (thought to be due to plasma spray application) which aligns with the frictional stress direction. This explains the low coefficient of friction of hBN at this high-pressure interface.

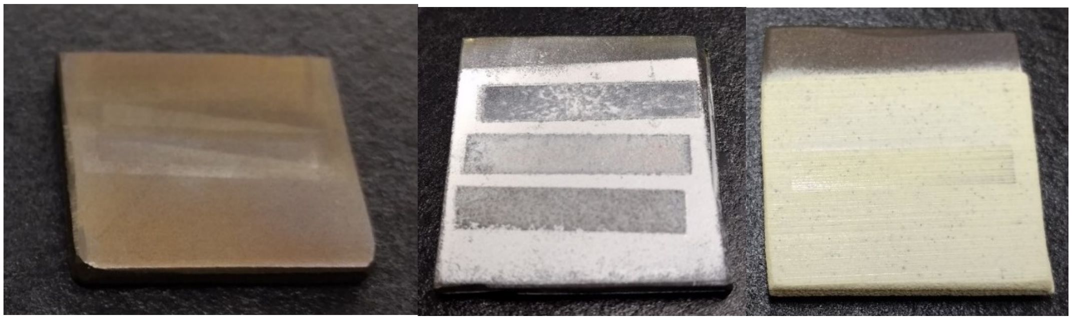

Figure 6.15 Inconel (left), hBN (center) and TBC (right) interface sheet metal pads after test runs.

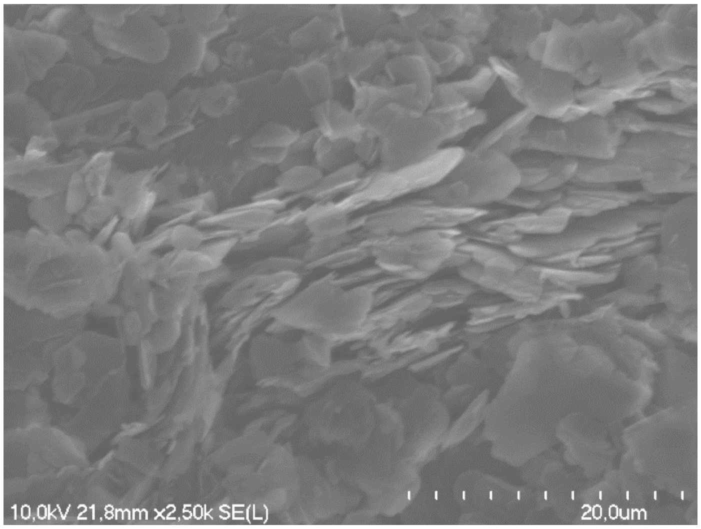

Figure 6.16 hBN platelets aligned by frictional stress at the interface with ceramic specimen.

TBC has a dark, scratch-like appearance, shown in the closeup in Figure 6.17.

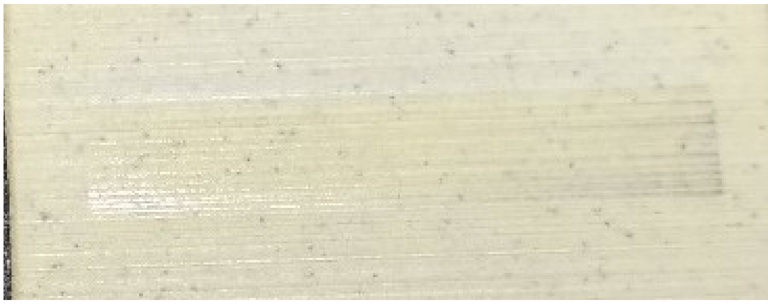

Figure 6.17 TBC friction marks after test run.

It was hypothesized that there may have been silicon nitride transferred to the TBC. However, using EDS, it was shown that the darker appearance is cosmetic and has the chemical composition of the TBC top coat (8YSZ).

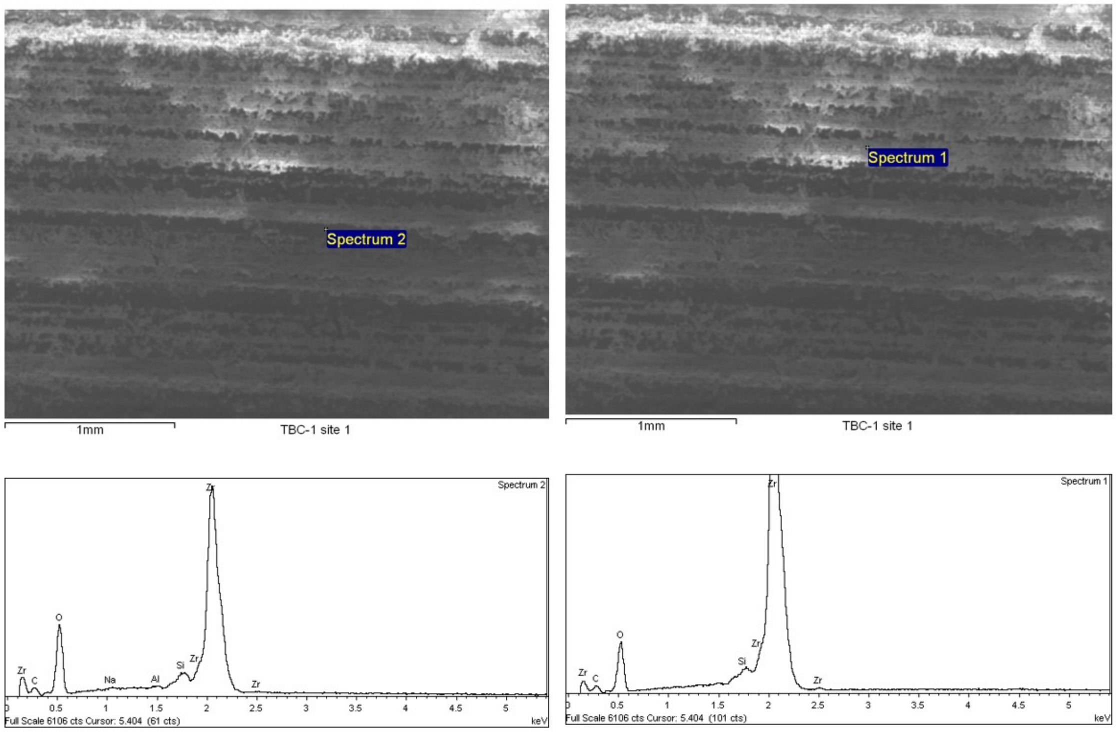

Figure 6.18 EDS results for dark scratches (left) on TBC surface indicate that there is no significant difference in chemical composition with paler benchmark (right).

DIC results must be post-treated for relevant data visualization. Figure 6.19 shows a map of displacement *u* measured in the specimen's longitudinal *x* axis by the DIC system. Origin is the lower left point of the DIC interpolated grid. This map is generated for each DIC picture. Sudden changes in colour correspond to specimen fractures. Cracks are in the *y* direction, indicating that failure is indeed caused by normal stress in the *x*-direction, induced by shear at the interface.

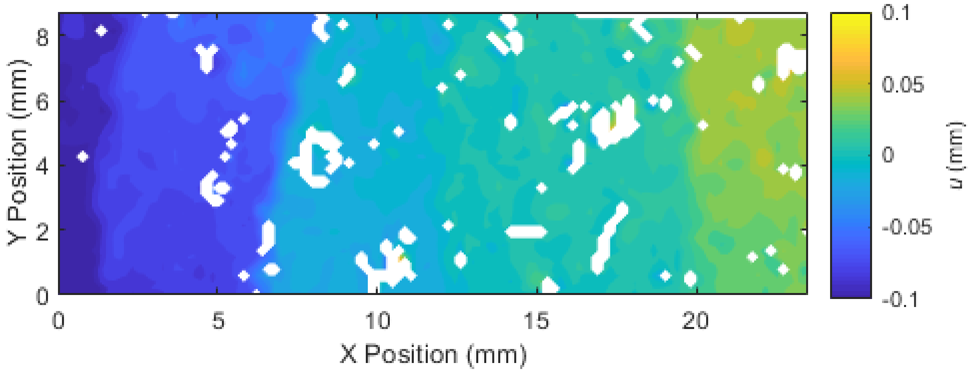

Figure 6.19 DIC map of *x*-axis displacement *u* at a given temperature point during thermal loading

The variation in total length of the specimen is tracked and converted into total strain ε_{tot}. Theoretical SN235P thermal expansion of the specimen, ε_T, is subtracted from the total strain, to obtain the mechanical, friction-induced strain ε_m, as shown in Eq (6.2).

$$\varepsilon_{tot} = \frac{\Delta L}{L_i} = \varepsilon_m + \varepsilon_{th} \tag{6.2}$$

ε_m is plotted in Figure 6.20, for a preload force of 20 kN. Sudden jumps in strain value correspond to the ceramic specimen splitting and the return of the frictional interface to a lower-stress state. Once split, the broken-off segments generally follow the relative thermal expansion of Inconel, indicating that the interface has gripped the specimen segment, pulling it away from the other segment. The full post-treatment process is detailed in Appendix B.

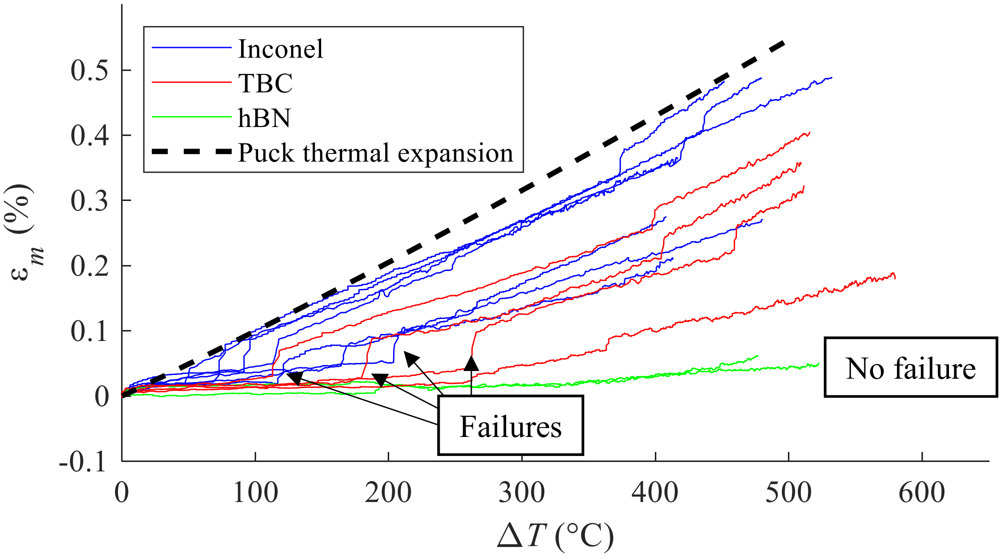

Figure 6.20 Overall mechanical strain of the specimens coloured according to interface type, at 20-kN preload; failures are visible as a jump in interpolated strain

Figure 6.20 shows two different result families: specimens that fail (Inconel and TBC curves) and specimens that do not fail (hBN curves). The absence of jumps in hBN curves signifies that the specimens slipped throughout thermal loading. The Inconel and TBC interfaces, on the other hand, have similar behaviours, though TBC breaks the specimen at a higher temperature. This could be due to fundamentally lower coefficient of friction or to surface effects of the TBC, which may offer less shear resistance to the ceramic specimen, as it has relatively compliant in-plane properties, as found in Section 5.6.1. TBC thermal resistance was evaluated in a transient

FE thermal simulation at the same heating rate as tests, and it was found to have negligible effects on component temperature difference results.

Preload was varied during the tests, and the effects of increasing preload are shown in Figure 6.21. The spread of ΔT achieved before failure at a given preload is quite large, thought to be due to preload center-of-force inconsistency, as well as variability in ceramic specimen strength.

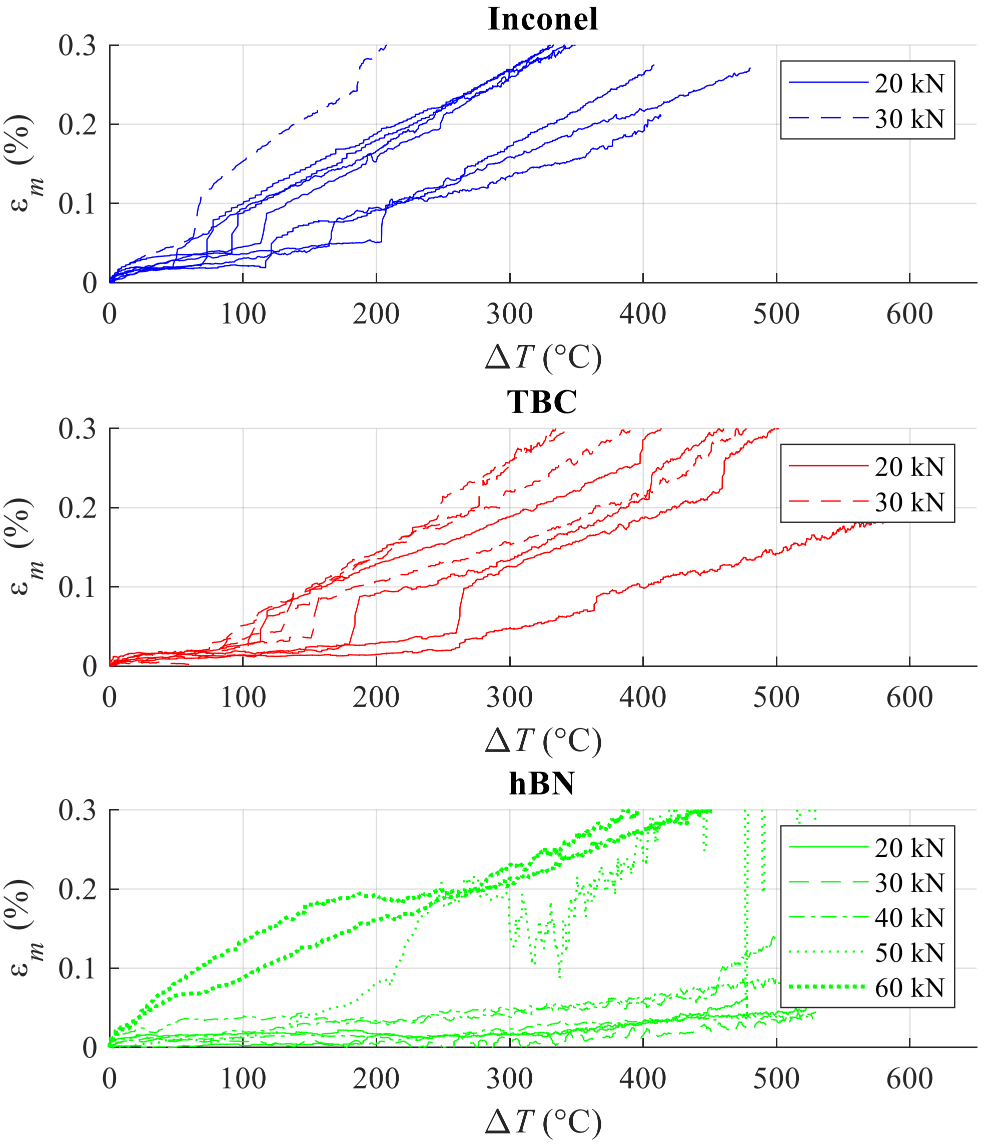

Figure 6.21 Overall mechanical strain of the specimens according to interface type and maximum preload force.

In Figure 6.21, it is quite clear that hBN holds a significant advantage over the other two interface types. From 20 to 40 kN, the specimen strain is practically constant. The extreme preload values (50 kN and 60 kN) cause early failure in the hBN-coated interface test runs. The greatest advantage brought by hBN is the long-lasting slip regime it provides. Although TBC and Inconel interfaces slip early on, the specimen is gripped quite quickly ($\Delta T = 100$-200 °C for Inconel, $\Delta T = 200$-250 °C for TBC, at 20 kN preload), which causes it to fail instantly. hBN remains in the slip regime throughout the thermal loading, except at high force preload. This is consistent with the findings in room-temperature ASTM tests, where it was found that Inconel and TBC offered a stick-slip type of behaviour, whereas plasma-sprayed hBN offered a smooth kinetic (slipping) regime, with no return to a static (sticking) state. Microslik and Lubricoat did not offer quite as smooth a glide as APS, which could mean that they are not as viable candidates as APS.

6.4 Conclusions

At room temperature, low load conditions, hBN improves static coefficient of friction μ_s by 31 % and kinetic coefficient of friction μ_k by roughly 43 %, when compared to silicon nitride on TBC or Inconel 718. Several application methods were employed and tested at room temperature, and all performed well, with APS eliminating stick-slip behaviour completely and Lubricoat having the most dramatic effect on μ. Microslik did not perform quite as well. APS hBN does not adhere fully to its substrate, and adhered to the indenter under an average compressive load of 200 MPa. However, scanning electron microscopy reveals that hBN platelets are still present over the entire contact face despite visual inspection leading to think otherwise.

hBN has a significant impact on thermally induced friction at the interface between low-CTE ceramic and high-CTE Inconel 718 alloy. Only a thin layer of hBN macrostructure is required to reduce friction, and it is resistant to extreme force and shear strain. Non-lubricated interfaces, i.e., TBC and Inconel 718, grip the silicon nitride during expansion and break them, whereas comparable test conditions lubricated with APS hBN did not fail. TBC, which has a similar CTE to Inconel 718 and similar coefficient of friction, yields slightly better results than Inconel 718, although it does not by itself significantly reduce stress levels in the adjacent ceramic body.

Furthermore, APS hBN offers a smooth kinetic, or slipping, regime, which appears to prevent the interface from returning to a static, or sticking, state under high load. No Lubricoat or Microslik were tested under high-load and high-temperature, however, so the sensitivity to stick-slip amplitude is unknown.

CHAPTER 7

CONCLUSIONS

English conclusions below.

La question de recherche pour cette thèse était : **Quelle est la meilleure approche pour réduire les contraintes en tension dans les pales de rotor de turbine ICT?**

7.1 Résumé

La motivation derrière le travail présenté dans cette thèse est d'améliorer la fiabilité des pales de rotor ICT, afin de contribuer à amener au marché ce nouveau paradigme de rotor. La fiabilité est un élément vital dans les turbomachines dans toutes leurs applications. Donc, la réduction des sources de défaillance dans la céramique du rotor ICT est tout aussi vitale. Le travail de cette thèse est découpé en trois parties et leur chapitre correspondant : observation et analyse des résultats numériques et expérimentaux dans les conceptions de rotor existantes au chapitre 3 ; enquête sur les causes physiques principales des problèmes de fiabilité au chapitre 4 ; évaluation expérimentale des solutions potentielles aux chapitres 5 et 6.

Dans le chapitre 3, un résumé des investigations expérimentales et numériques de deux conceptions de rotor ICT a soulevé la question du frottement à l'interface de la pale et des composants de support. Deux conceptions de rotor ont été comparées numériquement et expérimentalement, ce qui a conduit à un ensemble de résultats clés :

- L'analyse numérique indique que le contact de la pale avec les composants métalliques de support entraîne un champ de contrainte en tension dominant. Les travaux expérimentaux corroborent cela, puisque la conception avec deux interfaces fortement sollicitées a subi une défaillance alors que la conception qui libère le pied de pale a opéré avec succès.

- Il s'ensuit que la conception avec la pale coulissante sur plan incliné est supérieure en termes de fiabilité de la pale. La conception à pale pincée a une base de pale très sollicitée mécaniquement, ce qui serait fondamentalement difficile à améliorer.

Les résultats indiquent qu'il est possible de construire des rotors ICT plus durables selon la conception à pales coulissantes. Les résultats indiquent également qu'une réduction du frottement à l'interface pourrait réduire le champ de contraintes en tension à des niveaux acceptables.

Le chapitre 4 couvre l'étude numérique des phénomènes physiques dominants à l'interface restante et essentielle de la pale, c'est-à-dire entre le bout de la pale en céramique et le carénage structurel du rotor. Une approche de conception d'expériences (DOE) a été utilisée avec une géométrie CAO simplifiée en FEA, avec un espacement d'hypercube latin sur les principales variables identifiées. Les données ont été traitées avec un réseau de neurones avec validation aléatoire, avec un $R^2 > 0.95$, suffisant pour la précision recherchée, compte tenu des simplifications apportées. L'analyse de sensibilité du réseau de neurones a mis en évidence ces principaux résultats :

- Le coefficient de frottement μ est en effet la variable la plus importante. Il a un impact sur les autres phénomènes physiques, quelle que soit leur direction. Une technologie de réduction de friction doit être intégrée à l'interface pale-carénage. Pour être clair, il ne s’agit pas de friction haute vitesse du type observé dans une turbine classique, mais de friction microscopique entre des composantes en contact à haute pression, tournant à la même vitesse.
- La déformation tangentielle et la dilatation thermique ont une contribution similaire, la première étant principalement entraînée par la vitesse de rotation et la seconde par le gradient de température et la sélection des matériaux. Étant donné que la vitesse de rotation a des contraintes de conception aérodynamiques, la réduction de la dilatation thermique est considérée comme un objectif plus accessible.

Ainsi, la lubrification pourrait être utilisée, comme suggéré au chapitre 3, pour réduire la friction à haute force normale entre les pales en céramique et le carénage structurel métallique en rotation. La barrière thermique, déjà envisagée pour réduire les besoins en refroidissement dans le carénage, pourrait également servir d'élément de contrôle de la dilatation thermique. Le nitrure de bore hexagonal (hBN) et le revêtement de barrière thermique à base de zircone (TBC) sont proposés comme solutions potentielles aux problèmes soulevés dans l'investigation numérique.

Les chapitres 5 et 6 rapportent l'étude expérimentale qui a été réalisée comme étapes préliminaires pour incorporer le TBC et le hBN dans un rotor ICT. Compte tenu des propriétés non linéaires et orthotropes des deux matériaux, la validation expérimentale a été considérée comme la méthode appropriée.

- Des éprouvettes de TBC en zircone stabilisée à l'yttria (YSZ) projetées par plasma à l'air (APS) ont été soumises à des essais de traction statique et des essais d'indentation, qui ont validé que l'orthotropie théorique était suffisante pour les chargements dans le carénage structurel.
- Du TBC a été appliqué au carénage structurel d'un prototype ICT et a démontré qu'il peut résister aux conditions de fonctionnement réelles des ICT.
- Les méthodes d'application à l'aérosol, au placage autocatalytique ainsi que l'application APS de hBN ont été testées pour évaluer leur coefficient de frottement. Le coefficient de frottement statique μ_s a été réduit de 31 % et le coefficient de frottement cinétique μ_k a été réduit de 44 %. L'APS a montré les valeurs de coefficient de frottement les plus faibles et les plus lisses et sans à-coups (*stick-slip*), ce qui conduit à conclure qu'il s'agit du meilleur candidat pour des rotors résilients.
- Le hBN appliqué par APS a été testé sous chargement élevé dans une configuration à dilatation thermique forcée. Sous une charge similaire et en tenant compte des limitations du banc d'essai, le hBN APS montre une augmentation d'au moins 100 % de l'expansion admissible, car les spécimens de test n'ont pas craqué avec cette interface alors qu'elles l'ont fait sur l'Inconel 718 sans revêtement et sur le TBC.

Cela indique que le TBC doit être conçu non seulement pour réduire le flux de refroidissement, mais également pour contrôler la dilatation thermique et réduire les contraintes en bout de pale. Bien que le hBN n'ait pas été testé directement dans un rotor ICT, ses excellentes performances en tant que lubrifiant à charge élevée et à haute température indiquent qu'il devrait être incorporé dans les futurs rotors ICT. De plus, il a été appliqué avec succès sur du TBC, ce qui indique que les deux revêtements sont compatibles et peuvent être appliqués sur la face interne du carénage structurel.

La réponse pratique à la question de recherche est donc : **Inclure la différence de dilatation thermique entre le bout de pale et l’anneau de refroidissement dans les critères de sélection de l'épaisseur du TBC, et ajouter un revêtement hBN APS pour lubrifier l'interface afin de réduire la sensibilité à la déformation tangentielle.**

7.2 Contributions

La thèse met en avant les contributions originales suivantes.

1. **Identifier l'interface de friction comme un problème de fiabilité dans les pales de rotor ICT.** L'interface entre le bout de pale et le carénage structurel est spécifique à la configuration renversée. On estime que quelle que soit la façon dont la pale est liée au carénage, il y aura un problème de friction entre matériaux hétérogènes qui induira des contraintes en tension dans les pales en céramique. Passer d'une conception à pale pincée à une conception à pale coulissante sur plan de glissement réduit la problématique à une interface au niveau du bout de pale, ce qui s'avère être un avantage significatif pour cette conception.
2. **Identifier et quantifier les contributions des principales variables à l'état de contrainte en bout de pale.** L'interface est sujette à plus d'un mécanisme de déformation. La déformation tangentielle, l'écart de dilatation thermique et le coefficient de frottement ont été identifiés comme les principales variables de conception à réduire. La déformation tangentielle peut être réduite en réduisant le poids apparent du carénage, par exemple en utilisant du titane pour le système de refroidissement, ou en réduisant la vitesse de rotation. L'écart de dilatation thermique peut être réduit grâce au TBC qui réduit la dilatation thermique du carénage. Le coefficient de frottement peut être réduit en utilisant un revêtement lubrifiant à haute température tel que le hBN, à l'interface.
3. **Étudier expérimentalement les revêtements TBC et hBN comme solutions potentielles.** Des tests en laboratoire ont validé la résistance des deux revêtements à une force normale élevée et à un fonctionnement à haute température. Le TBC a été validé dans un rotor ICT et est déjà intégré dans le processus de conception. Le hBN n'était pas

encore intégré dans le rotor, bien qu'il ait montré une réduction de 44 % du coefficient de frottement cinétique et une augmentation d'au moins 100 % de l'écart de déformation admissible. Les deux revêtements sont compatibles et le hBN peut être appliqué sur le TBC, créant ainsi un revêtement bifonctionnel qui pourra être appliqué sur la face interne du carénage structurel, en bout de pale.

7.3 Travaux futurs

Les solutions pratiques proposées dans cette thèse, c'est-à-dire les revêtements TBC et hBN, ont leurs propres domaines de recherche associés, et seule la surface a été effleurée dans ce travail. Dans le travail présenté dans cette thèse, l'investigation numérique et la validation expérimentale utilisent des modes de défaillance catastrophiques à court terme. Cependant, d'autres modes de défaillance existent et doivent également être étudiés. Par exemple, le TBC a tendance à s'écailler en raison de la croissance d'oxyde dans la couche de liaison. Cela se produit après une exposition à long terme à des températures élevées. Il demeure inconnu si un contact à long terme avec des céramiques à base de silicium pourrait également induire ce type de problème, ou éventuellement l'inhiber.

Comme mentionné ci-dessus, le hBN n'a pas été testé dans un rotor ICT. C'est la dernière étape de validation expérimentale qui doit être franchie. Il peut être appliqué sur du TBC, bien qu'il faille valider si la préparation de surface, c'est-à-dire le meulage du TBC au diamètre interne final, peut être effectuée et tout de même garantir une bonne adhérence au hBN et si des étapes de fabrication supplémentaires sont nécessaires, ce qui pourrait devenir trop coûteux. Si tel est le cas, d'autres méthodes d'application de hBN pourraient être étudiées, bien qu'il reste tout à fait clair que l'APS offre la combinaison la plus faible de μ_s et μ_k. Il convient également de valider que le hBN peut supporter la proximité avec le flux de gaz chauds. Parce qu'il est coincé entre la pale et le carénage sous une force élevée, cela ne devrait pas être critique.

Les limites de lubrification du hBN n'ont pas été clairement identifiées dans le banc d'essai à haute température, car la lecture de la température maximale était limitée par la pollution lumineuse infrarouge. De plus, la charge de compression était limitée par l'alignement du banc d'essai et les valeurs élevées n'étaient pas considérée comme représentatives des forces centrifuges de volume en jeu dans les rotors ICT. L'identification d'une limite claire des conditions de lubrification du hBN serait pertinente pour déterminer quelles enveloppes d’opération et de conception sont disponibles pour les rotors ICT.

Enfin, les tests hBN ont été exécutés sur des éléments de test rectangulaires, plats et réguliers. L'investigation numérique du chapitre 4 a également utilisé une forme de corps de pale simplifiée. Les profils aérodynamiques ont des formes très variables et différents centres de force, ce qui pourrait être critique dans l’évaluation de champs de contraintes en tension réels. Une analyse de sensibilité à la force normale locale pourrait être utile au concepteur, en tant qu'indicateur de la taille ou du rayon minimal de l'élément, par exemple.

English conclusions

The research question for this thesis was: **What is the best approach to reducing tensile stresses in ICT rotor blades?**

7.4 Summary (English)

The motivation behind the work presented in this thesis is to improve reliability in ICT rotor blades, to improve market acceptability of this new rotor paradigm. Reliability is a vital element in turbomachinery throughout their applications, thus reducing sources of failure in the ICT rotor ceramics is equally vital. The work in this thesis is cut into three parts: observation and analysis of numerical and experimental results in the existing rotor designs in Chapter 3; investigation of the physical drivers of reliability issues in Chapter 4; experimental assessment of potential solutions in Chapter 5 and Chapter 6.

In Chapter 3, a summary of experimental and numerical investigations of two ICT rotor designs raised the issue of friction at the interface of the blade and the supporting components. Two rotor designs were compared numerically and experimentally, leading to a set of key findings:

- Numerical analysis indicates that the blade contact with supporting metallic components results in the dominant tensile stress field. Experimental work corroborates this, as the design with two highly stressed interfaces failed whereas the design which frees up the blade base did not fail.

- It follows that the design with the sliding blade is superior in terms of blade reliability. The clamped-blade design has a very stressed blade base, which would be fundamentally difficult to improve.

Results indicate that it is possible to build longer-lasting ICT rotors according to the sliding-blade design. Results also indicate that a reduction in friction at the interface could reduce the tensile field to acceptable levels.

Chapter 4 covers the numerical investigation of the physical phenomena at the remaining, essential blade interface, i.e., the ceramic blade tip to the rotor's structural shroud. A design of experiments approach was used with a simplified CAD geometry in FEA, with Latin hypercube spacing over the main identified variables. Data was processed with a neural network with random holdback validation, with a $R^2 > 0.95$, sufficient for the precision which was sought, considering the simplifications at hand. The neural network sensitivity analysis pointed to these main findings:

- Coefficient of friction is indeed the single most important variable. It impacts other physical phenomena, regardless of direction. Friction-reducing technology should be incorporated at the blade-to-shroud interface. To be clear, this is not high-speed friction of the type seen in a conventional turbine (tip rub), but microscopic friction between components in contact at high pressure, rotating at the same speed.
- Hoop strain and thermal expansion have similar contribution, the former driven mainly by rotational velocity and the latter by temperature gradient and material selection. Seeing as rotational velocity has aerodynamic design constraints, reducing thermal expansion is seen as a more approachable target.

Thus, lubrication could be used, as suggested in Chapter 3, for reducing friction between the ceramic blades and metallic structural shroud. The thermal barrier, already considered for reducing cooling requirement in the shroud, could also double up as a thermal expansion control item. Hexagonal boron nitride (hBN) and zirconia-based thermal barrier coating (TBC) are proposed as potential solutions to the issues raised in the numerical investigation.

Chapters 5 and 6 report the experimental investigation which was done as preliminary steps to incorporate TBC and hBN in an ICT rotor. Considering the non-linear and orthotropic properties of both materials, physical testing was considered the appropriate method.

- Air plasma sprayed (APS) yttria-stabilized zirconia (YSZ) TBC specimens were submitted to static tensile and indentation tests, which validated that the theoretical orthotropy was sufficient for the loadings in the structural shroud.
- TBC was applied to the structural shroud of an ICT prototype and successfully demonstrated that it can withstand actual ICT operating conditions.
- Aerosol, electroless and APS application methods of hBN were tested for coefficients of friction. Static coefficient of friction μ_s was reduced by 31 % and kinetic coefficient of friction μ_k was reduced by 44 %. APS showed the lowest and smoothest values of coefficient of friction and no stick-slip, which leads to conclude it is the best candidate for resilient rotors.
- APS hBN was tested under high load in a forced thermal expansion setup. Under similar load and accounting for test rig limitations, APS hBN shows at least a 100 % increase in allowable expansion, as the test specimens did not fail with this interface whereas they did on bare Inconel 718 and on TBC.

This indicates that TBC should be designed not only to reduce cooling flow, but also to control thermal expansion and reduce blade tip stresses. Although hBN was not tested directly in an ICT rotor, its excellent performance as a high load, high temperature lubricant indicate it should be incorporated in future ICTs. Furthermore, it was sprayed successfully on TBC, which indicates both are compatible and can be applied to the inner face of the structural shroud.

The practical answer to the research question is thus: **Include thermal expansion mismatch between the blade tip and cooling ring in the design criteria for selecting TBC thickness, and add an APS hBN coating to lubricate the interface with the blade tip to reduce sensitivity to hoop strain.**

7.5 Contributions (English)

The thesis puts forward the following original contributions.

1. **Identify the frictional interface as a reliability issue in ICT blades**. The interface between the blade tip and structural shroud is specific to the inside-out configuration. It is estimated that whatever the way the blade is linked to the shroud, there will be an issue with friction between heterogenous materials which will induce tensile stresses in the ceramic blades. Moving from a clamped blade design to a sliding blade design reduces to one problematic interface at the blade tip, which proves to be a significant advantage of the latter.
2. **Identify and quantify the contributions of the main variables to the stress state at the blade tip**. The interface is prone to more than one deformation mechanism. Hoop strain, thermal expansion mismatch and coefficient of friction were identified as the main design variables to reduce. Hoop strain can be reduced by reducing shroud apparent weight, e.g. using titanium for the carbon-fiber cooling system, or reducing rotational speed. Thermal expansion mismatch can be reduced through TBC which reduces thermal expansion of the shroud. Coefficient of friction can be reduced by using a high-temperature lubricant coating such as hBN at the interface.
3. **Experimentally investigate TBC and hBN coatings as potential solutions to address the issue**. Laboratory tests validated both coatings' resistance to high normal force and high-temperature operation. TBC was validated in an ICT rotor and is already integrated in the design process. hBN was not integrated in the rotor yet, although it did show a reduction of 44 % in dynamic coefficient of friction and at least a 100 % increase in allowable strain mismatch. Both coatings are compatible and hBN can be sprayed onto TBC, thus creating a bi-functional coating which should be applied to the inner face of the structural shroud, at the blade tip.

7.6 Future work (English)

The practical solutions proposed in this thesis, i.e., TBC and hBN coatings, have their own associated research fields, and only the surface was scratched in this work. In the work presented in this thesis, numerical investigation and experimental validation use short-term, catastrophic failure modes. However, other failure modes exist and should be investigated also. For example, TBC is prone to spall due to oxide growth within the bond coat. This occurs after long-term exposure at high temperatures. It is unknown whether long-term contact with silicon-based ceramics could also induce this type of issue, or possibly inhibit it.

As mentioned above, hBN was not tested in an ICT rotor. This is the last experimental validation step which should be taken. It can be coated onto TBC, although it should be validated whether surface preparation, i.e., grinding of the TBC to final internal diameter, can be undergone for proper hBN adhesion and if extra manufacturing steps are required, which could become overly costly. If this is the case, other methods of hBN application could be investigated, although it remains quite clear that APS offers the lowest combination of μ_s and μ_k. It should also be validated that hBN can withstand proximity with the hot gas flow. Because it is trapped between the blade and shroud under high force, this is not expected to be critical.

Lubricating limits of hBN were not clearly identified in the high temperature test rig, as maximum temperature reading was limited by infrared light pollution. Also, high compressive loading was limited by crosshead and test rig alignment and was not believed to be representative of the centrifugal body forces at play in ICT rotors. Identifying a clear limit of lubricating conditions for hBN would be relevant in determining what operating and design envelopes are available for ICT rotors.

Finally, hBN tests were run on rectangular, flat, regular test items. The numerical investigation in Chapter 4 also used a simplified blade body shape. Airfoils have widely varying shapes and different centers-of-force, which could be critical in actual tensile force fields. A sensitivity analysis to local normal force could be valuable to the designer, as an indicator of minimum feature size or radius, as an example.

APPENDIX A

FE MODEL FOR DOE EXPLORATION

This Appendix aims at providing the details for the structural-thermal analysis used in the DOE exploration in Chapter 4. The FE model was cut into three distinct analyses:

1. Thermal distribution considering rim rotor cooling and main flow heat flux, which is affected by blade surface-to-volume ratio and therefore must be simulated for each data point.
2. An unconstrained analysis to compute average radial displacement.
3. A constrained analysis to remove axial bending effects in the rim rotor.

The structural analysis (2 and 3) was twofold, because the bending in the shroud (see Section A.2) causes important 3D effects. This in turn causes the interface shape to change significantly, in a way which is not expected to affect true rotor geometry and which muddles results, making the inference shown in Chapter 4 impossible. Thus it was deemed that a second analysis, which forces a constant radial displacement, would yield results closer to the true stress state. Sections A.2 and A.3 show the details and relation between the two analyses.

The total ANSYS flowchart is illustrated in Figure A.1. Solving was done using 5 cores and each data point took around 2-3 minutes on average, for geometry generation and all 3 simulations to run.

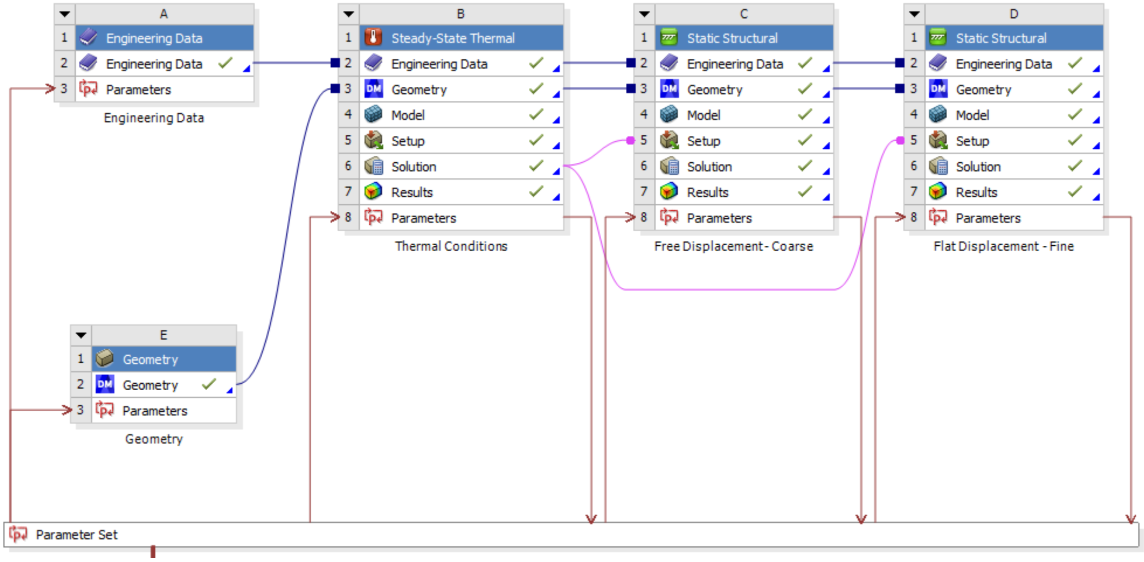

Figure A.1 ANSYS FE flowchart.

The FE model used the geometry described above, with the symmetries shown in Figure A.2.

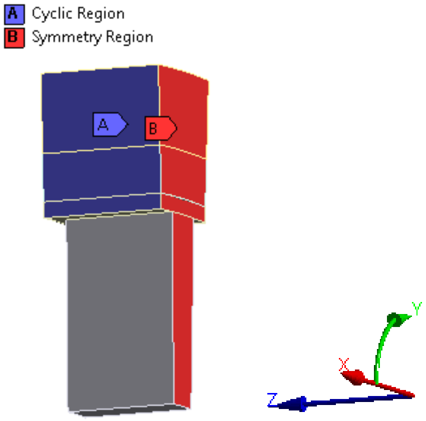

Figure A.2 Geometry symmetries and coordinate system used throughout the FE analyses.

A.1 Thermal analysis

To avoid the complexity of modeling cooling channels, which would involve calculating the best angle and wall thickness for each point, the cooling channels were simply assumed to do their job and ensure a temperature that would not exceed 300 °C at the rim rotor ID. Convection on the blade, although very dependent on fluid conditions and flow passage size, was kept constant at a constant temperature of 1300 °C, with a convection coefficient of 1000 W/m²°C. This is shown in Figure A.3. Notice that the symmetry along the axial direction is shown in the temperature results plot. Furthermore, the bulk of the temperature gradient is achieved within the TBC, which is representative of actual ICT conditions.

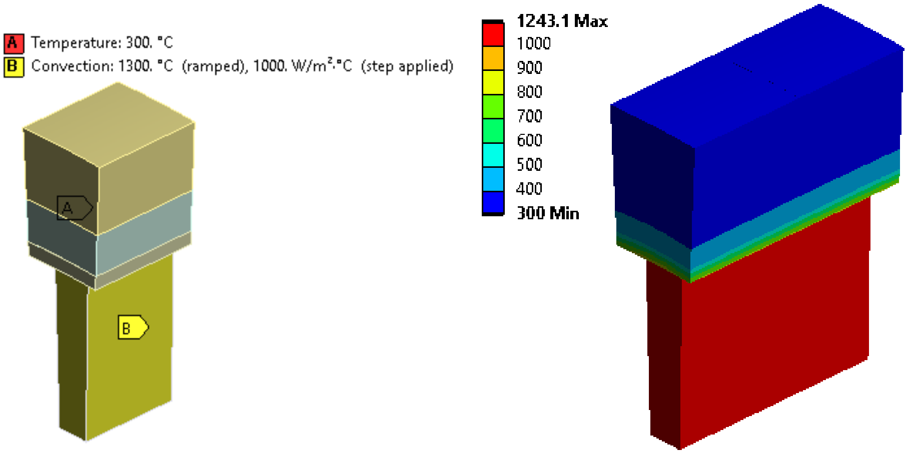

Figure A.3 Thermal FE conditions and results for a given geometry.

A.2 Structural analysis 1: Rim bending

A body under centrifugal load will show a certain amount of bending. As the outer surface is squashed and the extremities of the body are free, rotation occurs at the ends and thus the rim rotor and cooling ring make a banana shape which unloads the blade tip at the extremities, as illustrated in Figures 0 and 1.

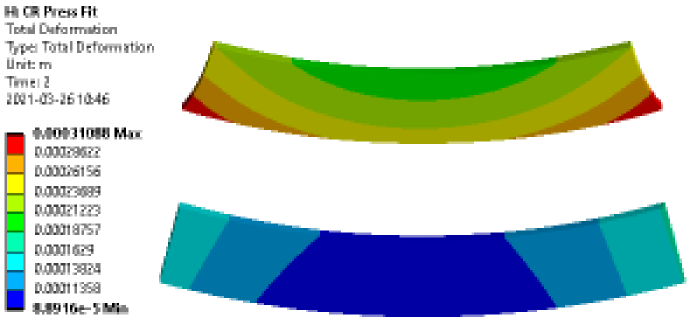

Figure A.4 Shroud-only simulation under centrifugal and thermal loading.

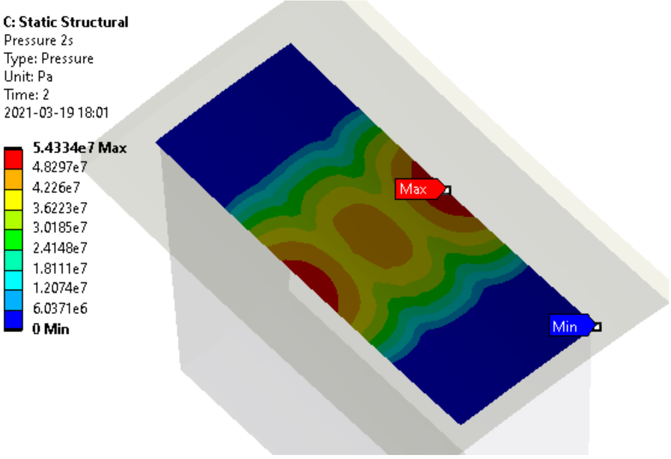

Figure A.5 Interface pressure profile under centrifugal and thermal loading shows that blade leading and trailing edge are unloaded in the simplified geometry.

This occurs in the ICT, however it was found through a few preliminary analyses to be quite sensitive to axial thermal gradient and blade center of mass location. Furthermore, it was found to be a major source of noise in the trends detected by JMP, with R^2 consistently < 0.5. For these reasons, it was deemed best to correct for this effect in the DOE, since the goal of this analysis is to examine the sensibility of the chosen variables.

The solution to this issue was to force the displacement of the shroud to remain flat. This means that a first “free” structural analysis must be run to assess the true displacement. The average rim rotor OD and and cooling ring ID displacements are used as boundary conditions in a second, “constrained” structural analysis (see A.3).

The “free” structural analysis boundary conditions are shown in Figure A.6. Rough contacts are used to speed up the analysis, as frictional stress is not of interest, but unsticking is. Pressure is applied to the blade base at 0 RPM to avoid loss of contact at the start of the analysis. Tangential and axial displacement are blocked in the rim rotor at the symmetry plane, but radial displacement is left free. Mesh size, shown in Figure A.7, is very coarse, as displacement is the output of interest, and stress is not.

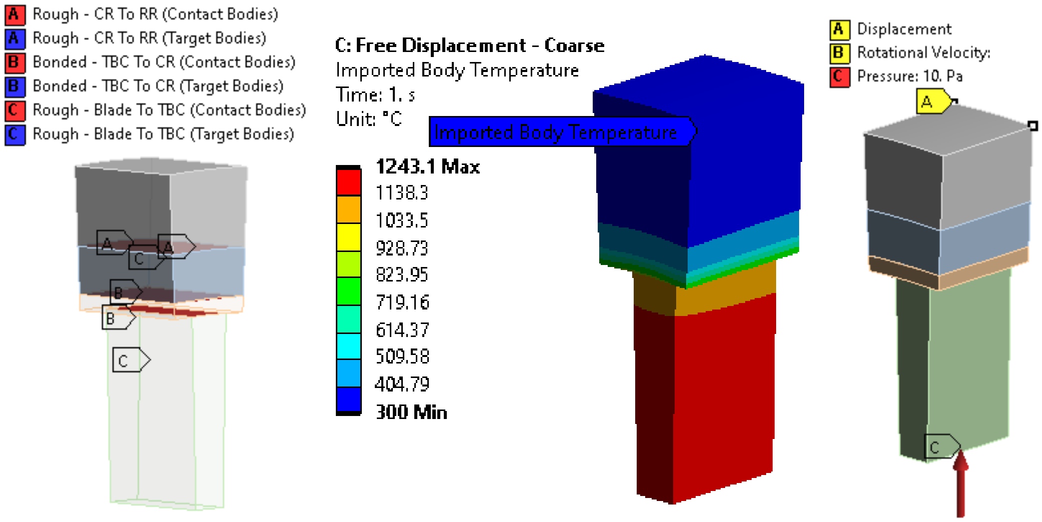

Displacement:

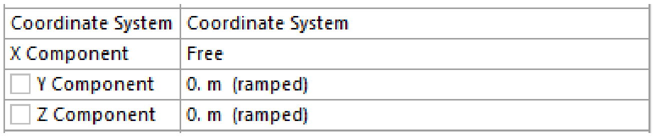

Coordinate System	Coordinate System
X Component	Free
☐ Y Component	0. m (ramped)
☐ Z Component	0. m (ramped)

Rotational Velocity:

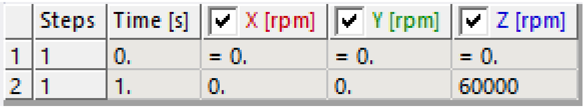

	Steps	Time [s]	☑ X [rpm]	☑ Y [rpm]	☑ Z [rpm]
1	1	0.	= 0.	= 0.	= 0.
2	1	1.	0.	0.	60000

Figure A.6 Boundary conditions in “free” structural analysis.

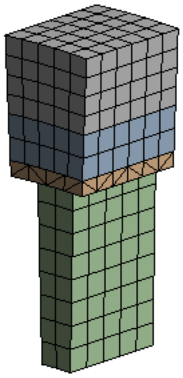

Figure A.7 Mesh size is very coarse in the “free” analysis.

The results of interest are shown in Figure A.8. The pressure profile is not conducive to clear conclusions on design variable trends, thus the radial deformation, shown in Figure A.9, is extracted from the “free” analysis.

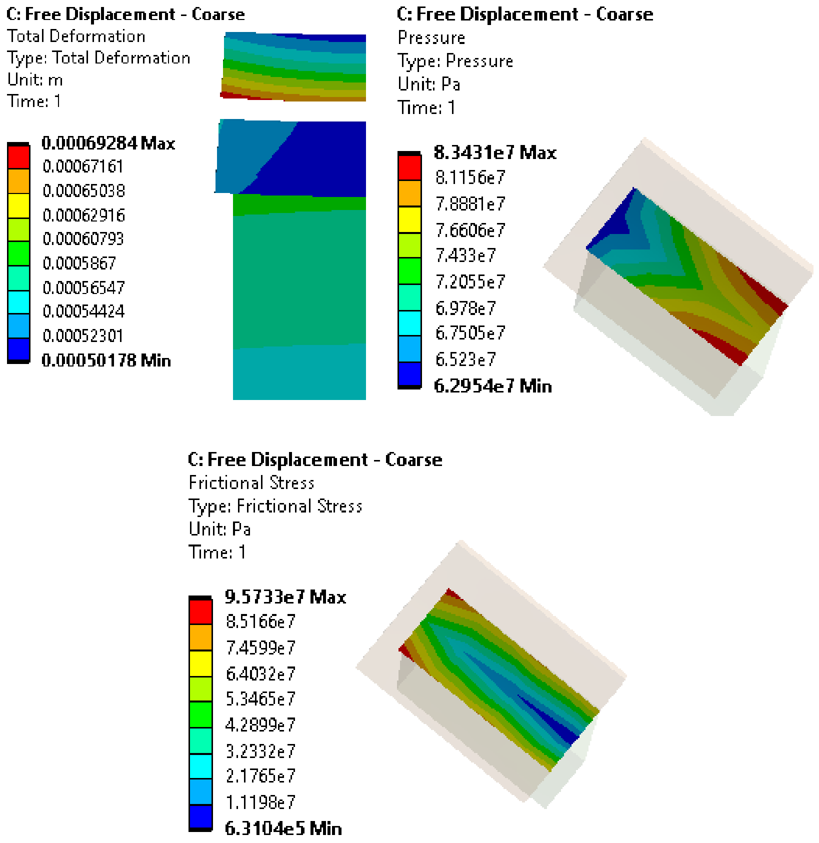

Figure A.8 Shroud bending (left), blade contact pressure profile (center) and interface frictional stress (right) are consistent with findings shown above.

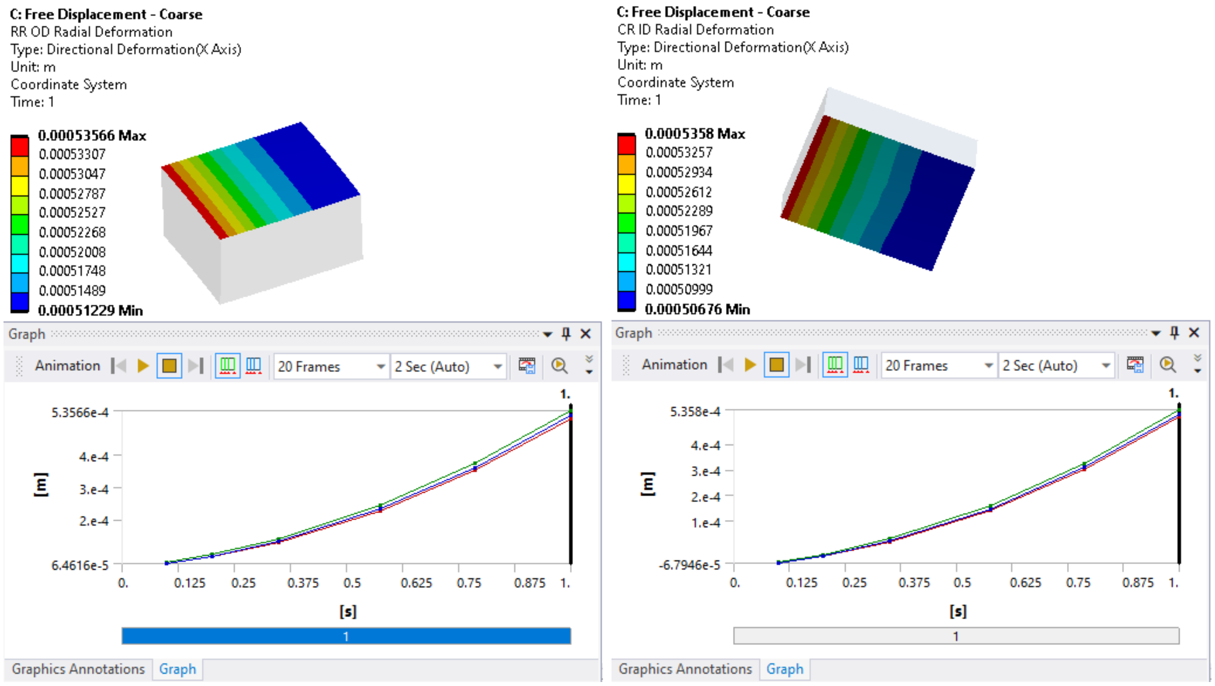

C: Free Displacement - Coarse
RR OD Radial Deformation
Type: Directional Deformation(X Axis)
Unit: m
Coordinate System
Time: 1

C: Free Displacement - Coarse
CR ID Radial Deformation
Type: Directional Deformation(X Axis)
Unit: m
Coordinate System
Time: 1

Figure A.9 Rim rotor OD (left) and cooling ring ID (right) radial displacement plots, along with graphs of minimum (red), average (blue) and maximum (green) radial displacement values throughout analysis.

As shown in Figure A.9, radial displacement follows a x^2 trend as rotational speed is increased in the timestep. The average radial displacement value is quite close to the minimum and maximum values; thus it is used as boundary conditions for the next structural analysis.

A.3 Structural analysis 2: Constrained displacement

This analysis aims at retrieving stress results from the blade and subsequently P_f. Boundary conditions in the "constrained" analysis are identical to the "free" analysis, with additional forced radial displacements at the cooling ring ID and rim rotor OD. This displacement is parameterized to be equal to the displacement calculated in the previous step. Conditions are illustrated in Figure A.10.

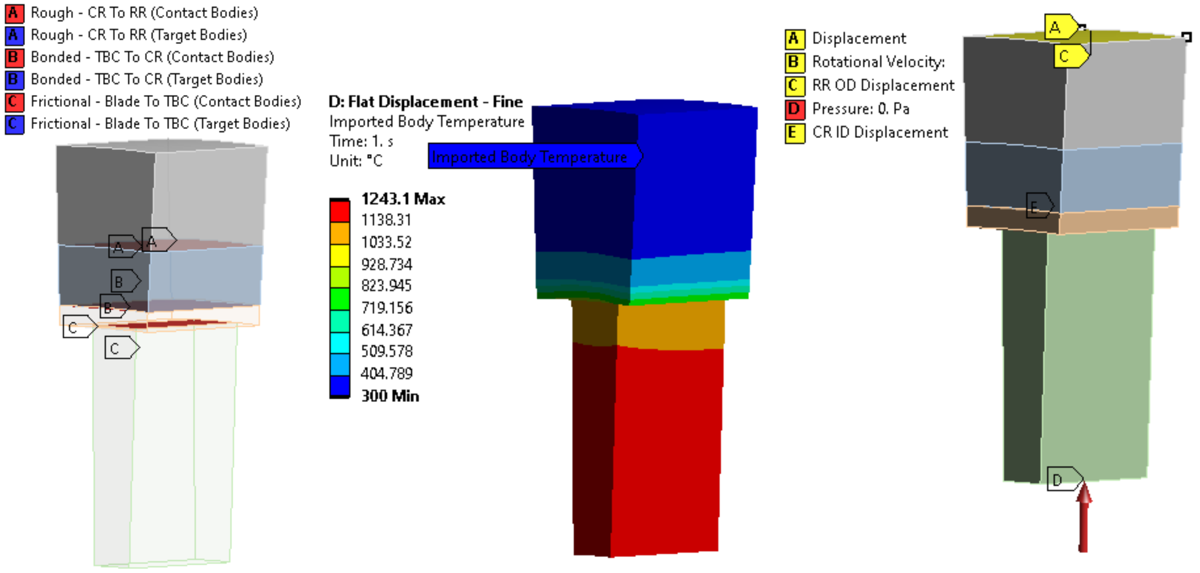

Axial RR Displacement:

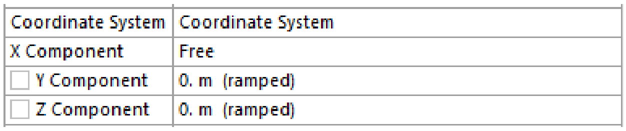

Coordinate System	Coordinate System
X Component	Free
☐ Y Component	0. m (ramped)
☐ Z Component	0. m (ramped)

Rotational Velocity:

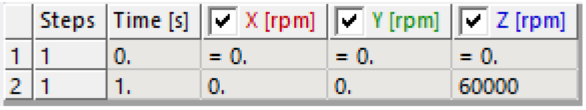

	Steps	Time [s]	☑ X [rpm]	☑ Y [rpm]	☑ Z [rpm]
1	1	0.	= 0.	= 0.	= 0.
2	1	1.	0.	0.	60000

RR and CR radial displacement:

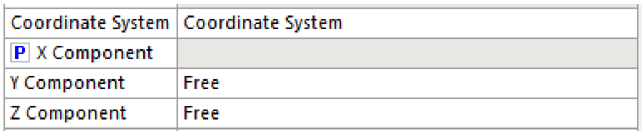

Coordinate System	Coordinate System
P X Component	
Y Component	Free
Z Component	Free

Figure A.10 Boundary conditions in "constrained" structural analysis.

The mesh size is much finer (0.25 mm) at the blade interface than in the "free" analysis. In the past, P_f calculations were found to converge with CARES validation only with a highly refined mesh in the stressed region. Tetrahedral meshing was also found to converge to CARES values better than hex dominant, hence the change in mesh type in the blade. Mesh order is quadratic for higher stress fidelity.

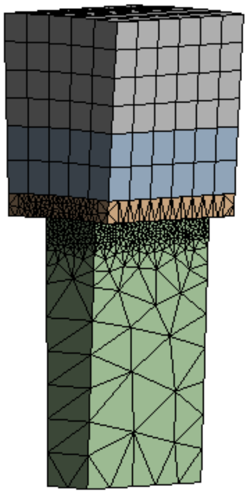

Figure A.11 Mesh size is much finer in the "constrained" analysis, at 0.25 mm.

Results are significantly different to the "free" analysis. The pressure profile, although not completely flat, shows that the blade no longer unsticks from the leading and trailing edge. This allows to visualize the complete effects of friction, especially on long blades which would unstick significantly and add severe non-linearity and mesh-size sensitivity to the analysis. Frictional stress is dominant along the blade edges, seeing as the blade is much stiffer than the TBC and cooling ring, and does not conform to the final deformed shroud radius.

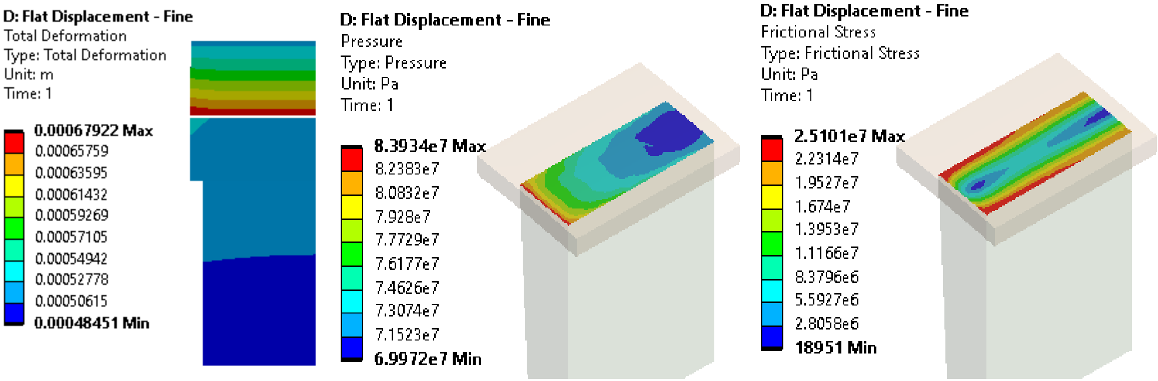

Figure A.12 Forced displacement (left), contact pressure profile (center) and interface frictional stress (right) are quite different from the "free" analysis.

A.4 Data Cleanup

To ensure that the conclusions made from the dataset are robust, the output variables were verified to make sure no obvious error or outliers were contained in the data set.

Two groups of data showed up consistently in all attempts to fit data. This was found to be due to a seemingly random failure of the rough contact between the cooling ring and the rim rotor in ANSYS. The cooling ring's radial displacement largely exceeded the rim rotor's, which indicates that the cooling ring "punched through" the rim rotor in these specific results. No common characteristic was found between the faulty points in the dataset. It is assumed that the normal stiffness at the interface, which ANSYS refreshes at each iteration, was insufficient in these cases. These points are therefore excluded from the result analysis. Further cleaning was done using contact pressure, using Eq. (A.3), to spot outliers, shown in red in Figure A.14.

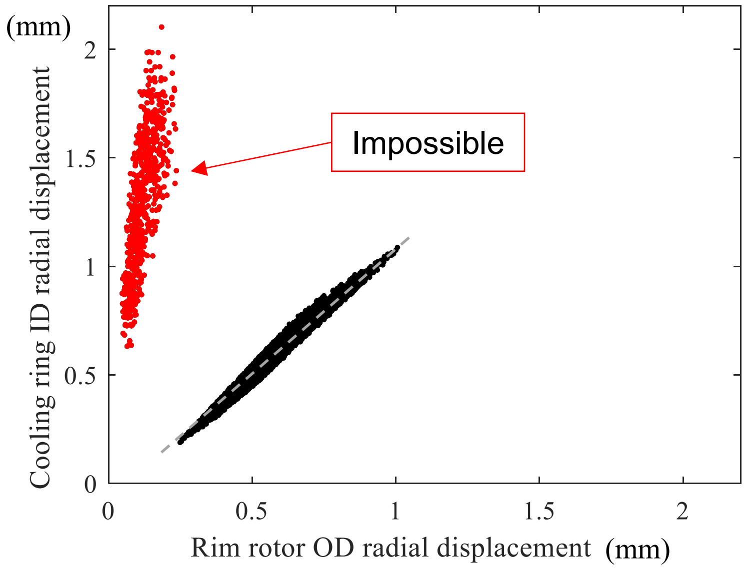

Figure A.13 Identification of erroneous calculation points due to numerical contact failure.

$$p \propto \frac{m\omega^2}{A} \tag{A.3}$$

Where p is proportional to average blade contact pressure, m is blade mass, ω is rotational speed and A is blade contact area. p is compared to FE average contact pressure results in Figure A.14. This excludes a total of 544 points from the 4822 calculated points (11.3 %), leaving a data population of 4278 data points.

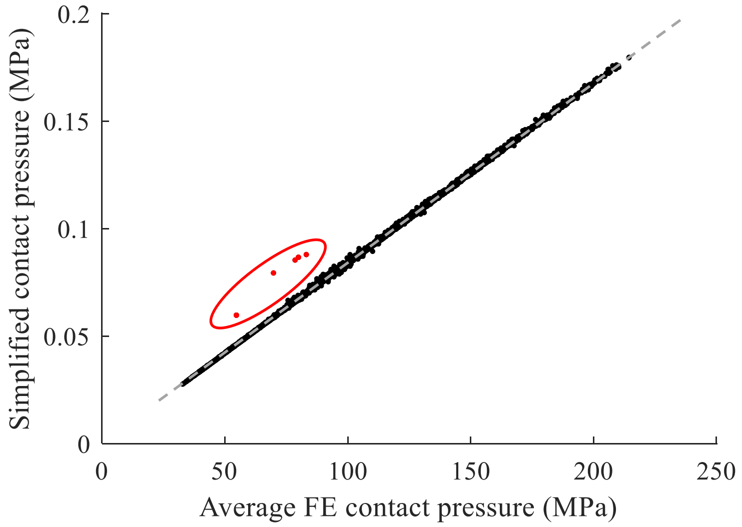

Figure A.14 Outliers (red) selected based on contact pressure correlation

APPENDIX B

DIC POST-TREATMENT

Data was extracted from the .csv files created from the DIC datasets. DIC outputs of interest in this study are *x* and *y* position of points on the specimens, as well as *u* and *v*, i.e. *x*- and *y*-direction displacement of each point. This was done with MATLAB.

Both mechanical and thermal loading steps were assessed similarly. First, displacement and position data are converted to meshgrid format. Second, the displacement (*v* for force loading and *u* for thermal loading) of interest at the corresponding *x* position value are extracted. Finally, displacement is plotted against the loading in question, in mesh form.

B.1 Compressive Preload

Here is an example of Specimen Bloc04, where the vertical displacement *v* is shown in Figure B.1. Note that blank spots in the data maps are due to the presence of NaNs where DIC failed to interpolate a result due to speckle distribution or infrared emission at high temperature.

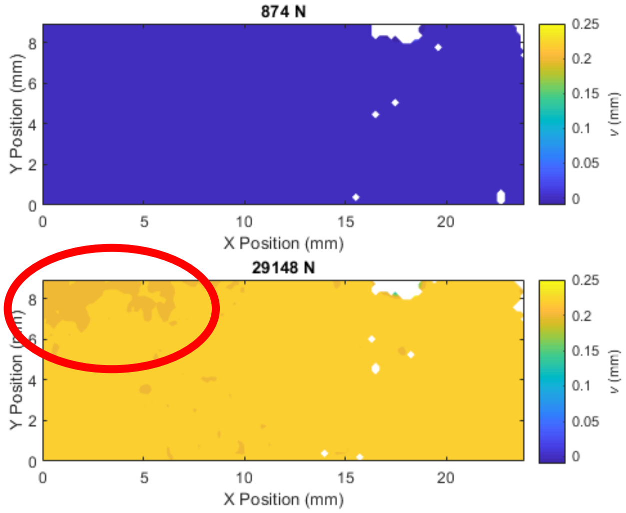

Figure B.1 Vertical displacement of DIC points at compressive loading beginning (top) and near the end (bottom); Bloc04 was loaded at a magnitude of 30 kN

Preload caused significant movement of the entire specimen, shown with an overall shift in *v*-value during compressive loading, from 0 to 0.25 mm. However, a difference in *v*-value in the $x = 0$ to 7 mm range indicates that the sample was possibly squeezed a little more on that side due to press misalignment. By subtracting the specimen tips' displacement from one another, using Δv instead of v, it is possible to track the squeeze according to force magnitude and x position, as illustrated in Figure B.2 for the force magnitudes in Figure B.1.

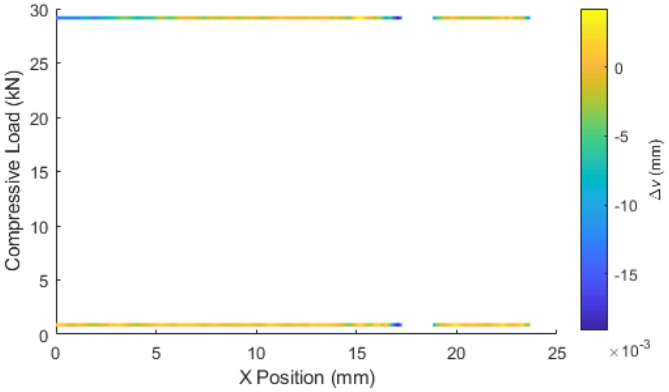

Figure B.2 Difference in specimen tip vertical displacement (Δv) for the force magnitudes in Figure B.1

It should be noted that the *y*-mean of the topmost and bottommost 5 rows was used to reduce data spread caused by local DIC variations. NaN values and large interpolation variations tend to appear along the specimen edges, so Δv must be seen as an approximate value. However, it does faithfully represent load misalignment.

The full evolution of preload "squeeze" is plotted in Figure B.3, according to applied compressive force. A Δv value around 0 means that the block has undergone rigid body movement, i.e. the whole test rig moved, whereas a negative value means that the specimen tips have gotten closer. This can be converted to local normal stress σ_y using Eq. (B.1), and is plotted in Figure B.4.

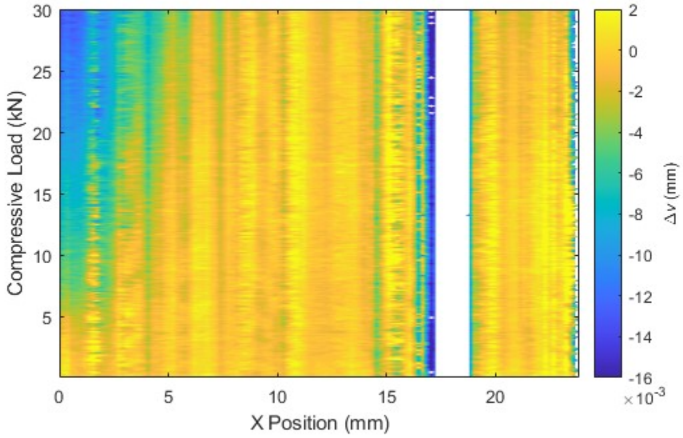

Figure B.3 Evolution of the difference between specimen tip vertical displacement according to compressive preload force magnitude

$$\sigma_y(x) = \frac{\Delta v(x)}{H} E \tag{B.1}$$

Where H is vertical distance between the rows compared in Δv, and E is the ceramic specimen's Young's Modulus (300 Gpa for silicon nitride).

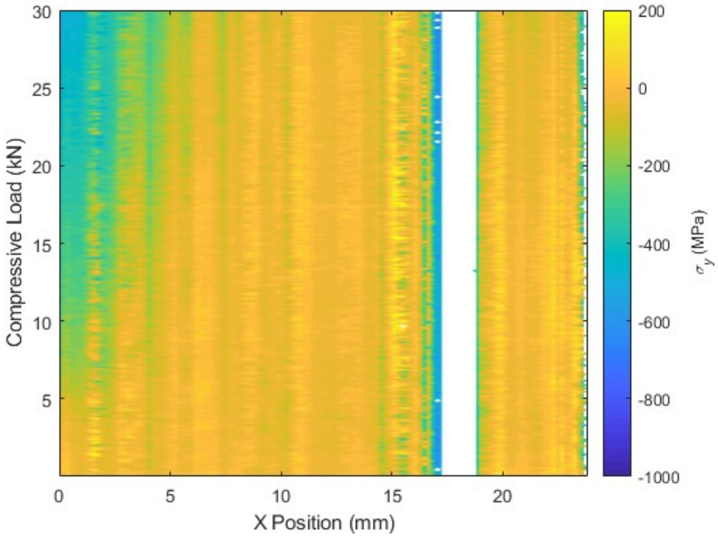

Figure B.4 Local normal stress σ_y along specimen length, according to compressive load

This shows that the normal compressive stress along the *x*-axis is not constant, which will affect the frictional stress at the interface. In this case, only one end of the specimen is clamped with considerable force, whereas the rest is roughly free. The variations near blank NaN areas should be ignored. Practically, only the final loading value is important, plotted in Figure B.5: All preload curves are shown on Figure B.6. A flat curve means the preload is uniform across the specimen, whereas a bell-shaped curve means the specimen is squeezed at one or both ends.

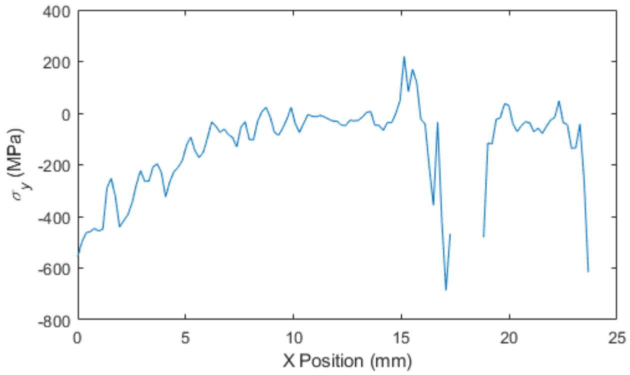

Figure B.5 Final vertical normal stress state along Bloc04 specimen *x*-axis

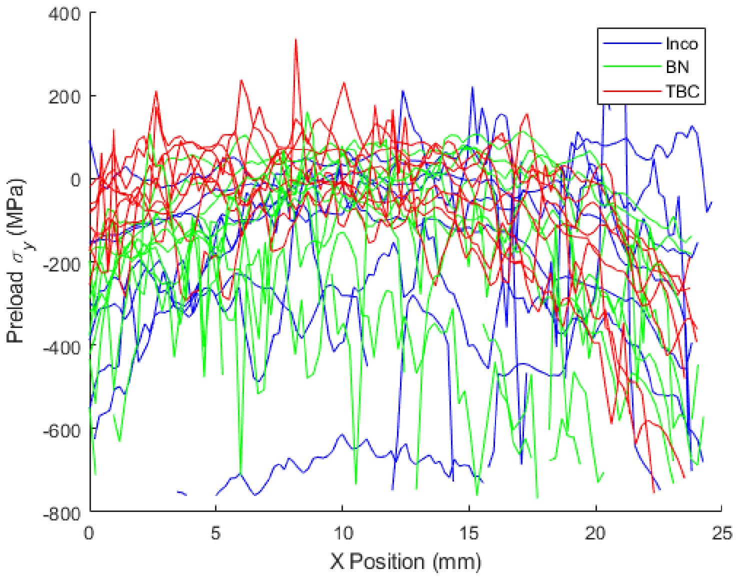

Figure B.6 All preload curves coloured according to interface type

Although a little noisy, Figure B.6 highlights 2 phenomena:

i) Specimens tend to be squeezed at one or both ends. This is due to the 3D deformation of the interface, complying to the relatively stiff ceramic specimen. This is shown in further detail in B.3.

ii) Coated specimens (hBN, TBC) tend to have a more repeatable loading profile, compared to direct Inconel. In the case of hBN, this is estimated to be due to the low friction coefficient, allowing the specimen to align itself more easily. In the case of TBC, the slight compliance of the first microns in the topcoat could assure the required "give" to achieve a more repeatable loading.

These hypotheses rely on high repeatability of the preload method. Given the alignment issues that were experienced in the first tester specimens before adopting the ball-and-socket alignment rig, it is possible that the poor repeatability of the Inconel interface specimens' preload is simply due to human error. As mentioned above, the local pressure along the specimen is quite different from average pressure, which causes significant pinching. As is seen in Figure B.7, the actual contact pressure is not what is measured with DIC. The following subsections group the preload pinching by interface type.

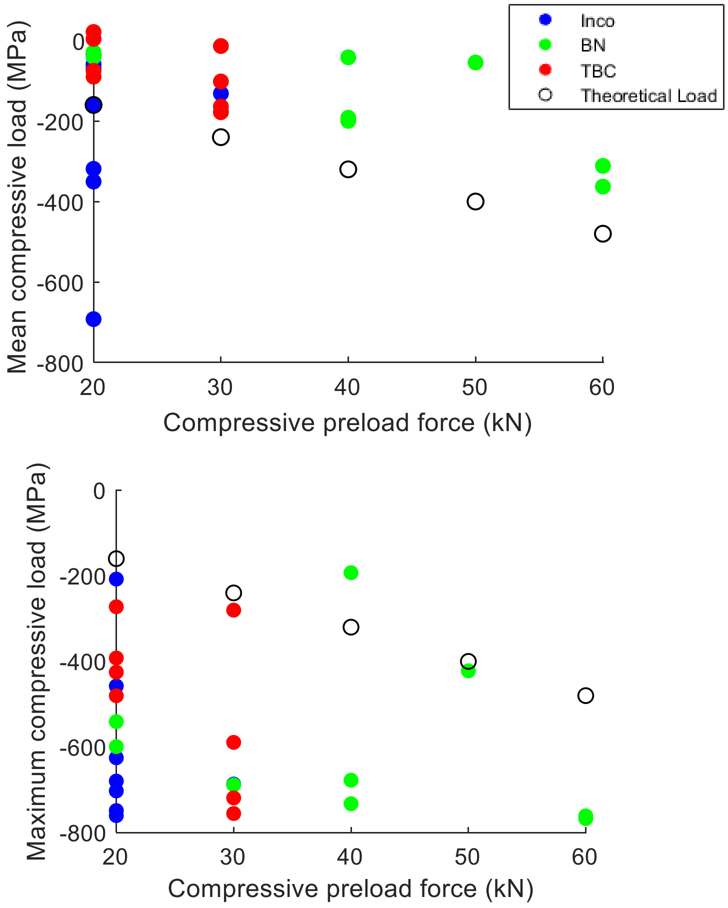

Figure B.7 DIC mean (left) and maximum (right) compressive loads differ from theoretical average load due to 3D effects between the interface plate and the specimen

B.1.1 Inconel interface

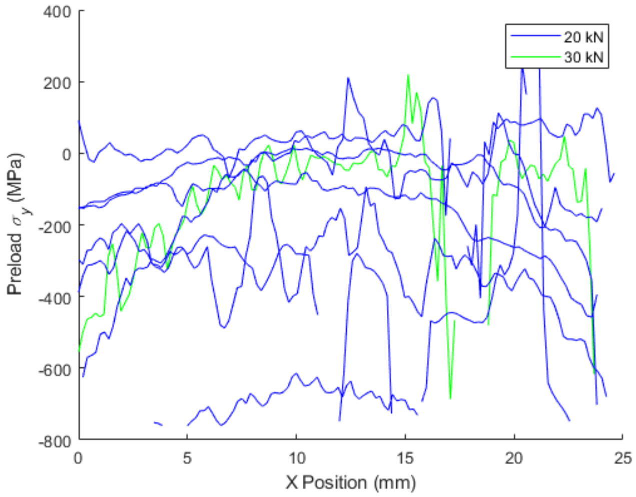

Figure B.8 Inconel interface preload coloured according to force value

There are several outliers in Figure B.8, which are thought to be due to specimen misalignment in the transverse direction, which could increase apparent preload, as illustrated in Figure B.9. The specimens with very high pressure magnitude (< -200 MPa throughout specimen) were taken before the full alignment apparatus was designed, which corroborates to the transverse misalignment hypothesis.

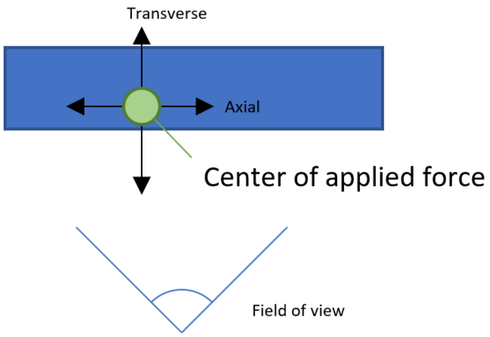

Figure B.9 Force misalignment schematic

B.1.2 Boron nitride interface

The boron nitride interface test runs were done with the full alignment rig, and each run was done on “fresh” hBN, as there was hBN depletion after every run, as shown in Figure B.10.

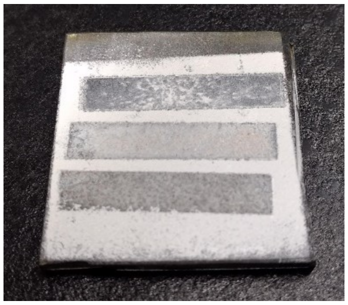

Figure B.10 Boron nitride interface after 3 test runs, showing hBN depletion at the interface with the specimen

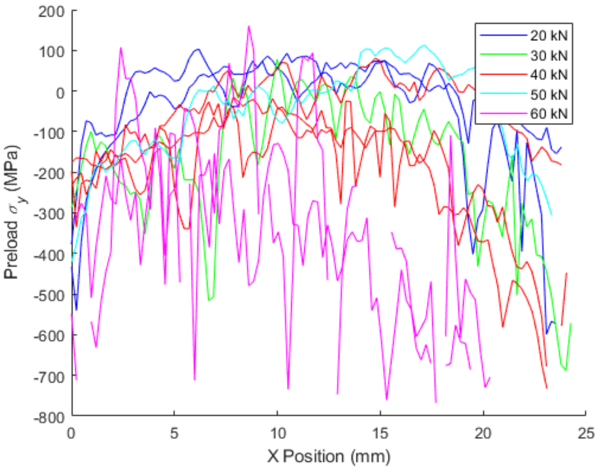

Figure B.11 hBN interface preload coloured according to force value

The hBN interface runs were much more consistent, although squeezing was still dominant as is seen in the bell-shape in all preload curves. The preload value was increased to higher values, as no failure occurred at high temperature in the specimens at the preload values tested with the Inconel interface.

B.1.3 TBC interface

Preload values were returned to Inconel values, as the friction coefficient with TBC is similar and failure occurred in a very similar fashion upon specimen heating. These test runs had the most repeatable data outputs. There is no significant difference between the test runs (see Figure B.12).

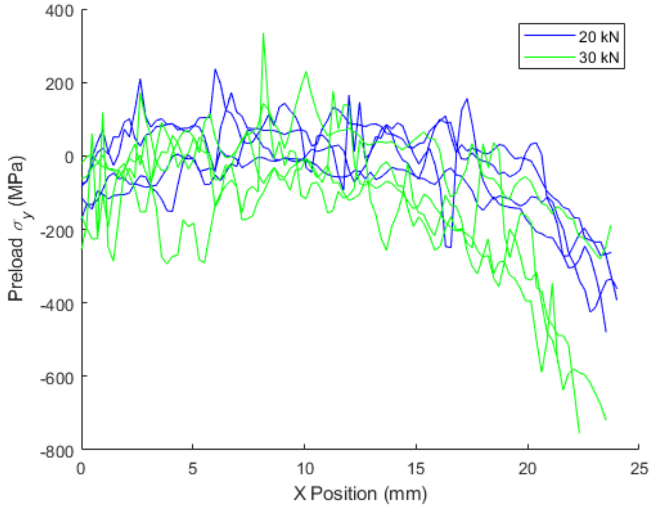

Figure B.12 TBC interface preload coloured according to force value

B.2 Thermal load and segmenting

Thermal load is surmised to cause the axial (*x*-wise) failure in the test specimens, as the metallic components in contact with the specimen expand more than the specimen itself. Thus, horizontal displacement *u* is observed in this portion, as plotted in Figure B.13. DIC was recorded up to 404 °C.

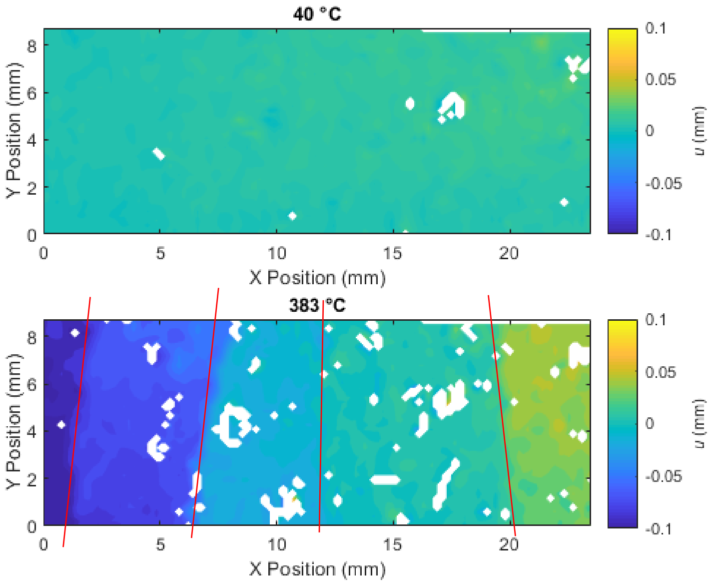

Figure B.13 *x*-displacement *u* of specimen DIC points at low temperature (top) and high temperature (bottom); fracture lines are identified in red

As chunks of the block break away due to friction, the horizontal displacement of these chunks becomes apparent. Thus, smaller blocks are formed as the initial specimen breaks into smaller pieces. Typical failure is illustrated in Figure B.14 (not the same block as in Figure B.13), which resembles the failure shown in post-processing DIC.

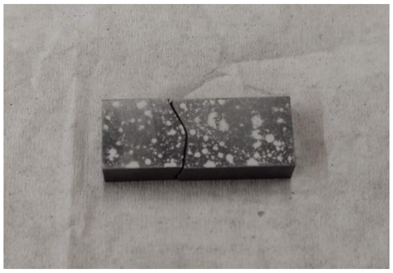

Figure B.14 Typical specimen failure after test run

In a similar fashion to the compressive load, the *u* displacement is plotted in Figure B.15 against temperature. The resulting broken segments are identified, as well as the temperature at which failure occurs.

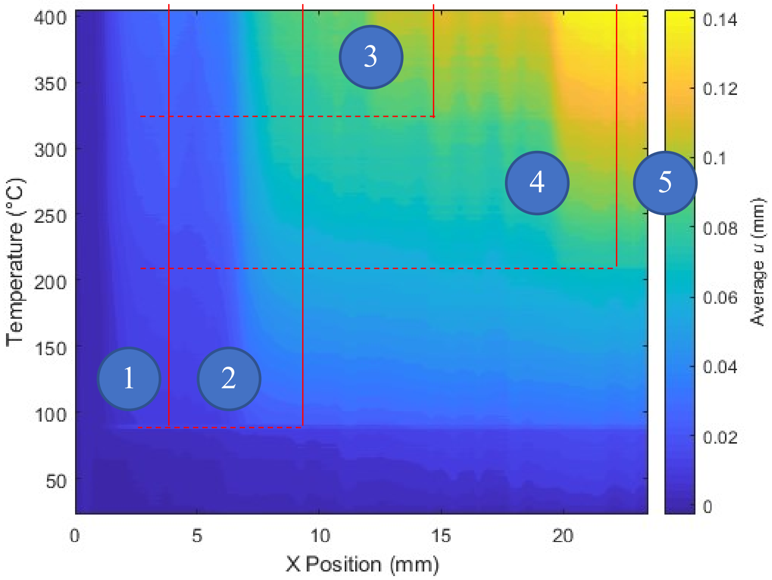

Figure B.15 Progression of y-averaged x-wise displacement u according to temperature for specimen Bloc04, and broken-off segment identification

Sharp changes in color in the x-axis signify a break in the specimen. It is therefore possible to know at which temperature the failures occurred and evaluate the strain in the sample before and after these ruptures.

Data past 400 °C is polluted – many NaNs and extreme interpolated variations – due to increasing infrared emission from the ceramic sample, thus it is discarded. In order to estimate strain state, the *y*-averaged *u* displacement plot at 400 °C is used to pick the analyzed segments. Using the brush tool in MATLAB, as shown in Figure B.16, the broken segments are defined. Their strain, as well as overall strain, are shown in Figure B.17.

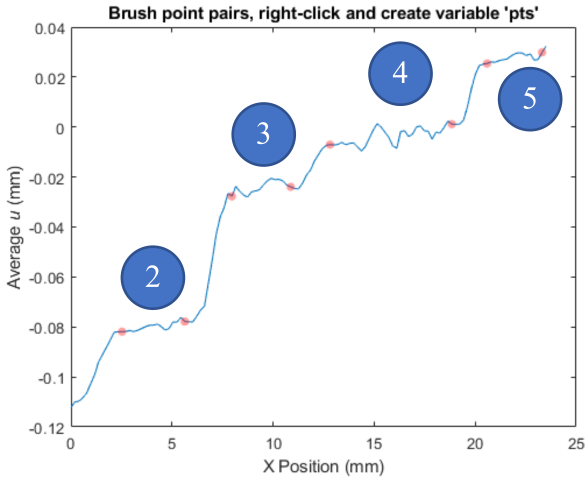

Figure B.16 The brush tool is used to identify the segment extremities at 400 °C; segment 1 is ignored as it is too short to be correctly delimited

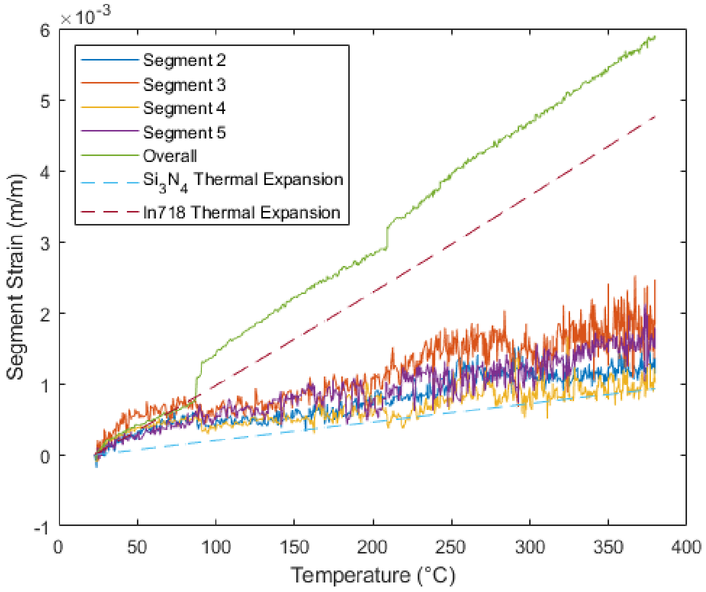

Figure B.17 Total segment and overall specimen strain according to temperature for specimen Bloc04

When failures occur, as identified in Figure B.15, discontinuities can be seen in the various curves. The overall strain curve tends to jump further up as segments snap away from each other, and segment strain remains relatively constant, with a slight drop, or relaxation, after rupture of the stressed segment.

This strain includes thermal expansion, which is identified in Figure B.17, for a CTE of 2.6 µ/m°C for SN235P, according to Kyocera's specifications. This theoretical expansion value becomes a baseline and subtracting it gives a good idea of mechanical strain induced by friction, which can be multiplied by Young's modulus to get the *x*-wise stress state in the specimen segments. The same figure then becomes:

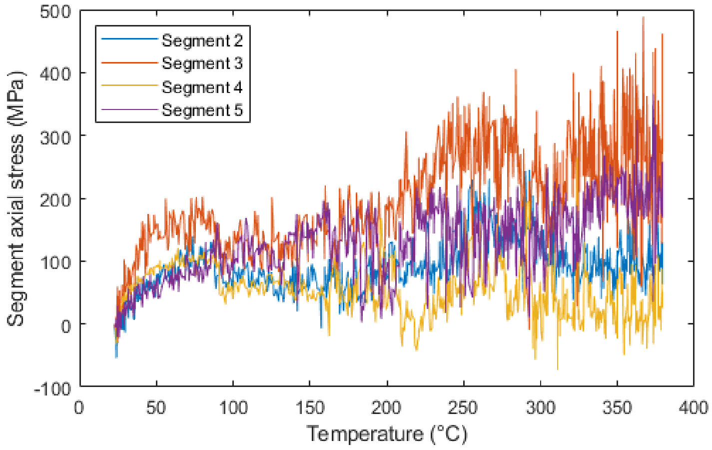

Figure B.18 Axial (*x*-direction) stress for identified segments in specimen Bloc04

B.3 Segment Stress

Figure B.19, a zoom-in on the initial portion of the ΔT ramp shown in Figure 6.20, shows that specimens achieve a given strain before slipping. This strain is proportional to the maximum permissible frictional stress at the interface. Direct contact with Inconel gives the highest strain value before slip. The coated specimens seem to offer lower frictional stress and seem to have similar maximum strain values, although hBN is a bit more consistently lower.

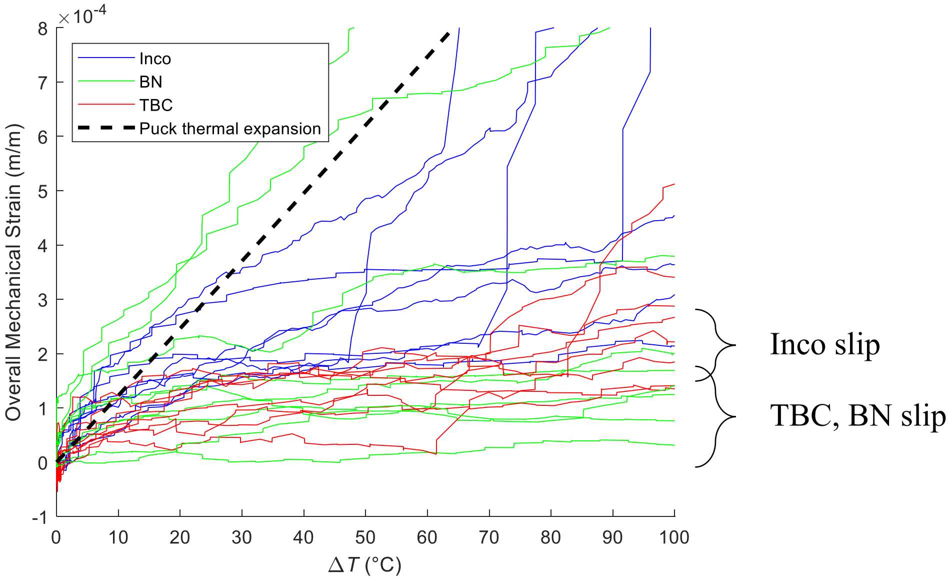

Figure B.19 Zoom in on initial sticking of specimens, at $\Delta T < 100$ °C

As specimens break in smaller segments, the stress state of these segments can be tracked. After removing a few obvious outliers, the stress-temperature charts for all segmented specimens are illustrated in Figure B.20.

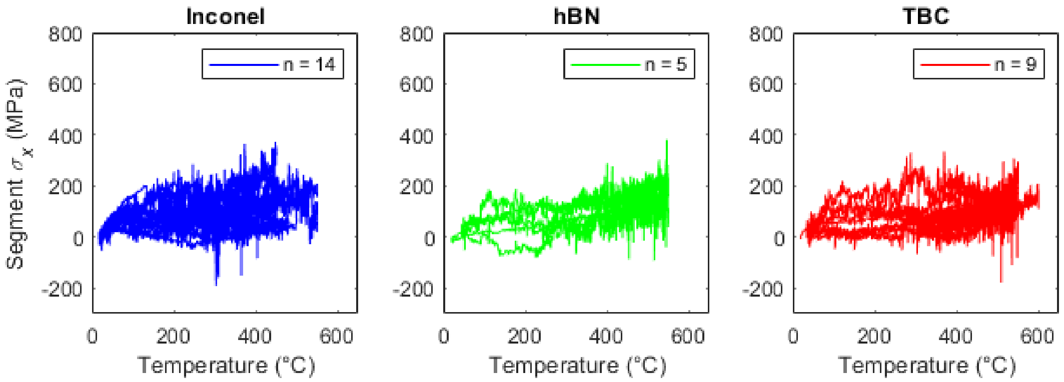

Figure B.20 Specimen segments' axial stress state and total number n of analyzed segments per interface type.

Absolute stress values should be taken with a pinch of salt, as they are quite dependent on manual segment selection in MATLAB, and on actual silicon nitride thermal expansion vs theoretical. For example, negative stress values are highly improbable. However, the general stress state is significantly lower for hBN-coated interface test runs. This hints at a 2 to 3 times lower thermal expansion-induced stresses with hBN over Inconel and TBC. It is worth noting that the hBN "segment" curves are mostly full specimens, as most simply did not break during tests and thus the overall stress state is automatically plotted instead. TBC-coated interface test runs had higher stress levels in 3 segments, which might be due to post-processing errors. After some more pruning of data, it becomes obvious in Figure B.20 that there is little variation of stress levels in the segments.

Figure B.20 indicates that there is a “preferred” state for the ceramic specimen segments where it remains unbroken. It is deemed safe to operate within a 200 MPa tensile stress limit. An hBN coating allows to offset the tolerated thermal strain difference before reaching 200 MPa.

B.4 FE Pinching Analysis

There is significant deformation of the interface sheet metal during preload, which causes local “pinching” or “squeezing” of the test specimen. The simplified test rig CAD is shown in Figure B.21.

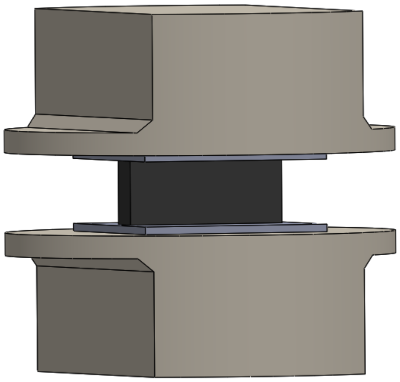

Figure B.21 Simplified test rig with interface sheet metal in contact with specimen and heater pucks

The deformation FE results for a typical test run are shown in Figure B.22.

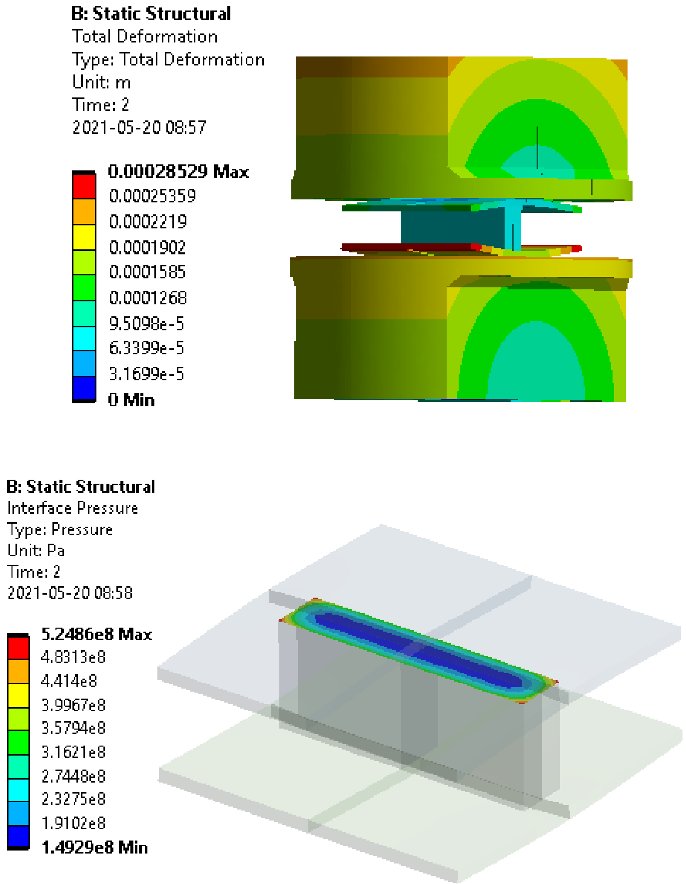

Figure B.22 Deformed test rig at high temperature (left) and contact pressure distribution (right)

The 3D deformation of the metal sheet unloads the center of the specimen and pinches the specimen extremities. Along with press misalignment, this explains the bell-shaped preload curves observed in Section B.1. FE stress results are strongly sensitive to mesh sizing and should be the object of an independent analysis report, to model the data shown in this report.

Further proof is provided by the no-oxidation patch of the Inconel sheet after a high-temperature test, shown in Figure B.23. This also indicates a very low thermal resistance between heating puck and Inconel sheet.

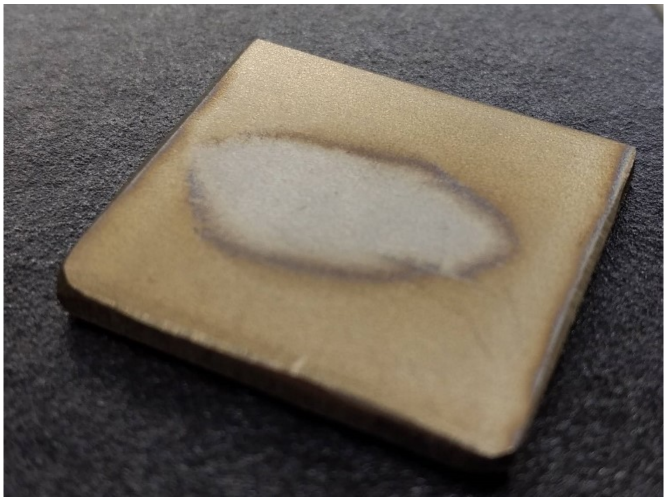

Figure B.23 Contact between Inconel interface sheet and puck is shown where oxidation is absent, in alignment with ceramic specimen pressure patch

REFERENCES

[1] Gohardani, A. S., Doulgeris, G., and Singh, R. (2011). “Challenges of future aircraft propulsion: A review of distributed propulsion technology and its potential application for the all electric commercial aircraft.” *Progress in Aerospace Sciences*, volume 47, number 5, p. 369–391. DOI : 10.1016/j.paerosci.2010.09.001.

[2] Pornet, C. and Isikveren, A. T. (2015). “Conceptual design of hybrid-electric transport aircraft.” *Progress in Aerospace Sciences*, volume 79, p. 114–135. DOI : 10.1016/j.paerosci.2015.09.002.

[3] Bowman, C. L., Felder, J. L., and Marien, T. V. (2018). “Turbo- and Hybrid-Electrified Aircraft Propulsion Concepts for Commercial Transport.” In *2018 AIAA/IEEE Electric Aircraft Technologies Symposium (EATS)*. p. 1–8.

[4] Chiesa, P., Lozza, G., and Mazzocchi, L. (2005). “Using Hydrogen as Gas Turbine Fuel.” *Journal of Engineering for Gas Turbines and Power*, volume 127, number 1, p. 73–80. DOI : 10.1115/1.1787513.

[5] Gupta, K. K., Rehman, A., and Sarviya, R. M. (2010). “Bio-fuels for the gas turbine: A review.” *Renewable and Sustainable Energy Reviews*, volume 14, number 9, p. 2946–2955. DOI : 10.1016/j.rser.2010.07.025.

[6] Habib, Z., Parthasarathy, R., and Gollahalli, S. (2010). “Performance and emission characteristics of biofuel in a small-scale gas turbine engine.” *Applied Energy*, volume 87, number 5, p. 1701–1709. DOI : 10.1016/j.apenergy.2009.10.024.

[7] Ng, K. S., Farooq, D., and Yang, A. (2021). “Global biorenewable development strategies for sustainable aviation fuel production.” *Renewable and Sustainable Energy Reviews*, volume 150, p. 111502. DOI : 10.1016/j.rser.2021.111502.

[8] Eser, P., Singh, A., Chokani, N., and Abhari, R. S. (2016). “Effect of increased renewables generation on operation of thermal power plants.” *Applied Energy*, volume 164, p. 723–732. DOI : 10.1016/j.apenergy.2015.12.017.

[9] Fortier-Topping, H., Vézina, G., Plante, J.-S., and Brouillette, M. (2013). “Design and Sensitivity Study of a Combustion Chamber of a Supersonic Rim-Rotor Gas Turbine (SRGT) Engine.” presented at the 21st Annual Conference of the CFD Society of Canada, Sherbooke, Canada.

[10] Landry, C., Dubois, P. K., Courtois, N., Charron, F., Picard, M., and Plante, J.-S. (2016). “Development of an Inside-Out Ceramic Turbine.” In *Proc. of ASME Turbo Expo 2016*, Seoul, South Korea. ASME. DOI : 10.1115/GT2016-57041.

[11] Picard, M., Rancourt, D., Plante, J.-S., and Brouillette, M. (2012). “Rim-Rotor Rotary Ramjet Engine, Part 2: Quasi-One-Dimensional Aerothermodynamic Design.” *Journal of Propulsion and Power*, volume 28, number 6, p. 1304–1314. DOI : 10.2514/1.B34226.

[12] Plante, J.-S. (2001). “Conception préliminaire d’un moteur rotatif continu à combustion induite par onde de choc.” Mémoire de maîtrise. Université de Sherbrooke, Sherbrooke, QC, Canada.

[13] Rancourt, D., Picard, M., Denninger, M., Plante, J.-S., Chen, J., and Yousefpour, A. (2012). “Rim-Rotor Rotary Ramjet Engine, Part 1: Structural Design and Experimental Validation.” *Journal of Propulsion and Power*, volume 28, number 6, p. 1293–1303. DOI : 10.2514/1.B34227.

[14] Vézina, G., Fortier-Topping, H., Bolduc-Teasdale, F., Rancourt, D., Picard, M., Plante, J.-S., Brouillette, M., and Fréchette, L. (2015). “Design and Experimental Validation of a Supersonic Concentric Micro Gas Turbine.” *Journal of Turbomachinery*, volume 138, number 2, p. 021007–021007. DOI : 10.1115/1.4031863.

[15] ACE-100. (2011). “23.1309-1E - System Safety Analysis and Assessment for Part 23 Airplanes” (Advisory Circular AC 23.1309-1E). Federal Aviation Administration.

[16] van Roode, M., Price, J. R., Parthasarathy, V., Richerson, D. W., and Graves, G. A. (2001). “Ceramic Stationary Gas Turbine Program: Monolithic Ceramic Component Development Summary.” presented at the ASME Turbo Expo 2001: Power for Land, Sea, and Air, New Orleans, LA, USA. ASME. p. 14. DOI : 10.1115/2001-GT-0457.

[17] Richerson, D. W. (2006). “Historical Review of Addressing the Challenges of Use of Ceramic Components in Gas Turbine Engines.” presented at the ASME Turbo Expo 2006: Power for Land, Sea, and Air, Barcelona, Spain. ASME. p. 241–254. DOI : 10.1115/GT2006-90330.

[18] Nemeth, N. N., Powers, L. M., Janosik, L. A., and Gyekenyesi, J. P. (2003). “CARES/LIFE Ceramics Analysis and Reliability Evaluation of Structures Life Prediction Program” (Technical Report NASA TM-2003-106316). NASA, Cleveland, OH, USA.

[19] Richerson, D. W. and Anson, D. (2002). “Evolution of Ceramic Gas Turbine Development Programs at Engine Manufacturers in the United States,” In *Ceramic Gas Turbine Design and Test Experience*. M. van Roode, M. K. Ferber, and D. W. Richerson, Eds. ASME Press, New York, NY, USA, p. 11–16.

[20] van Roode, M. (2002). “Evolution of Ceramic Gas Turbine Development Programs at Engine Manufacturers in Western Europe,” In *Ceramic Gas Turbine Design and Test Experience*. M. van Roode, M. K. Ferber, and D. W. Richerson, Eds. ASME Press, New York, NY, USA, p. 445–452.

[21] GE Aviation. (February 2015). “GE Successfully Tests World’s First Rotating Ceramic Matrix Composite Material for Next-Gen Combat Engine.”

https://www.geaviation.com/press-release/military-engines/ge-successfully-tests-worlds-first-rotating-ceramic-matrix-composite (Accessed November 3 2021).

[22] Zok, F. W. (June 2016). "Ceramic-matrix composites enable revolutionary gains in turbine engine efficiency," *American Ceramic Society Bulletin*, volume 95, number 5, p. 22–28, (June 2016).

[23] Steibel, J. (April 2019). "Ceramic matrix composites taking flight at GE Aviation," *American Ceramic Society Bulletin*, volume 98, number 3, p. 30–33, (April 2019).

[24] Kannmacher, K. D. and Groseclose, L. E. (1991). "Design and Analysis of Ceramic and CMC Components for Advanced Gas Turbines." In *Proc of the ASME 1991 International Gas Turbine and Aeroengine Congress & Exposition*, Orlando, FL, USA. ASME. DOI : 10.1115/91-GT-156.

[25] Goldberg, R. K. B. (2012). "Investigation of Effects of Material Architecture on the Elastic Response of a Woven Ceramic Matrix Composite" (Technical Report TN-2012-217269). NASA, Cleveland, OH, USA.

[26] Boyle, R. J., Parikh, A. H., Halbig, M. C., and Nagpal, V. K. (2013). "Design Considerations for Ceramic Matrix Composite Vanes for High Pressure Turbine Applications." In *Proc. of the ASME Turbo Expo 2013: Turbine Technical Conference and Exposition*, San Antonio, TX, USA. ASME. DOI : 10.1115/GT2013-95104.

[27] van Roode, M. (2009). "Ceramic Gas Turbine Development: Need for a 10 Year Plan." *Journal of Engineering for Gas Turbines and Power*, volume 132, number 1, p. 011301. DOI : 10.1115/1.3124669.

[28] Takehara, I., Tatsumi, T., and Ichikawa, Y. (2002). "Summary of CGT302 Ceramic Gas Turbine Research and Development Program." *Journal of Engineering for Gas Turbines and Power*, volume 124, number 3, p. 627–635. DOI : 10.1115/1.1451704.

[29] Lin, H. T. and Ferber, M. K. (2002). "Mechanical reliability evaluation of silicon nitride ceramic components after exposure in industrial gas turbines." *Journal of the European Ceramic Society*, volume 22, number 14, p. 2789–2797.

[30] Opila, E. J., Robinson, R. C., Fox, D. S., Wenglarz, R. A., and Ferber, M. K. (2003). "Additive Effects on Si3N4 Oxidation/Volatilization in Water Vapor." *Journal of the American Ceramic Society*, volume 86, number 8, p. 1262–1271. DOI : 10.1111/j.1151-2916.2003.tb03462.x.

[31] Eaton, H. E. and Linsey, G. D. (2002). "Accelerated oxidation of SiC CMC's by water vapor and protection via environmental barrier coating approach." *Journal of the European Ceramic Society*, volume 22, number 14, p. 2741–2747. DOI : 10.1016/S0955-2219(02)00141-3.

[32] Pint, B. A., Stack, P., and Kane, K. A. (2021). "Predicting EBC Temperature Limits for Industrial Gas Turbines." In *Proc. of the ASME Turbo Expo 2021: Turbomachinery*

Technical Conference and Exposition, Virtual, Online. ASME. DOI : 10.1115/GT2021-59408.

[33] Landry, C., Dubois, P. K., Courtois, N., Charron, F., Picard, M., and Plante, J.-S. (2016). "Development of an Inside-Out Ceramic Turbine." In *Proc. of the ASME Turbo Expo 2016: Turbomachinery Technical Conference and Exposition*, Seoul, South Korea. ASME. DOI : 10.1115/GT2016-57041.

[34] Brouillette, M. and Plante, J.-S. (2008). "Rotary Ramjet Engine." Brevet US 7337606 B2.

[35] Picard, M., Rancourt, D., and Plante, J. S. (2011). "Rim-rotor rotary ramjet engine (R4E): Design and experimental validation of a proof-of-concept prototype." In *ISABE Conference, Gothenburg, Sweden, Sept*, Gothenburg, Sweden. p. 12–16.

[36] Plante, J.-S., Rancourt, D., and Picard, M. (2011). "Supersonic rim-rotor gas turbine." Brevet US 61/538201.

[37] Vézina, G., Fortier-Topping, H., Bolduc-Teasdale, F., Rancourt, D., Picard, M., Plante, J.-S., Brouillette, M., and Fréchette, L. (2016). "Design and Experimental Validation of a Supersonic Concentric Micro Gas Turbine." *Journal of Turbomachinery*, volume 138, number 2. DOI : 10.1115/1.4031863.

[38] Plante, J.-S., Picard, M., Landry-Blais, A., Fortier-Topping, H., Gurin, M., Landry, C., Dubois, P., Frechette, L. G., and Picard, B. (2017). "High Temperature Ceramic Rotary Turbomachinery." Brevet US20170074102A1.

[39] Jimenez, O., McClain, J., Edwards, B., Parthasarathy, V., Bagheri, H., and Bolander, G. (1998). "Ceramic Stationary Gas Turbine Development Program — Design and Test of a Ceramic Turbine Blade." presented at the ASME 1998 International Gas Turbine and Aeroengine Congress and Exhibition, Stockholm, Sweden. ASME. p. V005T13A015. DOI : 10.1115/98-GT-529.

[40] Yoon, K. J., Wiederhorn, S. M., and Luecke, W. E. (2000). "Comparison of Tensile and Compressive Creep Behavior in Silicon Nitride." *Journal of the American Ceramic Society*, volume 83, number 8, p. 2017–2022. DOI : 10.1111/j.1151-2916.2000.tb01505.x.

[41] Dubois, P. K., Landry, C., Thibault, D., Plante, J.-S., Picard, M., and Picard, B. (2022). "Benefits and Challenges of the Inside-Out Ceramic Turbine: An Experimental Assessment." *Journal of Propulsion and Power*, volume 38, number 2, p. 221–228. DOI : 10.2514/1.B38004.

[42] Sarlioglu, B. and Morris, C. T. (2015). "More Electric Aircraft: Review, Challenges, and Opportunities for Commercial Transport Aircraft." *IEEE Transactions on Transportation Electrification*, volume 1, number 1, p. 54–64. DOI : 10.1109/TTE.2015.2426499.

[43] Gohardani, A. S., Doulgeris, G., and Singh, R. (2011). "Challenges of future aircraft propulsion: A review of distributed propulsion technology and its potential application for

the all electric commercial aircraft." *Progress in Aerospace Sciences*, volume 47, number 5, p. 369–391. DOI : 10.1016/j.paerosci.2010.09.001.

[44] Voskuijl, M., van Bogaert, J., and Rao, A. G. (2018). "Analysis and design of hybrid electric regional turboprop aircraft." *CEAS Aeronautical Journal*, volume 9, number 1, p. 15–25. DOI : 10.1007/s13272-017-0272-1.

[45] McDonald, C. F. and Rodgers, C. (2008). "Small Recuperated Ceramic Microturbine Demonstrator Concept." *Applied Thermal Engineering*, volume 28, number 1, p. 60–74. DOI : 10.1016/j.applthermaleng.2007.01.020.

[46] Kochrad, N., Courtois, N., Charette, M., Picard, B., Landry-Blais, A., Rancourt, D., Plante, J.-S., and Picard, M. (2017). "System-Level Performance of Microturbines With an Inside-Out Ceramic Turbine." *Journal of Engineering for Gas Turbines and Power*, volume 139, number 6. DOI : 10.1115/1.4035648.

[47] Picard, B., Picard, M., Plante, J.-S., and Rancourt, D. (2020). "Optimum Sub-Megawatt Electric-Hybrid Power Source Selection." *Aircraft Engineering and Aerospace Technology*, volume 92, number 5, p. 717–726. DOI : 10.1108/AEAT-06-2019-0119.

[48] Picard, B., L. -Blais, A., Picard, M., and Rancourt, D. (2019). "Power-Density vs Efficiency Trade-Off for a Recuperated Inside-Out Ceramic Turbine (ICT)." In *Proc. ASME Turbo Expo 2019*, Phoenix, AZ, USA. ASME. DOI : 10.1115/GT2019-91017.

[49] McLean, A. F. and Fisher, E. A. (1981). "Brittle Materials Design, High Temperature Gas Turbine" (Technical Report AMMRC TR81-14). Ford Motor Company, Dearborn, MI, USA.

[50] Hempel, H. and Wiest, H. (1986). "Structural Analysis and Life Prediction for Ceramic Gas Turbine Components for the Mercedes-Benz Research Car 2000." In *Proc. of the ASME 1986 International Gas Turbine Conference and Exhibit*, Düsseldorf, West Germany. ASME. DOI : 10.1115/86-GT-199.

[51] McEntire, B. J., Hengst, R. R., Collins, W. T., Taglialavore, A. P., and Yeckley, R. L. (1993). "Ceramic Component Processing Development for Advanced Gas Turbine Engines." *Journal of Engineering for Gas Turbines and Power*, volume 115, number 1, p. 1–8. DOI : 10.1115/1.2906678.

[52] Huang, M., He, P., Yang, J., Duan, F., Lim, S. C., and Yip, M. S. (2014). "Fabrication and Characterization of Mini Alumina Ceramic Turbine Rotor Using a Tailored Gelcasting Process." *Ceramics International*, volume 40, number 6, p. 7711–7722. DOI : 10.1016/j.ceramint.2013.12.112.

[53] Lin, H.-T., Ferber, M. K., Becher, P. F., Price, J. R., Roode, M. V., Kimmel, J. B., and Jimenez, O. D. (2006). "Characterization of First-Stage Silicon Nitride Components After Exposure to an Industrial Gas Turbine." *Journal of the American Ceramic Society*, volume 89, number 1, p. 258–265. DOI : 10.1111/j.1551-2916.2005.00678.x.

[54] Yoshida, H. and Li, Y. (2006). “FOD Simulation for Ceramic Turbine Blades.” *Transactions of the Japan Society for Aeronautical and Space Sciences*, volume 49, number 164, p. 81–86. DOI : 10.2322/tjsass.49.81.

[55] Coty, P. J., Lane, A. D., Lee, J. B., and Meyer, L. J. (1980). “A Design Review of Ceramic Components for Turbine Engines.” *Journal of Engineering for Gas Turbines and Power*, volume 102, number 2, p. 437–447. DOI : 10.1115/1.3230276.

[56] Schenk, B. (2002). “Ceramic Turbine Engine Demonstration Project: A Summary Report.” *Journal of Engineering for Gas Turbines and Power*, volume 124, number 3, p. 617–626. DOI : 10.1115/1.1417983.

[57] Baker, R. R. and Swank, L. R. (1983). “Duo-Density Ceramic Turbine Rotor Development,” In *Ceramics for High-Performance Applications III*, volume 1. E. M. Lenoe, R. N. Katz, and J. J. Burke, Eds. Springer US, p. 597–622. DOI : 10.1007/978-1-4684-3965-6_31.

[58] Xu, Y., Cheng, L., Zhang, L., Yin, H., and Yin, X. (2001). “Mechanical properties of 3D fiber reinforced C/SiC composites.” *Materials Science and Engineering: A*, volume 300, number 1, p. 196–202. DOI : 10.1016/S0921-5093(00)01533-1.

[59] Shao, J., Li, W., Deng, Y., Ma, J., Zhang, X., Geng, P., Kou, H., Chen, L., and Wu, X. (2017). “Theoretical models and influencing factor analysis for the temperature-dependent tensile strength of ceramic fibers and their unidirectional composites.” *Composite Structures*, volume 164, p. 23–31. DOI : 10.1016/j.compstruct.2016.12.054.

[60] Goldsmith, M. B., Sankar, B. V., Haftka, R. T., and Goldberg, R. K. (2015). “Effects of microstructural variability on thermo-mechanical properties of a woven ceramic matrix composite.” *Journal of Composite Materials*, volume 49, number 3, p. 335–350. DOI : 10.1177/0021998313519151.

[61] Stoffer, L. J. (1979). “Novel Ceramic Turbine Rotor Concept” (Technical Report AFAPL-TR-79-2074). General Electric Company, Cincinnati, Ohio, USA.

[62] Kochendörfer, R. (1979). “Compression Loaded Ceramic Turbine Rotor.” In *AGARD Conference Proceedings*, Porz-Wahn, Köln, Germany, volume 4. Advisory Group for Aerospace Research & Development. p. 22/1-22/19.

[63] Danfelt, E. L., Hewes, S. A., and Chou, T.-W. (1977). “Optimization of composite flywheel design.” *International Journal of Mechanical Sciences*, volume 19, number 2, p. 69–78. DOI : 10.1016/0020-7403(77)90001-7.

[64] Courtois, N., Ebacher, F., Dubois, P. K., Kochrad, N., Landry, C., Charette, M., Landry-Blais, A., Fréchette, L., Plante, J.-S., and Picard, M. (2017). “Superalloy Cooling System for the Composite Rim of an Inside-Out Ceramic Turbine.” In *Proc. of ASME Turbo Expo 2017*, Charlotte, NC, USA. ASME. DOI : 10.1115/GT2017-64007.

[65] Takahashi, M., Okabe, N., Zhu, X., and Kagawa, K. (2002). "Probabilistic Strength Estimation for Ceramic-Metal Joints with Various Interlayer Thicknesses." *Materials Science Research International*, volume 8, number 3, p. 109–115. DOI : 10.2472/jsms.51.9Appendix_109.

[66] Choi, S. R., Salem, J. A., Nemeth, N., and Gyekenyesi, J. P. (1994). "Elevated Temperature Slow Crack Growth of Silicon Nitride Under Dynamic, Static and Cyclic Flexural Loading," In *Proceedings of the 18th Annual Conference on Composites and Advanced Ceramic Materials—B*, volume 15. J. B. Wachtman, Ed. John Wiley & Sons, Ltd, p. 597–604. DOI : 10.1002/9780470314555.ch2.

[67] Rice, R. C., Jackson, J. l., Bakuckas, J., and Thompson, S. (2003). "MMPDS-01 Metallic Materials Properties Development and Standardization" (Scientific Report DOT/FAA/AR-MMPDS-01). Federal Aviation Administration, Washington, D.C., USA.

[68] Han, J.-C., Dutta, S., and Ekkad, S. (2012). *Gas Turbine Heat Transfer and Cooling Technology*, Second Edition. CRC Press, Boca Raton, FL, 892 p.

[69] Gates, Jr., S., Price, J., Parthasarathy, V., Miriyala, N., and Jimenez, O. (2000). "Recommended Direction of the Solar/DOE Ceramic Stationary Gas Turbine Program." In *Proc. ASME Turbo Expo 2000*, Munich, Germany. ASME. DOI : 10.1115/2000-GT-0076.

[70] Brentnall, W. D., Roode, M. van, Norton, P. F., Gates, S., Price, J. R., Jimenez, O., and Miriyala, N. (2002). "Ceramic Gas Turbine Development at Solar Turbines Incorporated," In *Ceramic Gas Turbine Design and Test Experience*. M. van Roode, M. K. Ferber, and D. W. Richerson, Eds. ASME Press, New York, NY, USA, p. 155–192.

[71] Bazergui, A., Bui-Quoc, T., Biron, A., McIntyre, G., and Laberge, C. (1993). "Les corps axisymétriques," In *Résistance des matériaux*, 2nd ed. Éditions de l'École Polytechnique de Montréal, Montreal, QC, Canada, p. 291.

[72] U.S. Department of Defense, Ed. (1998). *Military Handbook - Metallic Materials and Elements for Aerospace Vehicle Structures*, 5H ed. U.S. Department of Defense, book p.

[73] Kyocera Fine Ceramics Group. (2020). "Characteristics of Kyocera fine ceramics." Kyocera Corporation, (2020).

[74] Choi, S. R., Zhu, D., and Miller, R. A. (2004). "Mechanical Properties/Database of Plasma-Sprayed ZrO2-8wt% Y2O3 Thermal Barrier Coatings." *International Journal of Applied Ceramic Technology*, volume 1, number 4, p. 330–342. DOI : 10.1111/j.1744-7402.2004.tb00184.x.

[75] Thibault, D., Dubois, P. K., Picard, B., Landry-Blais, A., Plante, J.-S., and Picard, M. (2020). "Experimental Assessment of a Sliding-Blade Inside-Out Ceramic Turbine." presented at the ASME Turbo Expo 2020: Turbomachinery Technical Conference and Exposition, Virtual, Online. American Society of Mechanical Engineers Digital Collection. DOI : 10.1115/GT2020-15137.

[76] Richerson, D. W. (2004). “Ceramic Components in Gas Turbine Engines: Why Has It Taken So Long?,” In *28th International Conference on Advanced Ceramics and Composites A: Ceramic Engineering and Science Proceedings*. John Wiley & Sons, Ltd, p. 3–32. DOI : 10.1002/9780470291184.ch1.

[77] Courtois, N., Ebacher, F., Dubois, P. K., Kochrad, N., Landry, C., Charette, M., Landry-Blais, A., Fréchette, L., Plante, J.-S., and Picard, M. (2017). “Superalloy Cooling System for the Composite Rim of an Inside-Out Ceramic Turbine.” In *Proc. of the ASME Turbo Expo 2017: Turbomachinery Technical Conference and Exposition*, Charlotte, NC, USA, volume 8. ASME. p. 10. DOI : 10.1115/GT2017-64007.

[78] Padture, N. P., Gell, M., and Jordan, E. H. (2002). “Thermal Barrier Coatings for Gas-Turbine Engine Applications.” *Science*, volume 296, number 5566, p. 280–284. DOI : 10.1126/science.1068609.

[79] Zhu, D. and Miller, R. A. (2000). “Thermal conductivity and elastic modulus evolution of thermal barrier coatings under high heat flux conditions.” *Journal of Thermal Spray Technology*, volume 9, number 2, p. 175–180. DOI : 10.1361/105996300770349890.

[80] Martena, M., Botto, D., Fino, P., Sabbadini, S., Gola, M. M., and Badini, C. (2006). “Modelling of TBC system failure: Stress distribution as a function of TGO thickness and thermal expansion mismatch.” *Engineering Failure Analysis*, volume 13, number 3, p. 409–426. DOI : 10.1016/j.engfailanal.2004.12.027.

[81] Ang, A. S. M. and Berndt, C. C. (2014). “A Review of Testing Methods for Thermal Spray Coatings.” *International Materials Reviews*, volume 59, number 4, p. 179–223. DOI : 10.1179/1743280414Y.0000000029.

[82] Wu, D. J., Mao, W. G., Zhou, Y. C., and Lu, C. (2011). “Digital image correlation approach to cracking and decohesion in a brittle coating/ductile substrate system.” *Applied Surface Science*, volume 257, number 14, p. 6040–6043. DOI : 10.1016/j.apsusc.2011.01.119.

[83] Tan, Y., Longtin, J. P., Sampath, S., and Wang, H. (2009). “Effect of the Starting Microstructure on the Thermal Properties of As-Sprayed and Thermally Exposed Plasma-Sprayed YSZ Coatings.” *Journal of the American Ceramic Society*, volume 92, number 3, p. 710–716. DOI : 10.1111/j.1551-2916.2009.02953.x.

[84] Choi, S. R., Zhu, D., and Miller, R. A. (2005). “Effect of Sintering on Mechanical Properties of Plasma-Sprayed Zirconia-Based Thermal Barrier Coatings.” *Journal of the American Ceramic Society*, volume 88, number 10, p. 2859–2867. DOI : 10.1111/j.1551-2916.2005.00504.x.

[85] Lipp, A., Schwetz, K. A., and Hunold, K. (1989). “Hexagonal Boron Nitride: Fabrication, Properties and Applications.” *Journal of the European Ceramic Society*, volume 5, number 1, p. 3–9.

[86] Liu, Z., Gong, Y., Zhou, W., Ma, L., Yu, J., Idrobo, J. C., Jung, J., MacDonald, A. H., Vajtai, R., Lou, J., and Ajayan, P. M. (2013). “Ultrathin high-temperature oxidation-

resistant coatings of hexagonal boron nitride." *Nature Communications*, volume 4, number 1, p. 2541. DOI : 10.1038/ncomms3541.

[87] Subcommittee D20.19. (2014). "ASTM D1894-14 Standard Test Method for Static and Kinetic Coefficients of Friction of Plastic Film and Sheeting" (Standard ASTM D1894-14). ASTM International, West Conshohocken, PA, USA. DOI : 10.1520/D1894-14.